UNIVERSITÀ DEGLI STUDI DI MILANO &
UNIVERSITÀ CATTOLICA DEL SACRO CUORE

SCUOLA DI DOTTORATO IN
FISICA, ASTROFISICA E FISICA APPLICATA

DIPARTIMENTO
MATEMATICA E FISICA

DOTTORATO DI RICERCA IN
FISICA, ASTROFISICA E FISICA APPLICATA
Ciclo XXIII

Self-assembly and electronic properties of macromolecular systems: ordered ultrathin porphyrin layers vs hierarchically assembled eumelanin thin films

Settore scientifico disciplinare FIS/03

Tesi di dottorato di:
Patrizia Borghetti
Matricola R07866

Coordinatore: Prof. Marco Bersanelli
Tutore: Prof. Luigi Sangaletti

A. A. 2009/2010

Contents

Abstract

The requirement to improve the performances of technological devices is closely connected to the size reduction of their components. The general interest in the development and manipulation of structures in the size range lower than 100 nm has stimulated the entire scientific community, laying the foundation for the current nanoscience and nanotechnology progress.

Altough the lithographic and photolitographic techniques have been initially employed with success for reducing the sizes of bigger components, the so-called "top-down approach" has soon manifested serious limitations in surpass the micrometric domain [1]. Thus, the critical topic in nanotechnology is producing structures larger than molecules, being aware that forms of organized matter more extensive than molecules cannot be synthesized bond-by-bond.

As many examples in history show, Nature may suggest extraordinary solutions to technological problems: in the specific miniaturization challenge, self-assembly is the way. Self-assembly is the autonomous organization of components into patterns or structures without human intervention [2]. Correspondingly, it represents the very strategy for fabrication of ordered aggregates in the domain from nanometric to micrometric.

In the case of organic compounds, a huge number of molecular systems are suitable for such an approach. These monomeric organic building blocks can be arranged in specific three-dimensional architectures, leading to the formation of new materials. The basic ideas are to preserve or even increase the activity of the starting molecular unit in the nano/micro-structured arrangement and to further control the macroscopic properties of the material in the 2-dimensioanl or 3-dimensional self-molecular packing.

Indeed, the route towards a complete understanding and expertise in developing complex and efficient nanodevices may be accomplished through the comprehension of the self-assembling behaviour of the highly symmetric molecules, since the symmetry often makes it easier to rationally design toward a desired architecture [3].

In this view, porphyrins constitue an appealing class of organic molecules

for nanotechnology applications. Large dipole moments, polarizability, nonlinear optical response, absorption spectrum, energy transfer and catalytic properties make porphyrins and metalloporphyrins extremely versatile materials for research projects in many branches of chemistry and physics, like electronics, opto-electronics, electrochemistry, catalysis and photophysics.

The interest in self-assembly, however, is not limited to the important role it may play in future technology. Moleculare self-assembly is crucial to the formation of lipids, DNA, proteins and many other biological systems, In other words, it represents the process by which a system of non-living chemical components become organized into a living cell.

One of the most impressive aspects in the conformation of these biological complexes are the hierarchical organization levels that compose their final structure [4, 5, 6]. The generation of the increasing complexity of these biological architectures relies on progressive build-up of more and more elaborated entities by multiple and sequential (i.e. hierarchical) self-organization steps, in which each step sets the base for the next one.

At each phase of the self-assembly, new functionalities may result as the "emerging" properties from the assembly of the building blocks [7, 8, 9]. Indeed, one of the goal of material physics and chemistry consists in enstablishing the relashionship between the structure appearing at each level of self-organization and the properties exhibited by the whole system. This study may ultimately leads to define the biological function of the complexes under investigation. The study of the structure-property relationships in biological self-assembly systems is also attractive for technological perspective, because it may suggest practical routes to implement new functionalities in artificial functional systems [4].

One of the most appealing organic macromolecule, both for medical and technologic perspectives, which displays self-assembly abilities is melanin. The melanin pigment is a polycyclic biopolymer spread out in nature, for which eumelanin is the predominant form. Eumelanin possesses physical and chemical properties very inviting for the materials science, such as the broad band monotonic absorption in the UV and visible [10], photoconductivity [11] and antioxidant abilities [12]. Despite many decades of reaserches, its chemical structure is largely unknown, which strongly contributes to the uncertainties related to its biological functions.

Based on STM imaging and Small Angle X-ray Scattering (SAXS) measurements [13, 14, 15], a hierarchical self-assembly model has been recently proposed for natural eumelanin, according to which its basic monomers constitute oligomeric stacked units that finally assemble into more and more complex nanometric particles and fibril-like structures [16]. Interestingly, although natural and sinthetic eumelanin seem to share the same stacked

protomolecular modules [13, 17, 18, 19], the synthetic coumpond lacks in the larger-size aggregates that characterize the natural pigment at nanometric scale [20].

The different level of hierarchical self-organization displayed by the two forms offers the unique opportunity to determine, on one side, the minimum supramolecular level that guarantees similar physical properties in both the pigments and, on the other side, the chemical factors that promote further aggregation steps in the natural compound.

The present thesis is focussed on the study of the structural and electronic properties of two self-assembling organic systems, the porphyrins and the eumelanin. Despite both compounds are composed of planar polycyclic units, the level of chemical and structural ordering displayed by the two systems is completely different. On one side, porphyrins molecules have a well-defined chemical composition, they can be studied in the isolated form and they are able to form 2-dimensional and 3-dimensional ordered nanostructures with coherence over impressive distances. On the other side, eumelanin in the condensed phase is an intrinsically disordered macromolecule because of the coexistence of several chemically distinct oligomers which cannot be isolated for experimental analysis. So far, no experimental evidence of the basic molecular unit of eumelanin has been reported. However, the most recent models and the results provided in this thesis support the model of a macrocyclic tetramer which would make eumelanin similar to porphyrins at a molecular scale.

The first part of this thesis is addressed to the self-assembly of porphyrin monolayers on metal/semiconducting surfaces. In Chapter 3, the interaction of a monolayer of Zn-tetraphenyl-porphyrin with Ag(110) and Si(111) is studied, showing that the adsorpion geometry and, consequently, the relative excited charge injection are dramatically different for the two considered surfaces. In Chapter 4, the formation of one monolayer of 2H-tetraphenyl-porphyrin (2H-TPP) on Ag(111) from multilayer thermal desorption is found to induce the de-hydrogenation of eight carbon atoms in the remaining monolayer and the rotation of the phenyl rings in a flat conformation. After assessing the chemical and structural properties of the 2H-tetraphenyl-porphyrin monolayer and multilayer on Ag(111), *in-situ* metalation of 2H-TPP with Fe atoms is reported, demonstrating the direct synthesis of FeTPP monolayer and multilayer in UHV conditions (Chapter 5). Following the same recipe as for the 2H-TPP, 2H-octaethyl-porphyrins molecules adsorbed on Ag(111) are shown to coordinate evaporated Fe atoms, forming FeOEP molecules (Chapter 6).

The second part of the thesis intends to provide a comprehensive analysis of the self-assembly properties of synthetic eumelanin in condensed phase at

different hierarchical levels. In Chapter 7, a model-protomolecule will be proposed as the minimum supramolecular level required to explain the electronic properties of eumelanin observed in core-electrons spectroscopy experiments. Chapter 8 is focussed on the aggregation behaviour of eumelanin thin films grown on conductive substrates for pure or K-doped samples. The clear influence of K ions in the eumelanin aggregation, as revealed by atomic force microscopy images and X-ray diffraction measurements, has triggered further studies of the effect of K on the electronic properties of K-doped eumelanin films. In Chapter 9 the electronic states ascribed to K-doping are identified and compared to first-principle calculations of the K-doped protomolecules.

The experimental work presented in this thesis has been carried out in the Surface Science laboratory at Università Cattolica del Sacro Cuore (Brescia, Italy), on the ALOISA, BACH and Gas Phase beamlines at the Elettra synchrotron source (Trieste, Italy) and in the μ-nano Carbon laboratory at Elettra (Trieste, Italy). The calculations presented in Chapter 4 have been performed within the collaboration with Stephan Blankenburg and Daniele Passerone from EMPA (Dübendorf, Switzerland), while theoretical results contained in Chapter 7, 8, 9 have been carried out within the collaboration with Ralph Gebauer and Prasenjit Ghosh from The Abdus Salam International Centre for Theoretical Physics (ICTP, Trieste, Italy).

Chapter 1

Introduction

1.1 Porphyrins

1.1.1 Porphyrin molecular properties

The porphyrins are a class of naturally occurring macrocyclic compounds, which play a very important role in the metabolism of living organisms. The common building block of these molecules is the porphine macrocycle that consists of four pyrrole rings linked via methine bridges, as depicted in Figure 1.1. Their planar aromatic macrocycle is optimal for $\pi - \pi$ stacking interactions and it is a versatile platform for peripheral tailoring with groups that can offer additional interaction sites [21]. Two distinct sites of substitution on the porphyrin ring are the four *meso* and the eight β positions (Figure 1.1).

The porphyrin nucleus is a tetradentate ligand in which the space available for a coordinated metal has a maximum diameter of approximately 3.7 Å [22]. When coordination occurs, two protons are removed from the pyrrole nitrogen atoms, leaving two negative charges. The porphyrin complexes with transition metal ions are very stable, e.g. the stability constant for ZnTPP (tetraphenylporphyrin) is 10^{29} [22]. Almost all metals form complexes 1:1 (metal ions:porphyrin), although Na, K, Li complexes are 2:1 in which the metal atoms are incorporated slightly below and above the porphyrin macrocycle plane. When divalent metal ions (e.g., Co(II), Ni(II), Cu(II)) are chelated, the resulting tetra-coordinate chelate has no residual charge. While Cu(II) and Ni(II) in their porphyrin complexes have generally low affinity for additional ligands, the chelates with Mg(II), Cd(II) and Zn(II) readily combine with one more ligand to form penta-coordinated complexes with square-pyramidal structure. Some metalloporphyrins (Fe(II), Co(II), Mn(II)) are able to form distorted octahedral with two extra ligand

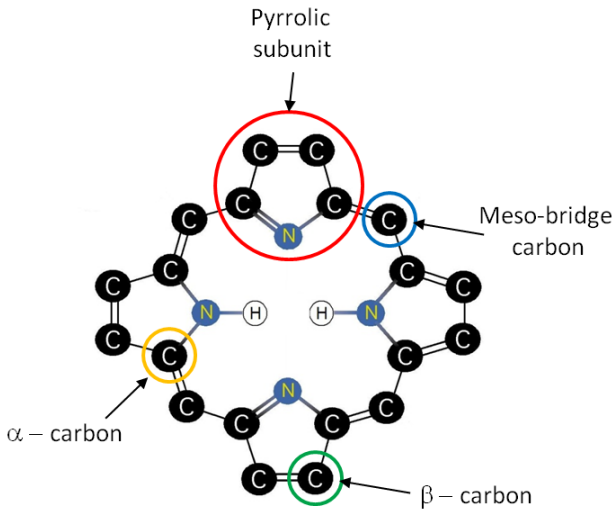

Figure 1.1: The porphine macrocycle.

molecules.

The metalloporphyrins hence offer a rich redox chemistry that renders this compounds of fundamental importance in living system processes. Amongst the porphyrin-based fundamental biological representatives:

- iron porphyrins are the prosthetic groups for the cytochromes, hemoglobins, etc., which provide dioxygen transport and storage and catalyze important redox reactions in biological systems [23];
- in chlorophyll, magnesium-porpyrin complexes are the basic reaction centers in which sunlight induces charge separation, starting the photosyntesis process;
- the structure of vitamine B-12 is based on the cobalt porphyrin and is necessary for the synthesis of red blood cells, the maintenance of the nervous system, and growth and development in children;
- nickel(II) and oxovanadium(IV) complexes of alkyl porphyrins are widely found in petroleum, oil shales and maturing sedimentary bitumen, encouraging the foundation for the modern science of porphyrin geochemistry [24].

The role of porphyrins in photosynthetic mechanisms indicates the high sensitive chromogenic reactivity of these molecules. Porphyrins exhibit characteristic strong and sharp absorption bands in the visible region. The so-called Soret band, located in the region from 400 to 500 nm, shows the

most intensive absorption (molar absorptivities of the order of 10^5 are often found). While variations of the peripheral substituents on the porphyrin ring often cause minor changes to the intensity and wavelength of the absorption features, the insertion/change of metal atoms into the macrocycle strongly affects the visible absorption spectrum [25].

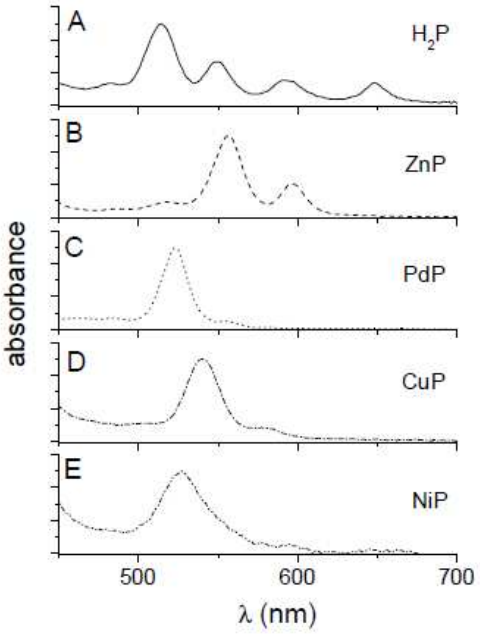

Figure 1.2: Absorption spectra of metallo-porphyrins with the macrocycle hosting different coordination metals. Figure from Ref. [25].

Thus, the possibility of tailoring the optical and electronic properties of porphyrins at molecular level has addressed the attention of the scientific community on the study of (metallo)porphyrins [21, 26, 27], porphyrin-metal interfaces [28, 29] and covalently linked donor-acceptor supramolecular porphyrin-based assemblies [30, 31] as materials for applications in opto-electronics, data storage, gas sensors and solar cells.

Very recently, $3d$-metal porphyrin have arised additional interest due to their magnetic properties. The possibility of altering the magnetic character of large molecules by deposition on metal surfaces has already been tested on Co and Fe phtalocyanines on Au(111) [32], for which the Kondo effect related to the central atom spin has manifested.

Lately, the magnetic behaviour of Fe(III)-octaethylporphyrin(OEP)-Cl molecules prepared by sublimation on ferromagnetic substrates (Co or Ni layers) has been investigated by using XMCD (X-ray Magnetic Circular

Dichroism) [33]. The authors have shown that, owing to an indirect, superexchange interaction between Fe atoms in the molecules and atoms in the substrate (Co or Ni), the paramagnetic molecules can be made to order ferromagnetically. Besides, the possibility to rotate the Fe magnetic moment along directions in plane as well as out of plane by a magnetization reversal of the substrate has been revealed. These experimental evidences indicate that specific porphyrins may be virtually used as switchable magnetic molecules for spintronics.

1.1.2 Porphyrin self-assembled monolayers

Porphyrins represent one of the most versatile class of organic compound for building nanostructures. On one hand, a large number of studies has been reported on the manipulation of porphyrins as isolated monomers or small oligomeric units, with interesting new applications that span from medical therapy [34] to artificial light-harvesting systems [21] and optoelectronic and photonic devices ([35] or see the review [3]). On the other side, well-defined porphyrin aggregates with high supramolecular chirality (like nanorods, nanorings, nanoparticles, nanowires, and nanotubes) have been produced, displaying intriguing chiroptical, sensoring and molecular recognition properties for industrial applications [27].

Yet, the most straightforward method to build nanostructures is to simply deposit the monomeric porphyrins onto single-crystal substrates, where the interaction between substrate and molecular thin film is sufficiently weak to prevent dissociative chemisorption. The attention on porphyrins at metal or semiconducting interfaces is growing in relation to the development of hybrid organic-inorganic electronic and optical devices such as OLEDs [36], thin film transistors [37] and solar cells [38]. In these molecular systems, the organic/inorganic interfaces play a fundamental role as they determine charge injection and charge flow and, therefore, the device performances [39]. For example, the surface modification of a semiconductor with an organic dye molecule can cause photoinduced charge injection from the dye into the semiconductor and therefore broaden the effective absorption region of the semiconductor. Thus, the possibility to tune the properties of these nanostructured systems is essential and, in case of organic/inorganic structures, can be straightforwardly achieved by exploiting the versatility afforded by organic molecular films. In fact, the considerable number of modes and conditions of deposition, chemical modification of materials, molecular mixing and doping allows to modify and improve interfaces in ways which cannot be applied to inorganic components [40].

In this perspective, porphyrin is one of the most attractive candidate as organic active center because the availability of a large variety of side groups and central metal ions that allows to specifically tune the molecule-substrate interaction [41]. Besides porphyrins have shown themselves amenable to the formation of square lattice monolayers, with coherence of the ordered monolayer over impressive distances.

This capability of producing ordered self-assembly monolayers (SAM) is the very base for the creation of organic/inorganic structures and eventually for the creation of well-defined organic/organic heterojunctions [30]. In fact, several advantages of the use of organic monolayers insted of multilayer films are recognized:

- in electrode-solution interfaces, the reduced molecular dimension of SAMs avoids slow diffusion of electro-active species;
- efficient charge injection occurs only at interfaces, i.e. only the layer in direct conctact with the substrate strongly contributes to the charge flow;
- whereas in the multilayer case, molecules are weakly bound and basically mantains the properties as in the isolated case, a strong interaction with the surface may further tune (and eventually enhance) the activity of the starting molecular unit.

Once the possibility of assembling a monolayer has been accomplished, the quality of the organic/substrate interaction crucially depends on the resultant molecular architectures [42, 43], i.e. on the orientation of porphyrin macrocycle and of its moieties with respect to the substrate surface. With regard to the porhine plane, the porphyrin molecules may adopt the two possible stacking styles of "face-on" and "edge-on" on a surface or in an interface [44, 45, 46]. In the case of "face-on", the porphyrin molecules lie on the surface by the molecular planes, while in the case of "edge-on", the planes of the porphyrin molecules are tilted from or perpendicular to the substrate. Whereas the "edge-on" stacking style optimizes the π-stacking interactions between the conjugated porphyrin rings, the "face-on" mode exalts the interaction between the molecular plane and the inorganic surface. A detailed understanding of the adsorption geometry of porphyrins on a variety of surfaces is therefore key to progress in the nanotechnology area.

In this regard, NEXAFS (*Near Edge X-ray Absorption Fine Structure*) spectroscopy is the most powerful tool in determining the geometry of the adsorbed molecules. As it will be discussed in details in Chapter 2.1, from the polarization dependence of the intensity of a particular resonance, the

angle between the associated molecular bond and the direction of the X-ray polarization vector can be obtained quantitatively. The case of porphyrin is straightforward: the π^* states generated by the four central nitrogen atoms belong to a combination of atomic-like p_z orbitals that lie perpendicular to the plane containing the aromatic frame, therefore from its polarization dependence the porphine orientation with respect to the substrate plane is calculated (see Chapter 3, 4, 5, 6).

The polarization dependence of NEXAFS spectra has been largely exploited for determining the orientation of many organic molecules (a large overview is contained in [47]) and in particular of phthatolacyanines [48, 49, 50] which share with porphyrin the macrocyclic conformation of the four pyrrole-like subunits. Despite this fact, so far only a few works on the orientation of porphyrin layers by means of NEXAFS measurements have been published. For example, Goldoni and co-workers reported that in multilayer the ZnTPP macrocycle forms an angle of $5° \pm 5°$ with the Si(111) surface [26] whereas in the ZnTPP/C_{70} double-layer heterojunction the adsorption geometry of ZnTPP molecules on C_{70} has been pecisely determined [30].

In most articles on porphyrins, the configuration of the molecular plane has been estimated by means of Scanning Tunneling Microscopy [51] or optical spectroscopies (such as infrared reflection absorption spectroscopy [52], reflectance anisotropy spectroscopy [53], surface plasmon (SP) enhanced fluorescence spectroscopy [54], UV-VIS absorption spectroscopy) [55]. These methods, however, allow for clear interpretation of data only in the "face-on" stacking style, whereas in case of "edge-on" stacking style no quantitative results on the tilt angle of the molecular plane can be obtained.
Moreover, the direction of peripheral groups can rarely be inferred by means of these techniques. This information indeed can be achieved in several porphyrin systems by means of NEXAFS measurements.

Specifically, when the electronic states of the substituent groups scarcely interact with those of the macrocycle, i.e. when peripheral groups and the porphine are not conjugated, one may consider that the NEXAFS spectra of the whole molecule are the superposition of those of the aromatic building blocks, whose polarizazion dependence can be analyzed separately (see [47], Chapter 6). This is observed, for example, when porphyrins have meso-aryl substituents, as, e.g., in the case of 2H-TPP (Chapter 4).

The characterization of the adsorbate arrangement on single crystal surfaces is just the preliminary step for inspecting charge transfer dynamics, which is at the very base of molecular charge-injection devices. One possibility to check the degree of interaction between the substrate and the molecular adlayer is the resonant photoemission spectroscopy (ResPES) [56]. This method is complement to the pump-and-probe technique, with an in-

trinsic timescale based on the lifetime of the intermediate (core-hole) state, leading to the descriptive name "core hole-clock" method (For a more exhaustive description of ResPES technique see Chapter 2.2). The possibility to access faster processes with detailed element and site specific informations makes resonant photoemission preferred in many cases with respect to pump-and-probe technique.

Whereas several laser pump-probe studies on porphyrin in solution have been published (e.g. see Ref. [57, 58]), only a few works on charge transfer dynamics at porphyrin/inorganic interface probed by ResPES have been reported. To date, de Jong *et al.* have studied charge transfer dynamics between a monolayer of Fe(II)-tetraphenylporphyrin(TPP)-Cl molecules and molybdenum disulfide substrate [59]. In particular, they found that the efficiency of charge transport across the interface is found to be different for the individual molecular electronic subsystems (i.e. macrocycle and phenyls) and for each they estimated the time for excited electrons to be transferred to the substrate. They also underlined that, in order to distinguish molecule-substrate charge transfer from hopping between molecules, a comparison between the spectral results for the multylayer and monolayer case is necessary. In this thesis, the interaction of one single layer of ZnTPP with Ag(110) and Si(111) sufaces will be analysed (Chapter 3). In particular, after the comparison to the multilayer ResPES data (recently published by Goldoni *et al.* [30]), it will be shown that coupling of the phenyl legs with the substrate and the relative excited charge injection are dramatically different for the two considered surfaces.

1.1.3 Metalation of porphyrins

Typically, the inclusion of metal atoms in porphyrin molecules is obtained via chemical reaction in solvents. The most prominent representatives of the so-called metalloporphyrins are the iron porphyrins, with a Fe(II) ion complexed to the four nitrogen atoms in the center of the conjugated ring system. These molecules play a key role in a number of oxidative catalytic processes, including biological systems.

Iron porphyrins can undergo reversible redox reactions and are very sensitive towards oxidation [60]. Hence, they are very difficult to handle and to sublimate as a pure compound. So far the commercially available porphyrins with a Fe atom at the center of the macrocycle also have Cl attached to the iron atom to stabilize the highly reactive metal that can easily oxidizes [61]. The possibility to produce stable Fe-porphyrins with no Cl atoms and characterize them in situ is an intriguing challenge and of fundamental interest due to their key role as main building blocks in important biological

molecules such as cytochrome P-450 [62] and haemoglobin [62], [63], as well as for magnetic systems [64] and catalytic processes [65].

Recently, it has been shown that pure Fe-Tetraphenyl porphyrin (Fe-TPP) can be produced under UHV conditions by *in situ* metalation of free-base 2H-5,10,15,20-Tetraphenylporphyrin (2H-TPP) monolayers with Fe atoms, that are deposited using an electron beam evaporator [66]. In this experiment STM micrographs with sub-molecular resolution are presented, showing the appearance of intra-molecular protrusions consequent to Fe evaporation. These protrusions have been addressed as an evidence of the metalation of the TPP. Moreover, photoemission studies, performed with laboratory X-ray sources, showed evidence of metalation by Fe, Zn, Co and Ce of free-base tetraphenyl porphyrins collecting the N $1s$ core level signal together with the metal peak [67, 68]. Similar metalation experiments have been also performed on free-base phtalocyanines [69]. These studies have demonstrated that metals can efficiently be coordinated to adsorbed porphyrin and phtalocyanine layers by evaporation of metal atoms in situ under clean UHV conditions. This approach represents a possible route toward the production of unavailable porphyrin materials, using the facile and energetically favorable capabilities of a direct metal-to-molecule coordination [70] as well as an access to low-dimensional metal-organic architectures and patterned surfaces, which cannot be achieved by other conventional methods.

Therefore, the complete understanding of the coordination mechanisms is of straightforward interest. Although there are several studies on this subject, in particular related to Fe metalation of tetra-phenyl porphyrins, the model of the molecular structural configuration and adaptation onto the substrate surface needs to be refined likewise the study of the single layer has to be clarified from the core level spectroscopy point of view before and after the metalation. In particular, much less attention was devoted to the interface adsorption geometry and the multilayer molecular orientation. The possible distortion of the macrocycle and how the electronic structure will change after the metalation have never checked in details. Moreover, based on both experimental and theoretical data, the monolayer metalation process was explained with the substrate surface mediated diffusion of the metal to the reaction site [71, 51, 72, 73], although this model seems inadequate for phtalocyanine overlayers which form a compact wetting layer, covering the whole substrate [69].

In the present thesis, an extensive characterization of the electronic states and the molecules geometrical adaptation during the synthesis of a pure 2H-TPP and FeTTP layers on Ag(111) single crystal will be reported (Chapter 5). Besides, the first study of *in-situ* Fe metalation of octaethylporphyrin (2H-OEP) will be presented (Chapter 6).

1.2 Eumelanin

1.2.1 Eumelanin basic properties

Among biomolecular systems, melanins represents a class of biological pigments widely spread in nature. Melanins can be divided into four categories: eumelanin, phomelanin, neuromelanin and allomelanin [74, 75]. Eumelanin is the black, nitrogen-containing pigment that is the predominant form in humans. It is synthetized in special cells called melanocytes and is found in skin, hair, eye and in the inner ear.

The well proven photoprotective role of eumelanin [76] has a clear counterpart in the broad band monotonic absorption in the UV and visible displayed by the macromolecule in solution [77]. Wolbarsht *et al.* [10] noted that this featureless, broad spectrum is a uniqueness amongst organic chromophores, which normally consist of discernible peaks reflecting transitions between individual and distinct electronic states and/or satellite vibronic states. For a direct comparison, the structured absorption spectrum of porphyrin has been reported in section 1.1.1.

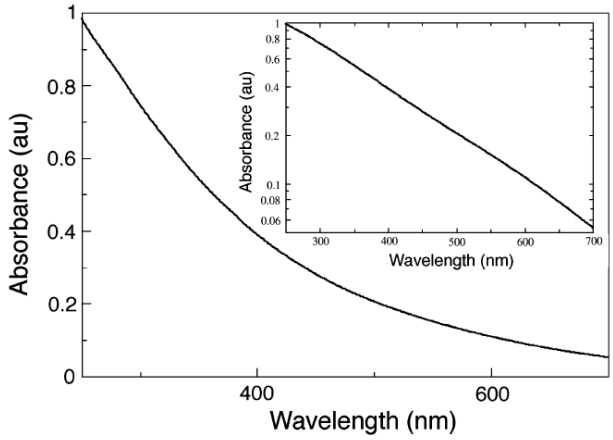

Figure 1.3: The monotonic, broad band UV-visible absorption spectrum of (synthetic) eumelanin. No distinct chromophoric peaks are observed. Figure from Ref. [77].

Defence from solar radiation is further guaranteed by the fact that the majority of absorbed energy is dissipated non-radiatively within a nanosecond of excitation [78]. In fact, the very efficient thermal relaxation mediated by melanin [79, 80, 81] allows to reduce the risk of potentially damaging photochemical reactions. Beyond being a sunlight filter, eumelanin has been recognized to act as anti-oxidant and as free-radical scavenger [12], protecting the body against free-readical damage.

Eumelanin, and melanins in general, exhibits a very peculiar set of condensed phase electrical properties with respect to other bio-organic materals: it displays electrical conductivity and photoconductivity [11], as well as threshold and memory switching [82], specific of amorphous semiconductors. These experimental evidences have suggested that melanins may represent a novel class of functional materials for electronics and photovoltaic applications [83].

Nevertheless, there is a great uncertainty concerning absolute electrical conductivities, activation energies and even the sign of the charge carrier, and the mechanism of charge generation and transport is still subject of debate (for a complete review, see Ref. [84]). Rosei *et al.* [85] described melanin as a network of nanometre-size conjugates clusters where the generation of electron-hole pairs, subsequently dissociated via thermalization, is in competition with trap and geminate recombination (i.e. recombination of free charge carriers with trap states or self-recombination).

Jastrzebska *et al.* have reported that the electrical conductivity in melanin highly varies with humidity, ranging from 10^{-13} to 10^{-5} S/cm, i.e. from a strong insulating to a moderate conducting state [86]. Thus, the water content of the samples plays a fundamental role in the mechanism of conductivity. Water is thought to exist in two forms within the materials, one adsorbed on the surface and the other contained between the protomolecular layers of the macromolecule [87]. The water on the surface is weakly bound and can easily removed by heating samples above 100°C, whereas several hundred degrees are required to remove the water trapped in the macromolecular skeleton [88].

Clearly, eumelanin may be of some use as a functional material in photovoltaic and sensoring applications only if the correct description of its intriguing mesoscopic properties is achieved. Since these properties are primarly determined by the molecular and supramolecular structure, the correct structural model must in turn be available.

1.2.2 Macromolecular structure

In spite of the importance of eumelanin from a biological and medical perspective, that has motivated many decades of research from biochemists and the biology community [89, 90, 91], the structure, composition and aggregation behaviour of this class of pigments in the condensed phase is far from being thoroughly elucidated. This is in part due to the fact that melanins are difficult molecules to study because they are chemically and photochemically stable and are virtually insoluble in most common solvents [92].

Eumelanin is known to originate from the oxidative copolymerization of

5,6-dihydroxyindole (DHI, also known as dihydroxyindole (HQ)) and 5,6-dihydroxyindole-2-carboxylic acid (DHICA) [93]. Their oxidative forms - quinone-imine (QI) and indolequinone (IQ) - are also included in the system [94], but the details of the connectivity of the basic monomers remain one of the major questions (Figure 1.4).

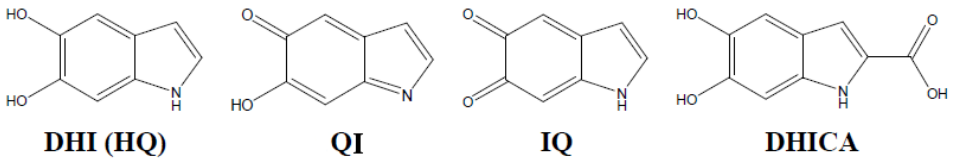

Figure 1.4: 5,6-dihydroxyindole (DHI), its oxidized forms (QI and IQ), and 5,6- dihydroxyindole, 2-carboxylic acid (DHICA): the key monomeric building blocks of eumelanin. Figure from Ref. [77].

Recently, the oligomeric model, which is based on STM imaging and Small Angle X-ray Scattering (SAXS) measurements [13, 14, 15], has gained larger consensus in explaining physical and chemical properties of this chromophore. According to this model, **(i)** four to six monomers are brought together to consitute a planar protomolecule, then **(ii)** the eumelanin basic building block is formed by 3-4 of these protomolecules which are stacked through $\pi-\pi$ interactions in a "graphitic-like structure". This fundamental aggregate, the oligomer, measures $\approx$ 15 Å in lateral size and $\approx$ 12 Å in height, while the distance between the planes is estimated to be $\approx$ 3.5 Å, similar to that of graphite. The first two steps in eumelanin agglomeration are sketched in Figure 1.5. The AFM, STM and SEM imaging have shown that there are at least three additional levels of morphologic assembly in natural eumelanin, each with a definite length scale: **(iii)** small units with lateral dimensions of 10-20 nm and **(iv)** round-shaped corpuscles of 150 nm in diameter, as shown in Figure 1.6. Finally, **(v)** these granules can aggregate in larger agglomerates with variable morphology and size, depending on the biological environment. This bottom-up structural organization, starting from indolic monomers to sub-micrometric aggregates, has been summed up by Clancy *et al.* in the so-called hierarchical self-assembly model for natural melanin [16].

In summary, this model starts from the oligomeric building block to explain the formation of the nano/micro-metric structures observed at different scales. Each of these diverse levels of aggregation is likely to play an important role in the range of chemical and photochemical properties exhibited by eumelanin. However, the very starting point for the construction of consistent structure-property-function relationships has to be found in the

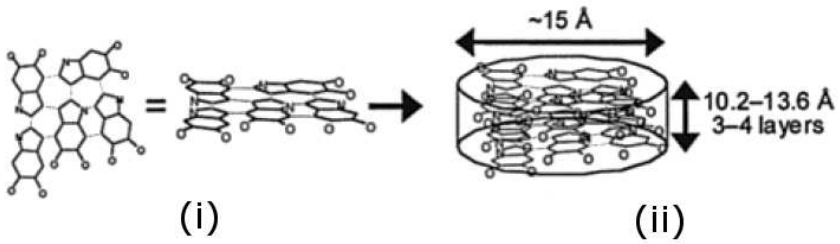

Figure 1.5: The first two steps in eumelanin assembly according to the hierarchical self-assembly model: (i) the constitution of the planar protomolecule from monomers, (ii) the stacking of the 3-4 protomolecules to obtain eumelanin basic oligomer. Figure from Ref. [16].

chemical structure of protomolecules. In this regard, the key word is "chemical disorder", indicating that each of the protomolecules building the basic oligomer may have a different chemical composition, i.e. a different weighted mix of monomers and/or a different chemical bond arrangment.

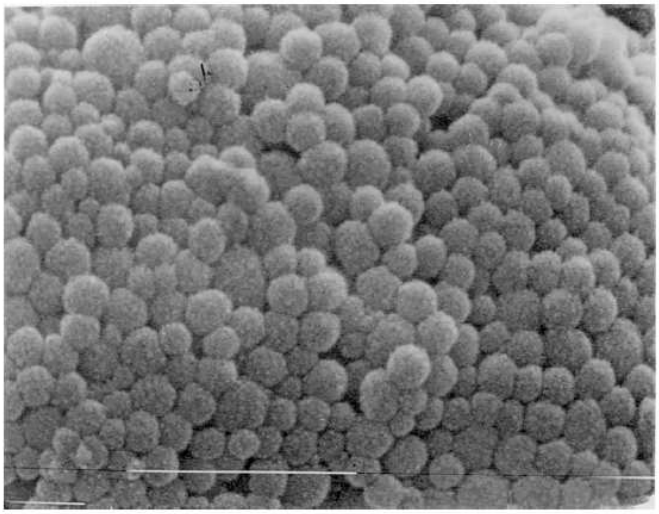

Figure 1.6: SEM image of eumelanin from Sepia officinalis (× 56.000), which is constituted of speherical particles of 150 nm in diameter. White portion of black and white dashed line is 714 nm. Figure from Ref. [20].

The coexistence of different building blocks and polymerization effects between different or like monomers have important consequences on the electronic properties of eumelanin and may explain some of the unique characteristics of this pigment. For istance, Meredith *et al.* [77] suggested that the superposition of a large number of transitions associated with each of the com-

ponents of the ensemble may result in a rather broad spectral weight, without the sharp features characteristic of molecular levels of isolated molecules. This would also explain why, until very recently, there has been no direct observation of an energy gap in condensed phase eumelanin. Moreover, the relatively small radiative quantum yields could also result from the presence of several species with slightly different HOMO-LUMO gaps that create an emission-reabsorption cascade and thus the near unity non-radiative conversion of any absorbed photon [77].

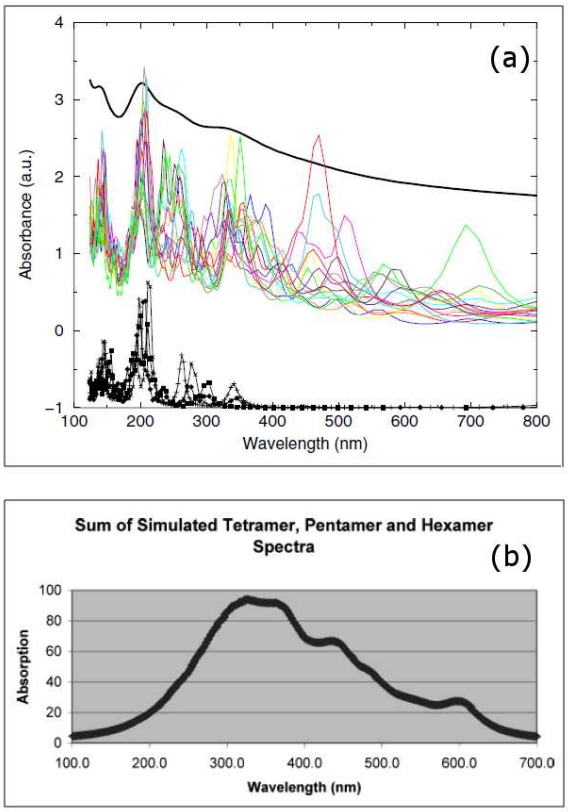

Figure 1.7: (a) Absorption spectrum of the superposition of 16 tetramers with a porphyrin-like ring (thick black line, shifted up by 1.5 units for clarity). Individual tetramer contributions are given by the thin colored lines. Monomer spectra are also shown (shifted down by 1 unit for clarity). Figure from Ref. [95]. (b) Linear combination of one simulated tetramer, one pentamer and one examer absorption spectra from Ref. [96].

Polymerization is therefore recognized as a central issue in the study of the electronic structure of melanins, to such an extent that recent experimental studies have been carried out with the aim to grow single crystals containing eumelanin monomers by inhibiting the polymerization through the addition

of suitable side groups [97].

First-principles density functional calculations of the electronic structure of the melanin monomers [98, 99] have been published only recently. Even if synthetic methods of preparing isolated monomers of DHI are available, it is not simple to test these calculations because these molecules are highly unstable and spontaneously polymerize in an oxidizing environment. A further step in first-principles quantum mechanical calculations of eumelanin costituents has been made by Kaxiras and co-workers, who have lately proposed a model for protomolecules [95]. Accounting for melanin ability to capture and release metal with a metal-ion binding capacity of one ion per 3-4 monomer units [100], they have sequenced eumelanin monomers in order to create an inner ring where all the N atoms reside, in analogy with the porphyrin structure. Tetramers and pentamers result to be the only stable forms, with a slightly preference for tetramers. Besides, thay have shown that the superposition of the calculated absorption spectra of 16 possible arrangements of individual monomers reproduces accurately the experimental featureless absortpion spectrum of eumelanin, even if the individual tetramer spectra have sharp features (see Figure 1.7-a). However, Stark et al. [96] had already reported that a linear combination of spectra of some tetramers, pentamers and hexamers (with no inner porphyrin-like ring) equally reproduces the large band of the eumelanin absortpion spectrum, as shown in Figure 1.7-b. Therefore, absortpion spectrum is not a definitive probe of the molecular structure and, least of all, of the electronic structure of eumelanin.

Recently, ab initio calculations of the electronic structure on single monomers have been published by Sangaletti *et al.* [101]. In the same paper, the feasibility of soft X-ray spectroscopy measurements of electronic properties of eumelanin in condensed phase has been tested by studying synthetic eumelanin powders dispersed in water droplets deposited onto copper substrates. The comparison of experimental data of the occupied and unoccupied valence states to the calculated electronic structure of single monomers shows that, althought the main spectral features of solid state aggregates are catched, the extension of computational codes to macromolecules is required for accounting for polimerization/hybridization effects occurring in the macromolecule.

1.2.3 Natural eumelanin and synthetic eumelanin.

Natural melanin pigments are a mixture of eumelanin and pheomelanin [102]. For experimental analysis, Sepia melanin is considered to be a model system for natural eumelanin, being the content of the black pigment $> 99\%$ [76].

Natural eumelanin (and melanins in general) is found to be firmly bound to proteinaceous components through covalent or ionic bonds [103]. Thus, it

is important to remove the protein component in order to study the physical properties of the melanin biopolymer. Despite several purification methods to isolate melanin from the bound protein are available, usually residual protein fragments are not completely removed during the isolation and purification procedure [92].

The unwelcome presence of proteins in eumelanin samples may be prevented if synthetic eumelanin analogues are employed. Two procedure are commonly used for producing synthetic eumelanin: the autoxidation of L-DOPA and and the enzymatic oxidation by Tyrosinase [104]. Even if the first method avoids variations in the sample properties due to the variable characteristics of the involved enzyme, the second procedure has to be preferred when comparison with natural melanin properties is demanded.

The main difference between natural and synthetic eumelanin is found in the DHI vs DHICA content. As reported in the seminal paper of Ito [93], while the enzymically prepared eumelanin only contains *c.* 10% DHICA, intact natural melanins can contain up to 50% of the carboxylated form. This may have profound implications in the redox activity of the macromolecule, as well as in the coordination of metal ions, as will be discussed in section 1.2.4.

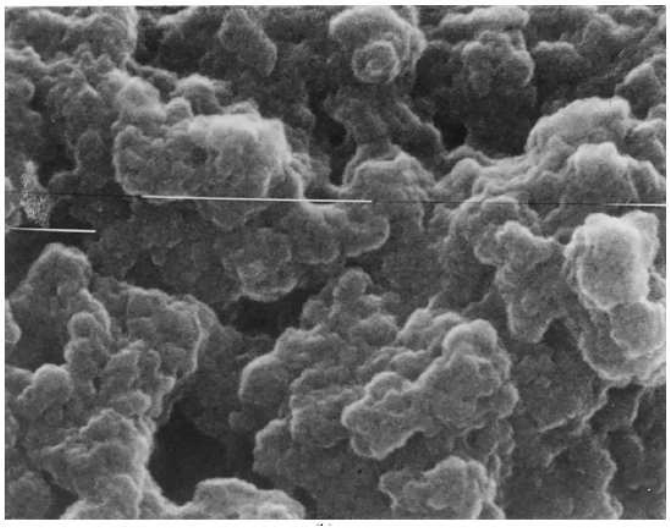

Figure 1.8: SEM image of synthetic eumelanin (× 48.000), which appears as an amorphous conglomerate. White portion of black and white dashed line is 830 nm. Figure from Ref. [20].

With regard to the structural properties, X-ray diffraction [17], scanning tunnelling microscopy (STM) [13] and mass-spectroscopy [18, 19] measurements reveal that synthetic tyrosine melanin is characterized by the same

inter-planar distance of $\approx$ 3.5 Å and is composed by the same structural oligomeric entity of $\approx$ 12 Å as the natural melanin. Nevertheless, SEM imaging clearly showed that, on a microscopic scale, synthetic eumelanin occurs as an amorphous conglomerate and no regular shaped elements can be singled out [20]. This is evident from Figure 1.8.

Despite some alterations in chemical and structural characterics occur in synthetic eumelanin with respect to the natural compound, both pigments display the same behaviour in absorption, fluorescence, conductivity and photoconductivity features, i.e. in the set of appealing properties that may be exploited for electronic, sensing and photovoltaic devices design. This encourages the investigation of synthetic eumelanin properties, being the artificial compound easier to handle in view of a possible large-scale employment.

1.2.4 Eumelanin and metals.

The ability of eumelanin to capture, release and accumulate metals has been well documented (for a complete review, see Ref. [105]). Mg(II), Ca(II), Na(I), K(I) and almost all the first row transition metals are normal constituents of Sepia melanin, which has been considered one of the best model for natural eumelanin. Importantly, synthetic eumelanin, whose protein content is negligible, reveals metal affinities similar to those of the natural pigment, indicating that proteins in melanin have only minor effects on metal binding [105].

The high binding capacity and affinity for metal ions is related to the chemical structure of this pigment that offers the carboxylic (COOH), hydroxyl (OH) and amino (NH) groups as potential metal binding sites. Incidentally, a model for the eumelanin planar protomolecules has recently been proposed in which four eumelanin monomers are arranged to form an inner porphyrin-like ring that would naturally account for eumelanin ability to capture and release metal ions [95].

In natural melanin, pH-dependent studies have suggested that the alkali and alkaline earth cations bind to carboxyl group, whereas Fe(III) is likely complexed with phenolic OH groups [100]. A comparative study for both Sepia melanin and synthetic DHI melanin has been conducted on the coordination of Zn(II): whereas in the biological sample Zn(II) shares the same site as Mg(II) and Ca(II) [106], in the synthetic material, IR analysis reveals that zinc is more inclined to bind to imine sites [107]. These variations are ascribed to the diverse chemical structure of the two sample, i.e. the concentration of COOH group in synthetic eumelanin is minor, as highlighted in section 1.2.2. This underlines that the experimental results for natural eumelanin can't apply straightforwardly to synthetic eumelanin.

One interesting point is to establish the effect of metal binding on melanin electronic and structural properties. In living systems, melanin is synthetized in a saline enviroment, thus it is an ambitious task to determine the very role of metal ions in melanin aggregation. However, experimental evidences have shown that when natural melanin solutions are ultra-sonicated, metal ions have an important role in promoting melanin re-organization [108]. While cations occur in natural melanin already in the synthesis stage, for synthetic melanin films they are introduced during the deposition process. So far, only one study has been reported on doping of synthetic eumelanin, where Fe-doped thin films grown by electrodeposition showed self-assembling [109]. However, it is not clear if this behaviour is due to the presence of cations or to the deposition technique employed, because comparison with other deposition techniques is not reported.

Concerning the electronic structure, X-ray spectroscopic studies have been conducted only recently on ion-free synthetic eumelanin films [110, 101], but, to the best of our knowledge, the electronic structure of melanin containing metal ions has not yet been explored with soft X-ray electron spectroscopy such as photoemission and X-ray absorption.

Chapter 2

Experimental Techniques

2.1 Near Edge X-ray Absorption Fine Structure

2.1.1 Introduction

The X-ray absorption near edge structure or, for short, XANES technique is a powerful tool for the study of unoccupied electronic states in molecules, inorganic complexes, biological system, crystalline and disordered solids and chemisorbed atoms and molecules. By sweeping the X-ray photon energy over the ionization edge, XANES selects a specific atomic species and *maps* its bond to intra-molecular and extra-molecular (surface atoms) neighbors. Whereas the term XANES is more commonly used for solids and inorganic complexes, NEXAFS (*Near Edge X-ray Absorption Fine Structure*) is used in conjunction with surface and specifically for K-shell excitation spectra of low-Z molecules (composed of hydrogen, carbon, nitrogen, oxygen and/or fluorine atomes).

The absorption of electromagnetic radiation in the energy region just below and up to about 50 eV above the absorption edge excites the core electrons into unoccupied bound or continuum states, levaing a vacancy (Figure 2.1, left). The X-ray absorption can be probed either directly by monitoring the attenuation of the X-ray intensity passing though the sample, or indirectly by measuring the intensity of the secondary process, e.g., Auger emission or X-ray fluorescence. However, for low-Z molecules, the Auger electron yield is much higher than the fluorescence yield. In the two-stage Auger process, an electron from higher energy levels relaxes to the core level vacancy, tranferring the energy to another electron, which is ejected fromt the atom, as displayed in Figure 2.1, right.

Incidentally, electron detection provides the higher surface sensitivity for low-Z molecules because the mean free path in matter is tipically less than 1 nm for electrons of kinetic energies between 250 eV and 600 eV.

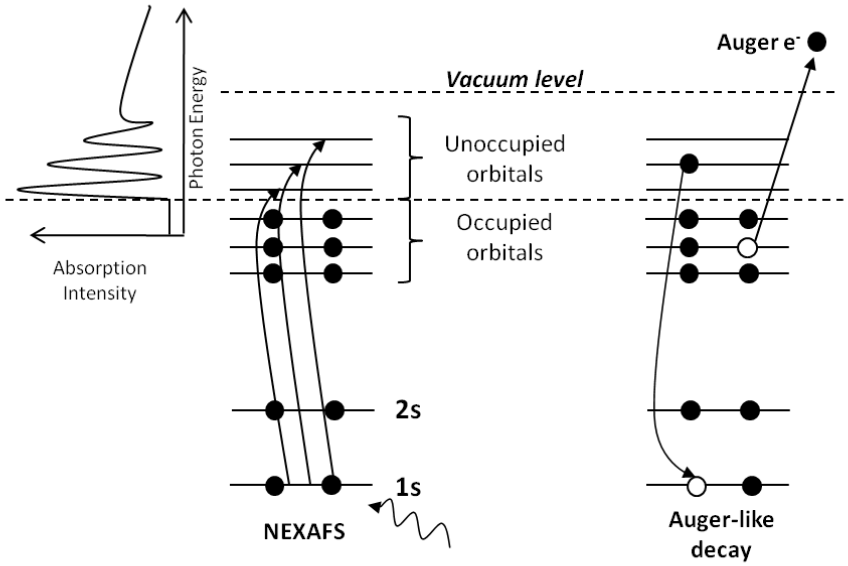

Figure 2.1: Schematic of the NEXAFS process with the corresponding spectrum (left) and the subsequent Auger emission (right).

Besides, the absorption process is strongly affected by the symmetry of the orbitals of the initial and final states. Using linearly polarized X-rays, the non-ionizing transitions may exhibit angular dependence on the direction of the electric field associated to the light beam, i.e., *linear dichroism*. Thus, one can determine in principle the orientation of the bonds determined by the symmetry of orbitals, and consequently molecular orientation in space. In the discipline of molecular thin film growth this is a very efficient method for investigating the geometry of the adsorbed molecules and self-assembling properties of complex molecular systems.

2.1.2 The X-ray absorption cross-section

The cross section of the X-ray absorption derives from the Fermi's "Golden Rule" for the transition probability per unit time P_{if} from a state $|i\rangle$ to a state $\langle f|$ [47]. The harmonic time-dependent perturbation $V(t) = \overline{V}e^{i\omega t}$ drives the process:

$$P_{fi} = \frac{2\pi}{\hbar} \left|\langle f|\overline{V}|i\rangle\right|^2 \rho_f(E), \tag{2.1}$$

where $\rho_f(E)$ is the energy density of the system's final state. The total X-ray absorption cross section at a given photon energy can be obtained by summing over all the shells with binding energy lower than $\hbar\omega$. However, since we are mainly interested in the partial absorption cross section of inner shells and all electrons in the outer shells have a smooth cross section in the range of inner-shell excitation energies, the cross section contribution from the outer shells will be neglected. The inner shell excitation is induced by an electromagnetic wave with electic field vector $\mathbf{E}$. Using the Coulomb gauge [111] the corresponding vector potential $\mathbf{A}$ is given by

$$\mathbf{E} = -\frac{1}{c}\frac{\partial \mathbf{A}}{\partial t}. \tag{2.2}$$

The vector potential can be written in the form of a plane electromagnetic wave of wave vector $\mathbf{k}$, frequency ω, and unit vector $\mathbf{e}$

$$\mathbf{A} = \mathbf{e}A_0 \cos(\mathbf{k}\cdot\mathbf{x} - \omega t) = \mathbf{e}\frac{A_0}{2}\left(e^{i(\mathbf{k}\cdot\mathbf{x}-\omega t)} + e^{-i(\mathbf{k}\cdot\mathbf{x}-\omega t)}\right). \tag{2.3}$$

The wave vector is related to the frequency ω and to the X-ray wavelenght λ according to $|\mathbf{k}| = \omega/c = 2\pi/\lambda$. The second exponential term which represents photon emission may be omitted in further calculations because we are only interested in absorption. Eq. 2.2 and Eq. 2.3 indicate that $\mathbf{A}$ and $\mathbf{E}$ are collinear in space and their magnitudes are related by $E_0 = A_0\omega/c$. The perturbative term in Eq. 2.1, which represents the interaction of a spinless particle of charge $-e$ and mass m with an electromagnetic field is given by

$$V(t) = \frac{e}{mc}\mathbf{A}\cdot\mathbf{p}, \tag{2.4}$$

where $\mathbf{p} = \sum \mathbf{p}_i$ is the sum of the linear momentum operators of the individual electrons. If we combine Eq. 2.4 and 2.3 with the Fermi's "Golden Rule" 2.1, we get for the transition probability per unit time

$$P_{fi} = \frac{\pi e^2}{2\hbar m^2 c^2} A_0^2 \left|\langle f|e^{i\mathbf{k}\cdot\mathbf{x}}\boldsymbol{\epsilon}\mathbf{p}|i\rangle\right|^2 \rho_f(E). \tag{2.5}$$

According to the *dipole apporximation*, for $\mathbf{k}\cdot\mathbf{x} < 1 \Rightarrow |\mathbf{x}| < \lambda/2\pi$, where $|\mathbf{x}|$ is the estimation of the K-shell diameter, the equation is simplified by retaining only the first term in the expansion. In our case, for example, the excitation of the carbon K-shell occurs at $\hbar\omega = 284$ eV, therefore $\lambda/2\pi = 7.0$ Å. The K-shell diameter of the carbon $|\mathbf{x}|$ is estimated from the Bohr radius $a_0 = 0.53$ Å and the atomic number Z as $|x| \approx 2a_0/Z = 0.18$ Å. The dipole approximation is therefore well satisfied. Since the X-ray absorption cross

section σ is defined as the number of electrons excited per unit time divided by the number of incident photons per unit time per unit area, i.e.,

$$\sigma = \frac{P_{fi}}{F_{ph}} \tag{2.6}$$

the photon flux F_{ph} associated with the plane wave in Eq. 2.3 shall be first determined. This is given by the energy flux of the electromagnetic flux of the electromagnetic field [47] divided by the photon energy:

$$F_{ph} = \frac{E_0^2 c}{8\pi\hbar\omega} = \frac{A_0^2 \omega}{8\pi\hbar c}. \tag{2.7}$$

The final result for the X-ray absorption cross-section in dipole approximation is:

$$\sigma = \frac{4\pi^2\hbar^2}{m_2}\frac{e^2}{\hbar c}\frac{1}{\hbar\omega}\left|\langle f|\boldsymbol{\epsilon}\cdot\mathbf{p}|i\rangle\right|^2\rho_f(E). \tag{2.8}$$

The absorption cross section crucially depends only on the product $\langle f|\boldsymbol{\epsilon}\cdot\mathbf{p}|i\rangle$. Putting photon polarization vector in front of the bracket, we get the matrix element of the dipole transition $\langle f|\mathbf{p}|i\rangle$ expressed in momentum space. Moving to the coordinate space, we consider the equivalent operator

$$\mathbf{p} = -i\hbar\nabla = \frac{im(E_f - E_i)}{\hbar}\mathbf{r}. \tag{2.9}$$

By using the dipole operator $\boldsymbol{\epsilon}$ instead of $\mathbf{r}$, where μ=e$\mathbf{r}$, we write the final expression for the dipole matrix element

$$D_{if} = \langle f|\boldsymbol{\mu}|i\rangle. \tag{2.10}$$

The transition intensity I_{if} depends also on the X-ray polarization direction ϵ and according to Eq. 2.6 is expressed as

$$I_{if} \propto \left|\langle f|\boldsymbol{\epsilon}\boldsymbol{\mu}|i\rangle\right|^2 = \left|\boldsymbol{\epsilon}\langle f|\boldsymbol{\mu}|i\rangle\right|^2 = \left|\boldsymbol{\epsilon}D_{if}\right|^2. \tag{2.11}$$

For discussion of transition to bound states and intensity of resonances it is sometimes introduced the *optical oscillator strenght* f which is related to the X-ray absorption cross section according to [112]

$$\sigma(E) = C\frac{df}{dE}, \tag{2.12}$$

where $C = 2\pi 2e^2\hbar/mc$. Since f is the energy integral of the cross section, the oscillator strength is a measure of the intensity of a resonance

$$f = \frac{2}{m\hbar\omega}\left|\langle f|\boldsymbol{\epsilon}\cdot\mathbf{p}|i\rangle\right|^2. \tag{2.13}$$

The oscillator strength for bound state transitions can be converted to cross section by introducing a bound state energy density of final states $\rho_b(E)$:

$$\sigma(E) = Cf\rho_b(E). \tag{2.14}$$

In a cross section versus energy graph the height of a bound state resonance is given by σ and the width by $1/\rho_b$. The oscillator strength is then equal to the area of the resonance peak.

2.1.3 Polarization dependence

The polarization dependence of the intensity of a particular resonance can be derived from the espression for the transition intensity in Eq. 2.11 and is based on the concept that bonds and associated MOs (Molecular Orbitals) in molecules are strongly directional.
The discussion will be restricted to K-shell excitation, being the main interest in the present thesis. The initial state $|i\rangle$ is to a very good approximation represented by the atomic $1s$ wavefunction of the excited atom in the molecule. It is spherically symmetric and can thus be represented by the function $|i\rangle = R_{1s}(r)$. In one-electron model, the final molecular state of the transition can be represented by a corresponing *linear combination of atomic orbitals* (LCAO). Despite of being a rough simplification, the LCAO is one of the simplest, yet succesful way to matematically construct the electron wave functions in molecules. For Z-low molecules the discussion is confined to atoms from the second row in the periodic system. The final state function can thus be written as a linear combination of atomic $1s$, $2s$ and $2p$ states:

$$|f\rangle = g|1s\rangle + a|2s\rangle + b|2p_x\rangle + c|2p_y\rangle + d|2p_z\rangle. \tag{2.15}$$

Here the coefficients g, a, b, c, d give the weight of the atomic orbitals in the LCAO expansion. The final state wavefunction in spherical coordinates is expressed as

$$|f\rangle = gR_{1s}(r) + aR_{1s}(r) + R_{2p}(r)(b\sin\vartheta\cos\varphi + c\sin\vartheta\sin\varphi + d\cos\vartheta), \tag{2.16}$$

where $R_{1s}(r)$,$R_{2s}(r)$ and $R_{2p}(r)$ represent the radial part of wavefunctions. The position vector $\mathbf{r}$ in the dipole operator in the same coordinate representation, $\mathbf{r} = r(\widehat{e}_x\sin\vartheta\cos\varphi + \widehat{e}_y\sin\vartheta\sin\varphi + \widehat{e}_y\cos\vartheta)$, where $\widehat{e}_x$, $\widehat{e}_y$ and $\widehat{e}_z$ are the unit vectors along axes of the coordinate system. The matrix element is get by integration:

$$\langle f|\boldsymbol{\mu}|i\rangle = \langle f|e\mathbf{r}|i\rangle = R\frac{4\pi}{3}(b\widehat{e}_x + c\widehat{e}_y + d\widehat{e}_y), \tag{2.17}$$

where $R = \int R_{1s}(r)R_{2p}(r)r^3dr$ is the radial part of the matrix element. Therefore, according to Eq. 2.17, for K-shell excitation the vector matrix element points in the same direction as the $p-$component in the final state orbital on the excited atom. Thus, for a $1s$ initial state the final state must have a p orbital component for an allowed transition, as dictated by the dipole selection rule.

For final state we now consider the σ^* and π^* orbitals of two double bonded atoms Figure 2.2. We orient the coordinate system so that the σ^* orbital and therefore the internuclear axis lies along the $z-$axis, and the π^* orbital lies along the $x-$axis. (In case of triple bonding the other π^* orbital would point along $y-$axis). The orientation of the X-ray polarization unit vector ϵ is specified by spherical angles θ and ϕ. The polarization dependence of resonance intensity associated with the σ^* molecular orbital final state is then given by

$$I_{if}(\sigma^*) \propto |\boldsymbol{\epsilon} \cdot \widehat{e}_z|^2 \propto \cos\theta^2. \tag{2.18}$$

The σ^* resonance is greatest for ϵ along the internuclear axis and vanishes when ϵ is perpendicular to it. The polarization dependence of the resonance associated with the π^* orbital is correspondigly

$$I_{if}(\pi^*) \propto |\boldsymbol{\epsilon} \cdot \widehat{e}_x|^2 \propto \sin\theta^2 \cos\phi^2 \propto \sin\theta^2. \tag{2.19}$$

The π^* resonance has the opposite angular dependence from σ^*. Equations 2.18 and 2.19 explain the origin of the linear dichroism in NEXAFS angular spectra. These resonances are therefore very useful in defining the bond and as a consequence molecular orientation in space.

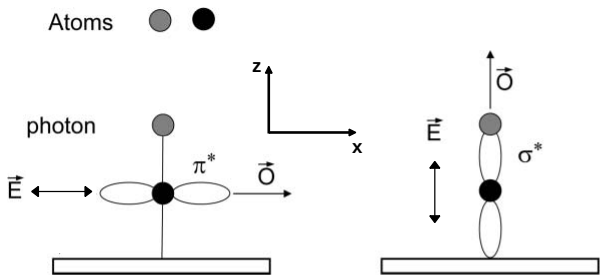

Figure 2.2: Schematic representation of the origin of the angular dependence of NEXAFS resonances for a π-bonded diatomic molecule adsorbed with its molecular axis normal to the surface. As a result of the different overlap between the electric field vector, **E**, and the direction of the final state orbitals, **O**, the π^*-resonance is maximized at normal incidence (left), while the σ^*-resonance is maximized at grazing incidence (right).

2.1.4 Classification of molecules

For the discussion of the angular dependence of $K-$shell resonances it is convenient to classify molecules into general group, based on the strong directionality of MOs. Such directionality is even present in chemisorbed molecules altough the overall symmetry of the adsorbate complex will in general be different from that of the free molecule. As discussed in the previous section, since K-shell excitations reveal the amplitude and the directionality of MOs on the excited atom, it is therefore possible in many cases to expoit local symmetry notions based on the direction of maximum orbital amplitude on the excited atom relative to the nuclear framework.

The spatial distribution of π^* and σ^* orbitals can be inferred by considering the bonding in unsaturated diatomics and rings. Depending on the number and mutual orientation of either s or p orbitals, the MO "sum" can either point in a specific direction, being of *vector* type, or it spans a plane, being of *plane* type. The schematic illustrations of most common orbital configurations are displayed in Figure 2.3, where single orbitals are represented by vectors, whereas a plane is defined whenever two or more vectors have higher than twofols rotational symmetry about an axis.

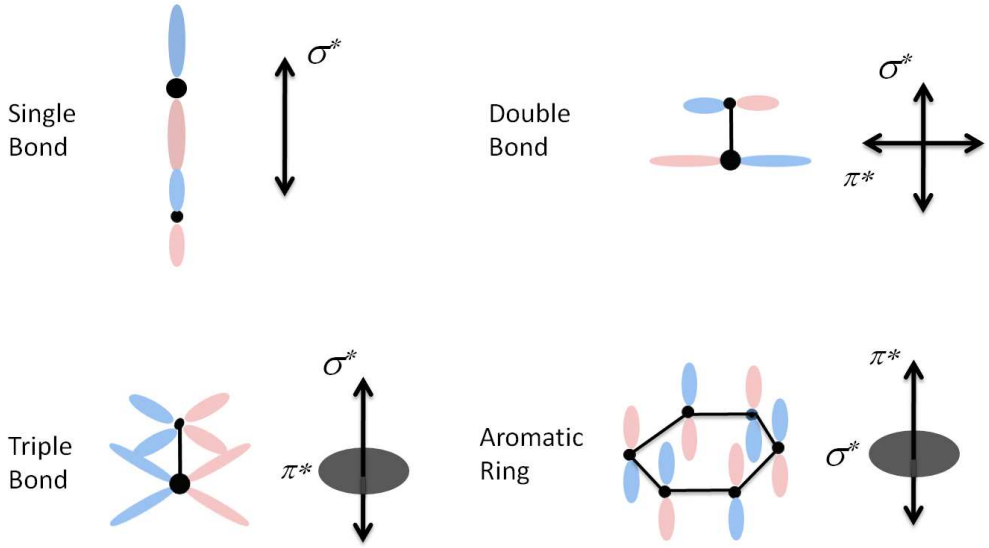

Figure 2.3: Sketches of spatial orientation of π^* and σ^* in four important groups of molecules. Molecules are divided into classes depending on whether the π^* or σ^* orbitals point in a specific direction (vector type) or span a plane (plane type).

In the present thesis, the case of an aromatic ring such as benezene (C_6H_6) or pyrrole (C_4H_5N) is of particular interest because are the basic costituents

of molecular complexes such as porphyrin, melanin and indene. In this case the atoms are arranged in a plane and thus the σ^* system is characterized by this plane. The π^* orbitals can be represented by vectors perpendicular to the plane. Thus, the further analysis of angular dependence of the resonant intensity will be developed for the π^* *vector* and σ^* plane.

2.1.5 Absorption lines for linearly polarized X-rays

The π^* and σ^* resonances of interest here can be described in a molecular orbital picture as a dipole transition from s initial state and the p component of π^* and σ^* final states. The intensity of the resonanant absorption lines I is given by the oscillator strength f, according to Eq. 2.13. In considering the angular dependence of specific resonanant absorption lines we can assume that the resonance shapes will be constant and only their peak height will change. Therefore the change in absorption intensity I will be proportional to the change in oscillator strength (as well as the change in X-ray absorption cross section) and by the use of Eq. 2.8 and 2.13 we can write

$$I \propto |\langle f|\mathbf{e}\cdot\mathbf{p}|i\rangle|^2 \propto \frac{1}{|E|^2}|\langle f|\mathbf{e}\cdot\mathbf{p}|i\rangle|^2. \tag{2.20}$$

where $\mathbf{e}$ is a unit vector in the direction of the electric field vector $\mathbf{E}$, $\mathbf{p}$ is the momentum operator, $|i\rangle$ is the $1s$ initial state and $|f\rangle$ the molecular orbital final state of transition.

For elliptically polarized synchrotron radiation from a bending magnet source the electrical field vector $\mathbf{E}$ has two phase-related orthogonal components of different magnitude [113]. The larger component lies in the horizontal orbit plane of the storage ring and the smaller component is vertical. Let us orient our coordinate system such that the X-rays propagate down the z-axis and the $x-$ and $y-$ axes with unit vector $e^{\parallel}$ and $e^{\perp}$ lie in the horizontal and vertical planes, respectively. The electric field is described by

$$\mathbf{E} = \mathbf{E}^{\parallel}\cos(kz-\omega t) + \mathbf{E}^{\perp}\cos(kz-\omega t). \tag{2.21}$$

$\mathbf{E}^{\parallel} = |\mathbf{E}^{\parallel}|e^{\parallel}$ and $\mathbf{E}^{\perp} = |\mathbf{E}^{\perp}|e^{\perp}$ are the maximum components of the electrical field in and perpendicular to the orbit plane of the storage ring.

In the present thesis NEXAFS measurements were performed at SuperESCA, BACH and ALOISA beamline at Elettra synchrotron radiation source. The undulators that provide synchrotron radiation to these beamlines produce linearly polarized X-rays, with the electrical field parallel to storage ring orbit plane, therefore in the following the perpendicular compo-

nent $\mathbf{E}^{\perp}$ will be neglected. Thus, the polarization factor P, defined as

$$P = \frac{|\mathbf{E}^{\parallel}|^2}{|\mathbf{E}^{\parallel}|^2 + |\mathbf{E}^{\perp}|^2} \tag{2.22}$$

is assumed to be $P = 1$[1]. The resonance intensity is now given by

$$I \propto |\langle f|\mathbf{e}^{\parallel} \cdot \mathbf{p}|i\rangle|^2. \tag{2.23}$$

For determining the molecular orientation relative to the substrate, it is convenient to fix the coordinate system to the surface rather than to the molecule, as shown in Figure 2.4 for the vector type (left) and plane type (right) of orbital. As derived in section 2.2 and according to the notation in

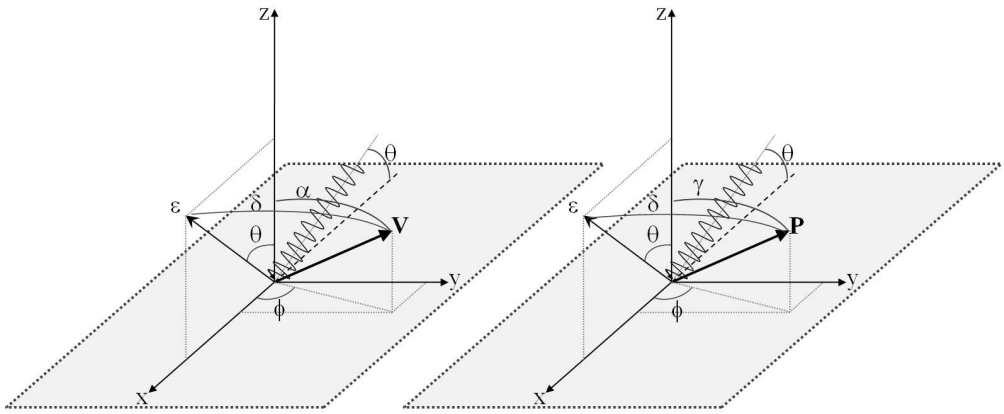

Figure 2.4: Coordinate system with the corresponding geometry of *vector* (left) and *plane* σ^* or π^* orbital on the surface.

Figure 2.4, the angular dependence of the π^* vector orbital changes as

$$I_v \propto \cos^2 \delta, \tag{2.24}$$

where δ is the angle between the X-ray polarization vector and the vector orbital. In the coordinate system of the surface, this is expressed as

$$I_v \propto (\cos\theta \cos\alpha + \sin\theta \sin\alpha \cos\phi)^2. \tag{2.25}$$

The angular dependence of molecules with σ^* plane is derived by integrating 2.24 over all azimuthal angles ϕ in a plane with normal $\mathbf{N}$, yielding

$$I_p \propto \cos^2 \epsilon, \tag{2.26}$$

[1] Actually the polarization factor is about 0.95 but in our experimental data analysis it is included in the error bars

where ϵ is the angle between the electric field **E** and the normal of the plane **N**. In the cooedinate system of the surface, one gets

$$I_p \propto 1 - (\cos\theta\cos\gamma + \sin\theta\sin\gamma\cos\phi)^2. \tag{2.27}$$

The angular dependence of the resonance intensities given by Eq. 2.25 and 2.27 explicitly depends on the azimuthal orientation of the molecule relative to the substrate through the angle ϕ. In case of surface symmetry, molecular orientational domains will form and the NEXAFS signal averages over all present configurations. This can be applied to the Eq. 2.25 and 2.27 by averaging with respect to the azimuthal angle according to the surface symmetry. In presence of twofold symmetry, the cross-term 2.25 containing $\cos\phi$ vanishes upon averaging over two adsorption geometries, and the equation for the vector orbital simplifies into

$$I_v \propto (\cos^2\theta\cos^2\alpha + \sin^2\theta\sin^2\alpha\cos^2\phi). \tag{2.28}$$

Similarly, the Eq. 2.27 for plane orbital simplifies into

$$I_p \propto 1 - \cos^2\theta\cos^2\gamma - \sin^2\theta\sin^2\gamma\cos^2\phi. \tag{2.29}$$

When the substrate possesses threefold or higher symmetry, no preferential orientation of the molecules is assumed and the absorption signal averages over all azimuthal angles ϕ. This leads to the result

$$\begin{aligned} I_v &\propto \cos^2\theta\cos^2\alpha + \frac{1}{2}\sin^2\theta\sin^2\alpha \\ &\propto \cos^2\theta\left(1 - \frac{3}{2}\sin^2\alpha\right) + \frac{1}{2}\sin^2\alpha \end{aligned} \tag{2.30}$$

for vector orbital, and, by averaging over ϕ

$$\begin{aligned} I_p &\propto 1 - \cos^2\theta\cos^2\gamma - \frac{1}{2}\sin^2\theta\sin^2\gamma, \\ &\propto \frac{1}{2}\left[\cos^2\theta\left(1 - 3\cos^2\gamma\right) + 1 + \cos^2\gamma\right] \end{aligned} \tag{2.31}$$

Therefore for a threefold or higher symmetry the azimuthal angle dependence vanishes and the expression are equivalent to those for cylindrical symmetry about the surface normal. As a consequence, for one specific molecular orientation the resonance intensities may become independent of the X-ray incidence angle θ. If in Eq. 2.30 and 2.31 α or γ are equal to the *magic angle* of 54.7° the angle-dependent terms vanishes. In this case, the intensity distribution measured in NEXAFS is indistinguishable from that for a completely random molecular orientation. In addition, for an X-ray incidence angle of $\theta = 54.7°$ the measured intensities are indipendent of the molecular orientation.

2.2 Resonant Photoemission Spectroscopy

2.2.1 Introduction

The request for device miniaturization necessitates a deep understanding of the processes occurring at the organic-inorganic and organic-organic interfaces [114]. Concerning chemical dynamics, charge transfer (CT) is a very important basic aspect, determining the elementary interaction processes of electronically excited states [115]. Charge transfer dynamics occurring in the femtosecond and sub-femtosecond regime has recently been successfully investigated by Resonant Photoemission Spectroscopy (RPES or ResPES). This experimental technique is based on core-level excitation and decay, with an intrinsic time scale based on the lifetime of core-holes, and is considered as an alternative route to the "pump and probe" laser based techniques [56, 116]. Indeed, it differs in two primary characteristics from the more traditional pump-probe studies:

1. The measurement is carried out not in the time domain, but instead in the energy domain, so that a shorter time scale compared to tens of fs can be explored

2. core electrons are involved, giving the advantage of atomic specificity unique to core spectroscopies.

In this section, the fundamentals of the RPES technique are briefly presented, with particular references to the review articles of Brühwiler *et al.* [56] and Vilmercati *et al.* [116].

2.2.2 Basics of the resonant photoemission process

In the RPES experiment the valence band (VB) X-ray photoemission is measured as the photon energy is tuned across the specific atomic absorption edge. Below the absorption edge, only the direct photoemission from the occupied electronic states contributes to the VB photoemission spectra, whereas at the X-ray absorption edge the spectra display contributions also from the resonant autoionization emission.

In fact, upon changing the photon energy across the resonance, the core electron is excited to different empty orbitals of the system and the changes in the absorption coefficient reflect the unoccupied electronic structure of the sample that are meausered in NEXAFS spectrum. Once the core electron is promoted to an unoccupied state by the absorption of light, the system is left in an unstable, excited state that may decay via radiative or non-radiative

(Auger) decay. In the case of K-edges of low Z materials, the overwhelming majority of decays takes place electronically in an Auger-like fashion (for C 99.7% and for N 99.5% of the excited states decay electronically [117]).

Figure 2.5 (right panel) depicts a schematic of the different electronic excitation and de-excitation channels of interest here, that follow[2] the resonant excitation. In the left part of Figure 2.5 the non-resonant excitation and de-excitation channels are shown for comparison. At specific resonant photon energies, a core-hole is created upon X-ray absorption leaving the system charge neutral until deexcitation (Figure 2.5-d). The radiationless decay of the excited system may then proceed via two different autoionization channels; in the "participator decay", the promoted electron is involved in the decay process and the system is left in a final state with a single valence vacancy (Figure 2.5-e), whereas in the "spectator decay" the promoted electron remains in the normally unocuppied state and the Auger emission also leaves the system in a +1 charge final state, but with two valence holes plus an excited electron (Figure 2.5-f).

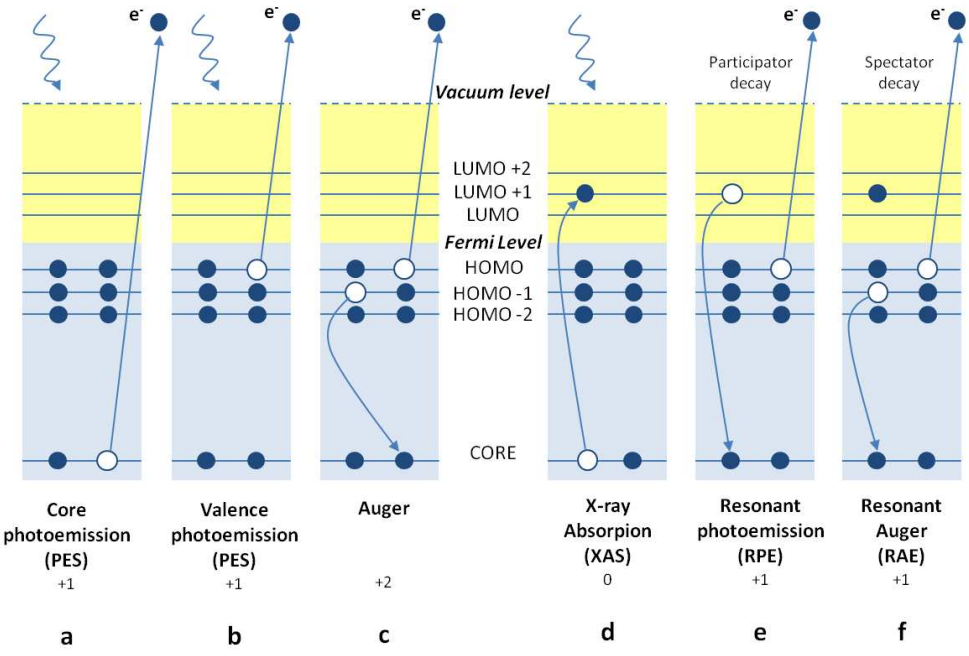

Figure 2.5: Scheme of the excitation and decay processes in the core electron spectroscopies.

The electronic final state in the participator autoionization decay is equal

[2]In using the concept "follow", we ignore here coherence in the excitation-deexcitation process, a topic that will be trated later.

to that in direct valence photoemission (Figure 2.5-b). The study of participator decay channels is therefore usually referred to as resonant photoemission (RPE).
In a molecular solid, the participator decay of a resonant core-hole excited-state solid is a major contribution to resonant spectra as long as intramolecular core-hole screening is dominant, and as long as the excited electron is localized on the molecule probed [56]. Such RPE events are easily identified as sharp features with strongly varying intensities as a function of the photon energy. In fact the intensity of the valence photoemission (that occurs at any photon energy), due to the competing x-ray absorption processes, is relatively small in the vicinity of the core-hole excitation energy, and does not usually exceed the intensity of the spectrum below threshold [118].
Besides, the RPE feature are more easily detected in the low binding energy region, since the final state of the spectator decay has a higher energy with respect that of the participator decay (it corresponds to a shake-up state in PES).

Most importantly, inasmuch as for different elements or chemically shifted atoms core excitations are site-specific [47], RPE may supply information on the local electronic structure [119]. While photon is tuned across the absorption resonance, the various valence band peaks may be assigned to the different chemical elements that constitue the material and also in certain favorable conditions to inequivalent sites of the same chemical element in the molecule, if the energy resolution provided by the experimental apparatus is sufficient. An example of the interface state clear identification is given by the PTCDA/Au(110) study [116].

The final state of the spectator autoionization channel clearly resembles that of the normal Auger decay (Figure 2.5-c), apart from the localisation of the excited electron in an unoccupied orbital. For this reason, the spectator decay is also known as resonant Auger emission (RAE).
In large molecules (i.e. in many-atom system), the spectral shapes of resonant and normal Auger are quite similar, which could be expected based on the small perturbation to the system played by a single valence electron. On the other hand, the improved core-hole screening due to the Coulomb interaction between the excited electron and the core-hole plays a role in moving the RAE features at higher kinetic energy with respect to their normal Auger counterparts. This is the so-called "spectator shift". While for free atoms the spectator shift is huge (dozen of eV), for adsorbates on metal substrates and for compounds with a good internal screening such as the π-systems used here, however, the spectator shift is generally small (less than 3 eV), which makes the identification rather difficult [56]. Additionally, since the orbital spatial distribution is found to spread through the molecule for

higher unoccupied molecular orbitals with respect to the LUMO orbital, the amount of the shift is expected to decrease as the core electron is promoted to LUMO+1, LUMO+2 etc., because the excited electron can easier delocalize far from the core-hole site.

2.2.3 Effect of charge transfer

Selectivity of individual orbitals can be combined with measurements of charge transfer (CT) times in the femtosecond regime using resonant core-level excitation and decay [56, 120]. May and Kühn choose a working definition of charge transfer in terms of a spontaneous charge redistribution due to a molecule-molecule or molecule-substrate coupling at interfaces. In practice, the reservoir (substrate or molecule) coupling can lead to a transfer of the excited electron away from the excitation site on the timescale of the core-hole decay, as depicted in the panel a of Figure 2.6.

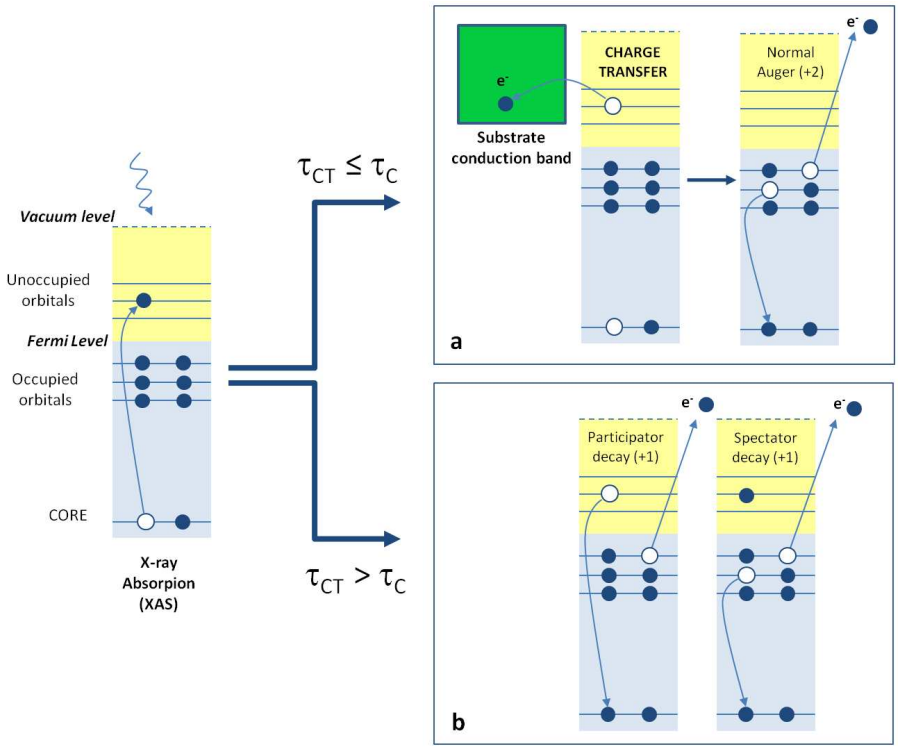

Figure 2.6: Schematic of the two main pathways for de-excitation of a system that is coupled to a (substrate) continuum. If the electron transfer is competitive with or faster than the core-hole decay, the excited electron may tunnel into the continuum, opening a normal Auger channel (panel a). Alternatively, if the delocalization of the excited electron is slower than the core-hole decay, autoionization occurs as usual (panel b).

In the case of complete electron delocalisation the decay adjusts to the normal Auger emission, while a fractional delocalisation leads to the occurrence of both resonant and normal components in the spectra. Thus, if one is able to distinguish the resonant and the normal spectral components, one can in principle study charge transfer events on the timescale of the core-hole lifetime τ_C. Note that the decay times for the various core holes are quite well known ($\tau_{C1s} = 6$ fs, $\tau_{N1s} = 5$ fs and $\tau_{O1s} = 4$ fs [121]) but can vary much with surroundings. For example, the electron transfer from an aromatic adsorbate to a TiO_2 semiconductor surface can occur in less than 3 fs [120].

The charge transfer time τ_{CT} is related to the observed intensities [56] as

$$\frac{\tau_{CT}}{\tau_C} = \frac{I_{resonant}}{I_{Auger}} \tag{2.32}$$

Even if some practical recipes for the identification of the RPE and RAE parts of the spectrum are available (see section 2.2.4), the distinction of resonant and nonresonant parts of the spectrum might not be straightforward. Then a first method can be chosen, in which the RAE part of the spectrum is disregarded, while the easily identifiable part of the RPES is used for the determination of charge-transfer times. According to this procedure, the RPE intensity I_{RPE}^{coup} of the coupled system is related to the corresponding RPE intensity I_{RPE}^{iso} of the isolated system. The charge transfer time is then given by

$$\tau_{CT} = \tau_C \left[\frac{\frac{I_{RPE}^{coup}}{I_{XAS}^{coup}}}{\frac{I_{RPE}^{iso}}{I_{XAS}^{iso}} - \frac{I_{RPE}^{coup}}{I_{XAS}^{coup}}} \right] \tag{2.33}$$

Here, the resonance intensity normalization to the absorption NEXAFS allows for distinguishing the lack of resonance enhancement on the VB due to the presence of fast CT from that due to the lack of spatial correlation of the involved wavefunctions. The method here proposed demands, however, that data are available for the isolated system. This is indeed the case when data are obtained from the same organic film in the thick multilayer phase where no charge transfer is supposed to occur if the molecules are very weakly bound. In this case, I_{RPE}^{iso} corresponds to the RPE intensity of the multilayer film and I_{RPE}^{coup} is represented by the RPE intensity of the monolayer film adsorbed on a substrate.

Another approach builds on the use of the coupling system (e.g. monolayer) data only and relies on the use of RAE insted of RPE to determine τ_{CT}. In fact, the total resonant intensity I_{res} is $I_{res} = I_{RES} + I_{RAE}$, but $I_{RES} \ll I_{RAE}$, and hence it is sufficient to treat the RAE part of the spectrum. Since the charge transfer is coupled to the resonant intensity, and the core-hole

lifetime to the normal Auger one, $\tau_{CT}/\tau_C = I_{resonant}/I_{Auger} \approx I_{RAE}/I_{Auger}$. That means, if one can distinguish between the spectral intensities coupled to the resonant Auger and the normal Auger processes, respectively, the charge transfer time τ_{CT} can be determined directly from the knowledge of the core-hole lifetime τ_C. Such a distinction is possible by virtue of the spectator shift (cf. section 2.2.2) that shifts the resonant Auger to higher kinetic energies than the normal Auger intensity. On the contrary, the spectral shapes of resonant and normal Auger are expected to be quite similar, which allows to approximate the shape of the former by that of the latter.

2.2.4 Energy dispersion of the resonant features

The energy dependence of the emitted electrons with the incoming photon energy is a crucial point for inspecting the coherence of the excitation-de-excitation processes.

In principle, the autoionization process is Raman-like, i.e. is properly described as a one-step process in which the resonant excitation and the subsequent decay of core-electron excitations are seen as one, nonseparable, scattering event [122, 123]. As a consequence, the energy conservation applies only between the initial ground state and the final decay state, whereas for the intermediate (core-excited) state, energy conservation needs not to be fulfilled. The resulting kinetic energy of both the participator and the spectator decay hence scales with the photon energy.

This is easily understood for the participator channel, as the final state of the RPE is identical to that of the direct valence photoemission channel (Figure 2.5-b and e). In general terms, one can imagine that, as the photon energy is detuned slightly off the resonant transition, the core-electron is still excited to the resonant orbital, yet the excess energy is conserved in the whole system. As soon as the excited state decays, this excess energy is carried away by the emitted electron, therefore the kinetic energy of the emitted electron is proportional to the exciting photon energy. In this case, the excitation and deexcitation steps in the process are considered truly coherent.

The exciting photon bandwidth compared to the lifetime width of the resonant core-to-bound excitation is a critical paramenter for observing the energy coherence of the excitation-de-excitation process.
Let's assume for simplicity an intermediate state in which a single eigenstate dominates, due, for example, to a large cross section or to a large energy separation to the next available states. If the excitation is induced by an X-ray photon of narrowly defined energy, i.e. a photon which has an energy spread comparable to or less than the core-level lifetime broadening, a state of well-defined energy is created "within" the resonance. Energy conservation

in this case demands, for an isolated system such as a free atom or molecule, that the resonant channels (both the participator and the spectator) disperse linearly with the photon energy in this excitation interval, as pointed at the beginning of this section. This means that the system fulfills the so-called Auger resonant Raman condition.

The situation is efficaciously sketched in Figure 2.7. The net excitation profile is the product of the beamline output (assumed to be Gaussian in profile) times the inherent line shape (assumed to be Lorentzian). Narrow-band excitation (solid line) defines a narrow input energy range, and thus an equally narrow band of output energy for each final state via energy conservation. For broad-band excitation (dashed line in Figure 2.7) the behaviour is different: resonant channels have an input energy uncertainty given by the the intrinsic line profile (seen by comparing the net excitation profiles to the inherent line shape in Figure 2.7) which determines to a great extent the effective excitation and, again via energy conservation, the deexcitation profile. Consequently, RAE and RPE features are distinguished in the spectra by their dispersion behaviour: RPE features are found at constant binding energy, whereas RAE features stay at constant kinetic energy in line with the behaviour of the normal Auger process. The ResPES spectra presented in this thesis have been collected using a photon bandwidth of $\Delta E \leq 100$ meV, i.e. the photon bandwidth is much narrower than the lifetime-broadened linewidth of the absorption peak. Thus, unlike the normal Auger spectral structures, the Raman Auger features may be observed to disperse linearly with the photon energy.

The coherence of the excitation-de-excitation process is destroyed whenever a fast charge transfer of the excited electron occurs. When a small system is in direct contact with a reservoir (large system, e.g. a substrate), the excited electron can delocalize to the substrate's empty states by tunneling. If this delocalization is slower than the core-hole decay, then the system does not know anything about this possibility, and the characteristics of the Auger-Raman conditions are expected to result (Figure 2.6, panel b). If, however, the electron transfer is competitive with or faster than the core-hole decay, the breakdown of the Auger-Raman characteristics results and a new decay channel is activated. This is called "normal Auger emission" because its equality to the Auger spectra obtained by primary excitation into the ionization continuum, i.e. the system is left in a +2 charge state and the corresponding spectral de-excitation features stay at constant kinetic energy, independent of the exciting photon energy (Figure 2.6, panel a). The excitation and deexcitation steps are hence treated as consecutive, independent, incoherent events (i.e. a two-step process), requiring energy conservation even for the intermediate state.

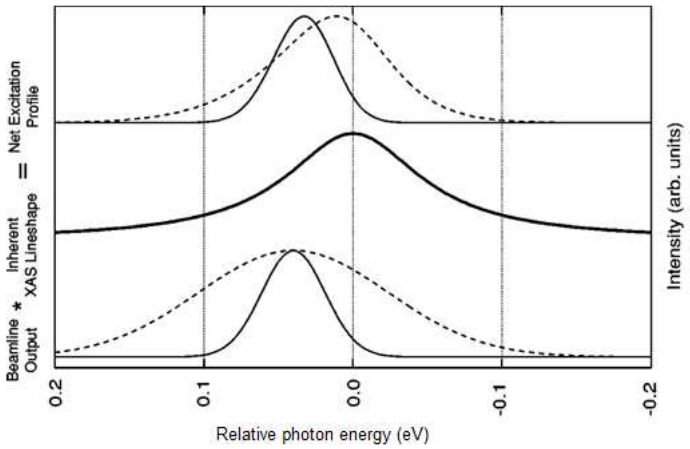

Figure 2.7: The Auger resonant Raman (ARR) effect. The net profile is the product of the beamline output by the inherent line as indicated. If the electron measured in deexcitation is the only channel for energy release from the core excited system, narrow-band excitation defines a narrow input energy range, and thus an equally narrow band of output energy for each final state via energy conservation. Otherwise, for a broad-band excitation, the intrinsic line profile determines to a great extent the effective excitation and, again via energy conservation, the deexcitation profile.

In contrast to the Raman-like conditions, if the photon energy is detuned slightly off the resonant transition, the excess energy (but also phase and, of coures, charge) is transported into the continuum of the substrate, and the resulting kinetic energy of the Auger-CT emitted electron is constant. Therefore, the different dispersion characteristics of the spectral features, depending on whether the excited electron is localised or not during the core-hole lifetime, can be conveniently used to distinguish them and to identify their relative share in the deexcitation spectrum, which, as discussed in section 2.2.3, allows the determination of charge transfer times.

Chapter 3

Growth of ZnTPP monolayers on Ag(110) and Si(111)

3.1 Introduction

In the context of an emerging technology based on thin film devices, organic/inorganic interfaces continue to play an important role, as they often constitute the bottleneck to the injection and transport of charge carriers [39]. At the same time, the flexibility afforded by organic molecular films in terms of modes and conditions of deposition, chemical modification of materials, molecular mixing and doping are opening a number of routes for modifying and improving interfaces in ways which cannot be applied to inorganic materials [40]. The role of surface/interface science, in taking advantage of this flexibility, will be very important. In this perspective, porphyrins are one of the most studied systems of organic molecules because of their facility to absorb light, the ability to interact with gases and the involvement in many biological systems. These molecules have therefore the potential to be involved in solar cells, optoelectronics, gas sensors and data storage device fabrication [38, 124].

In this chapter, the preparation of a conformationally controlled Zn-tetraphenylporphyrin (ZnTPP) monolayer (ML) on two possible substrates, Ag(110) and Si(111), is reported. Silver, normally used as contact in photovoltaic or transistor devices, and silicon, worldwide employed in the semiconductor industry, have been chosen as substrates. The choice of the zinc as central metal has been motivated by the electronic configuration of this metal ($3d^{10}4s^2$). In fact, since the d-shell is filled, d orbitals are not expected to be involved in the orbital hybridization of the whole molecule and, eventually, in the interaction with substrate due to the molecule adsorption.

Consequently, photoemission data may be straightforwardly compared to the isolated molecule and/or to free-base molecule data.

The results of a preliminary investigation of the $3d$-metal insertion effects on the free-base porphyrin valence band spectrum are shown in Figure 3.1. In the bottom part of Figure 3.1, 2H-TPP and ZnTPP valence band spectra are displayed. Apart from the peak at about BE = 10 eV for ZnTPP VB, the two spectra are very similar, with a slight difference in the spectral weight of the band around 7-9 eV in ionization potential energy. The case of $3d$-metal octaethylporphyrins (OEP) brings further evidences (Figure 3.1), because data for CoOEP and NiOEP are also available: again the valence band spectra 2H-TPP and ZnOEP are quite similar, whereas the insertion of Co and Ni in the OEP macrocycle drammatically affects the eletronic structure. In particular, the valence band of NiOEP and CoOEP become very complex in the energy region between 6-9 eV, i.e. close to the HOMO level energy position. A strong modification in the valence band structure is further expected when NiOEP and CoOEP are adsorbed on inorganic surfaces as shown for CoOEP/Ag(110) [125]. Therefore, ZnTPP consitutes a starting point for inspecting the specific characteristics of porphyrin/inorganic interface.

The molecular orientation with respect to the substrate was monitored using angular dependent near edge X-ray absorption fine-structure spectroscopy (NEXAFS), while the electronic properties of the filled states were investigated using X-ray and ultraviolet photoemission (XPS and UPS). Finally, the charge transfer properties and the interaction with the substrates were studied using resonant photoemission (ResPES) at the C K-edge. In particular, the coupling of the phenyl legs with the substrate and the relative excited charge injection is dramatically different for the two considered surfaces, demonstrating that the specific functions, such as photoinduced electron transfer, transport and changes in the electronic properties, derived from the interaction with the specific substrate. As a preliminary investigation, the molecular level structure before the contact will be analysed by considering data in gas phase. Moreover, the interaction molecule-molecule will be taken into account by comparing the present results with those reported in Ref. [26, 30] of the multilayer case.

3.1.1 Zinc-tetraphenyl-porphyrin

In the ZnTPP molecule, a Zn atom is coordinated in the center of the porphine ring, leading to the removal of the two hydrogens that in the free-base porphyrin (2H-TPP) are bonded to the pyrrole nitrogen atoms. For a comparison of the porphine cycle of 2H-TPP and ZnTPP, see Figure 1.1 and Figure 3.2.

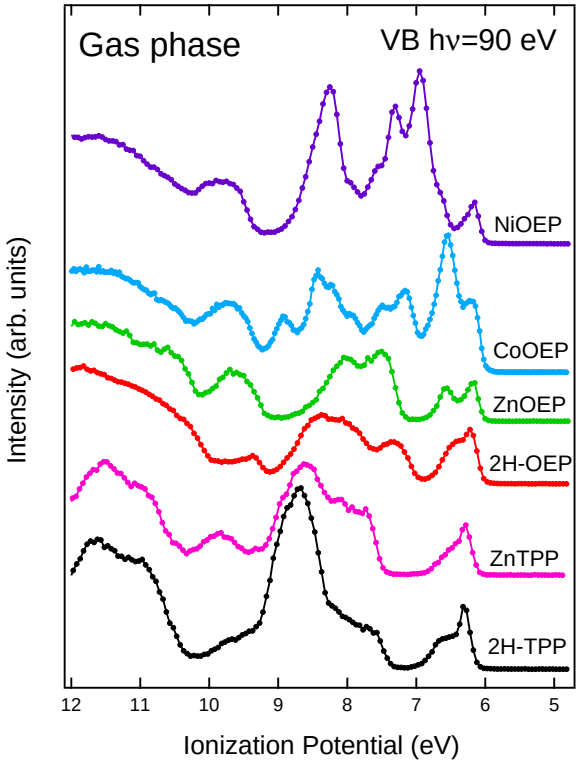

Figure 3.1: Valence band spectra of some OEP and TPP molecules in gas phase collected at hν = 90 eV.

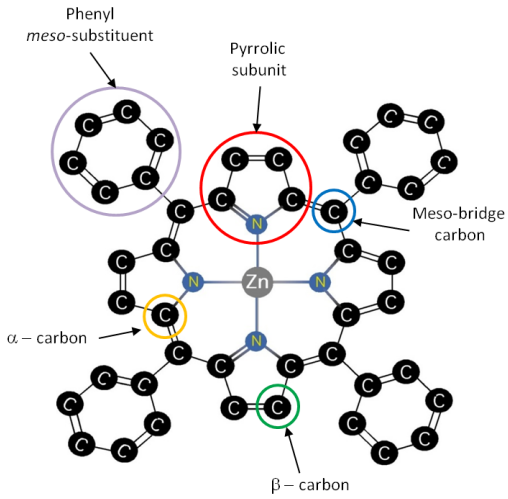

Figure 3.2: Zinc-tetraphenyl-porphyrin (ZnTPP).

Since the macrocycle is flat, the porphine of ZnTPP has a D_{4h} symmetry [126]. This symmetry in the gas-phase is confirmed also by the N 1s photoemission spectrum (hν = 500 eV), showing a single peak with a full-width at half-maximum of 0.7 eV, which indicates that the four N atoms are equivalent. This is at variance with the N 1s core level spectra of 2H-TPP where two components separated by about 2 eV are observed: the one at higher binding energy (BE) is assigned to the two pyrrolic N atoms (-NH-) while the lower BE peak corresponds to the two iminic ones (-N=) [127] (see Figure 1.1).

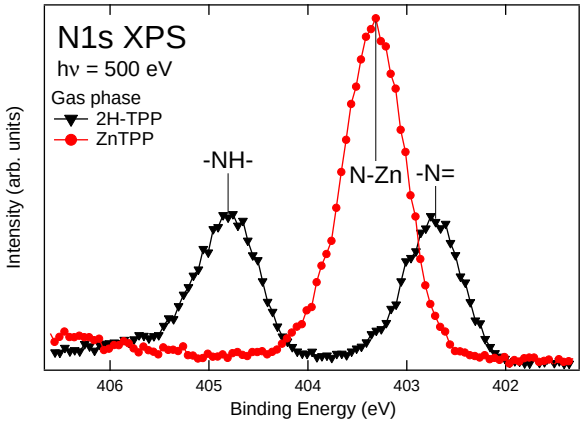

Figure 3.3: N 1s photoemission spectra of 2H-TPP and ZnTPP in gas phase. Spectra are normalized so that they have the same total peak area.

Synthetic ZnTPP porphyrins have phenyls as meso-aryl substituents. In the case of the isolated molecule, the large phenyl-porphyrin dihedral angles, which result from steric interactions with the β-hydrogens, leads to a minimal π-overlap between the phenyl ring and the porphyrin, thus causing only a slight perturbation to the electronic structure [128]. The distribution of phenyl-porphyrin dihedral angles for some β-unsubstituted porphyrins is shown in Figure 3.4 [129]. It can be noted that the isolated zinc(II), copper(II), nickel(II) and free-base porphyrin molecules have similar distributions of dihedral angles (the mean angle is 73° with a standard deviation of 9°). Meso-Phenylene-linked porphyrins do not exhibit significant conjugation because of this non-planarity [130].

The presence of the phenyl groups, therefore, cause only a very weak perturbation of the macrocycle states, and the electronic structure is expected as a rough superposition of the macrocycle and phenyl groups electronic states. This has been shown both in the isolated molecule and in the multilayer film. Here, the case of 20 ML of ZnTPP/Si(111) is reported [26]. In Figure 3.5 the NEXAFS spectrum at the C 1s threshold of ZnTPP multilayer is displayed

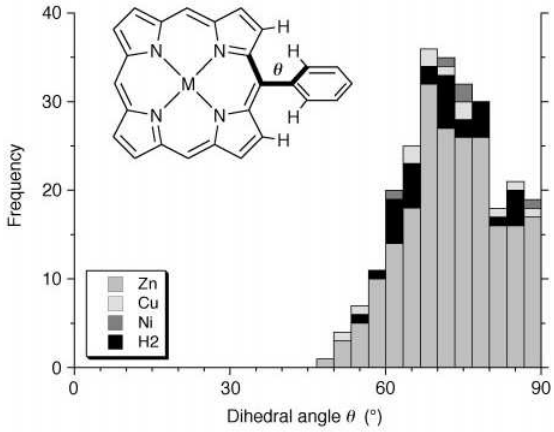

Figure 3.4: Distribution of dihedral angles in isolated meso-phenyl Zn(II), Cu(II), Ni(II) and freebase porphyrin molecules, from the Cambridge Crystallographic Database (CCD) [129].

with the corresponding NEXAFS spectra of benzene [131] (dashed line) and Zn-octaethylporphyrin [131] (with dominant contribution from the macrocycle, dotted line). The ZnTPP spectrum seems to be a simple superposition of the other two, supporting that there is almost no interaction between the π^* states of the macrocycle and those of the phenyl groups. Besides, according to this analysis, the first absorption peak at $h\nu = 284.3$ eV is mainly associated to the absorption transitions from core electron states located on carbon atoms in the macrocycle to the macrocycle π^* states, while the strong peak at $h\nu = 285.3$ eV can be primarly assigned to the transitions occurring from core electron states located on carbon atoms in phenyls to phenyls π^* orbitals.

Note that the NEXAFS spectra measured at the C 1s edge show a notable dependence from the incidence angle of the light (inset of Figure 3.5). Specifically, when NEXAFS spectrum is collected at grazing incidence (20° from the surface plane), the intensity of the first macrocycle peak is clearly reduced, indicating that the molecular macrocycles in the film are oriented, maybe azimuthally disordered, but with a defined angle with respect to the surface plane. A careful analysis of the angular dependence of the N 1s NEXAFS spectra reveals that the ZnTPP macrocycle forms an angle of $5\pm5°$ with the sample surface (not shown). On the other hand, in the C 1s NEXAFS spectrum (inset of Figure 3.5), the phenyl peak doesn't show any dichroism, indicating that the phenyl gropus may be randomly oriented with respect to molecule plane.

In multilayer films, the weak Van der Waals intermolecular interaction

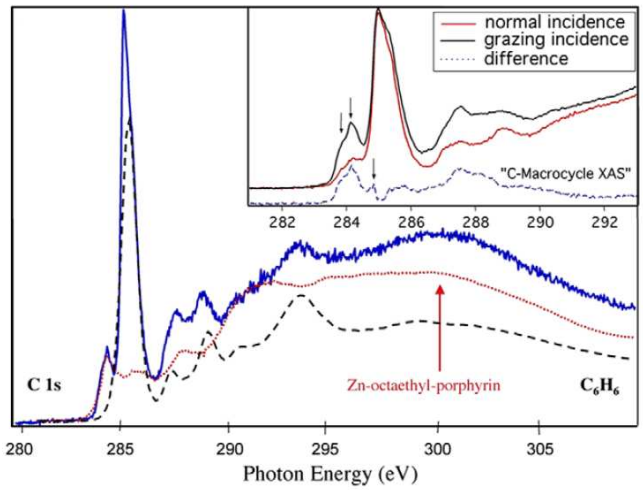

Figure 3.5: NEXAFS spectra at the C 1*s* threshold of ZnTPP (solid line), benzene (dashed line) and Zn-octaethyl-porphyrin (dotted line). The spectrum is measured with the linear polarization of the light at 20° from the surface normal. Inset: Near-edge region of the ZnTPP NEXAFS spectra collected at normal incidence and at grazing incidence (20° from the surface plane) of the linearly polarized light. The difference spectrum is also shown (dashed line) [26].

prevails. This may be induced by comparing the valence band spectrum of isolated molecules in the gas phase (i.e. without interaction with any other object - a surface or a neighbouring molecule) to the valence band spectrum in multilayer (Figure 3.5). In fact, the analysis of the valence band spectra is a reliable tool for inspecting the degree of intermolecular interactions because the electrons in the valence band play the fondumental role in chemical bonds. The energy position of the gas-phase spectrum, measured as a function of the Ionization Potential, has been shifted of −3.75 eV for allowing a direct comparison of ZnTPP occupied molecular states. Despite spectral features are more structured in the gas phase measurements, as expected, the multilayer spectrum shows strong similarities with the spectrum of the molecule in gas phase, suggesting that only a weak electrostatic interaction occurs between molecules, i.e. Van der Waals forces.

3.2 Experimental Section

The data were collected at the ALOISA and SuperESCA beam lines at the Elettra synchrotron facility in Trieste. All the experiments were performed in ultra-high-vacuum experimental chambers at a base pressure of 10^{-10} mbar. Highly purified (>99.9 %) commercial ZnTPP was used and sublimated di-

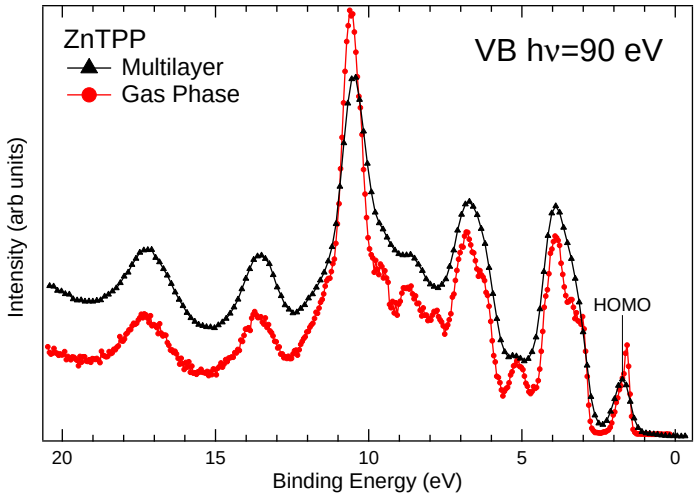

Figure 3.6: Valence band spectrum of ZnTPP in multilayer films (dots) and in gas phase (triangles). Highest occupied molecular orbital (HOMO) level in multilayer is indicated (BE = 1.8 eV).

rectly on Ag(110) and Si(111)-7×7 by a homemade, resistively heated, Ta evaporator. The Ag(110) surface was prepared by Ar^+ sputtering at 500 eV and annealing at 700 K, while the Si(111)-7×7 surface was prepared by removing the natural oxide by annealing at ≈ 1200 K. In both cases the absence of contaminants and ordering of the surfaces were checked by means of XPS and low energy electron diffraction techniques. To obtain ZnTPP monolayer (ML), and in general all the porphyrin monolayers reported in this thesis, a thick film of ZnTPP molecules was deposited in UHV with a home-built Knudsen cell evaporator via sublimation technique on the substrate held at RT. Then, the ZnTPP monolayers (ML) were obtained by sublimating the thick film at ≈ 550 K. We therefore define 1 ML of ZnTPP as the maximum amount of molecules adsorbed on the substrate surface following the above procedure.

The XPS data for 1ML ZnTPP on Ag(110) were collected by means of a hemispherical electron energy analyzer characterized by 100 meV resolution and ±1° angular resolution, while the XPS data for the ZnTPP monolayer on the silicon surface were recorded collecting the photoelectrons from a double-pass hemispherical analyzer characterized by an angular resolution of ±1° and an energy resolution of 80 meV. NEXAFS spectra were measured at the C 1*s* and N 1*s* thresholds in partial yield mode (ALOISA) or in the Auger yield mode (SuperESCA). The binding energy of the photoemission spectra was calibrated using the Fermi level of Ag(110) (set at a binding energy of 0 eV), which implies a binding energy of the Ag 3*d* at 368.10 eV

for the conducting substrate, and the Si $2p_{3/2}$ peak (BE = 99.36 eV) for the semiconductor substrate.

3.3 Results and discussion

3.3.1 NEXAFS study

The fine determination of the conformation and arrangement of adsorbed molecules on a surface are the key points to analyse, since they are strongly related to the physical and chemical properties of the final organic/inorganic interfaces. This information can be obtained using the linearly polarized NEXAFS spectroscopy.

Figure 3.7-a,b show the NEXAFS spectra at the N 1s and C 1s thresholds for the ZnTPP/Si(111) substrate as functions of the angle θ between the linear light polarization and the surface normal (α and ϕ, respectively, as indicated in Figure 2.4). Figure 3.7-c,d show the same spectra for the Ag(110) substrate. The spectra were normalized to the total photon flux intensity and, according to the procedure indicated in Ref. [47], they were normalized to the σ^* state at high photon energy after a pre-edge baseline subtraction. Instead, the N 1s spectra of ZnTPP/Ag(110) consists of raw data.

In general, the π^* states that characterize organic aromatic molecules are due to atomic-like p_z states perpendicular to the plane containing the aromatic frame. This is the case for porphyrins; the π^* states generated by the four central nitrogen atoms, are well separated in energy from the remaining empty orbitals. They are therefore easy to study and give a clear indication of the orientation of the molecular skeleton with respect to the hosting surface [47]. These states are responsible for the two peaks visible in the N 1s NEXAFS spectra below 404 eV, which correspond to the dipole transition from the N 1s core level to the π_1^* (e_g symmetry) and π_2^* (two almost degenerate transitions with b_{2u} and e_g symmetries) empty levels [31, 132]. The case of ZnTPP adsorbed over Ag(110) is straightforward; the molecular macrocycle lies perfectly parallel to the substrate surface. This is evident even by the raw data that show zero intensity for the π^* states below 404 eV as the electrical field of the incoming synchrotron radiation become coplanar with the Ag surface (pure s polarization), as observed in Figure 3.7-c.

A different arrangement is found when the ZnTPP monolayer is grown on Si(111). According to the model described by Stöhr [47] the area ratio $\pi_1^*(\theta)/\pi_1^*(0°)$ as a function of the angle θ depends parametrically on the tilt and the azimuthal angles between the molecular plane and the surface. Because of the three-fold degenerate symmetry of the Si(111) substrate, this

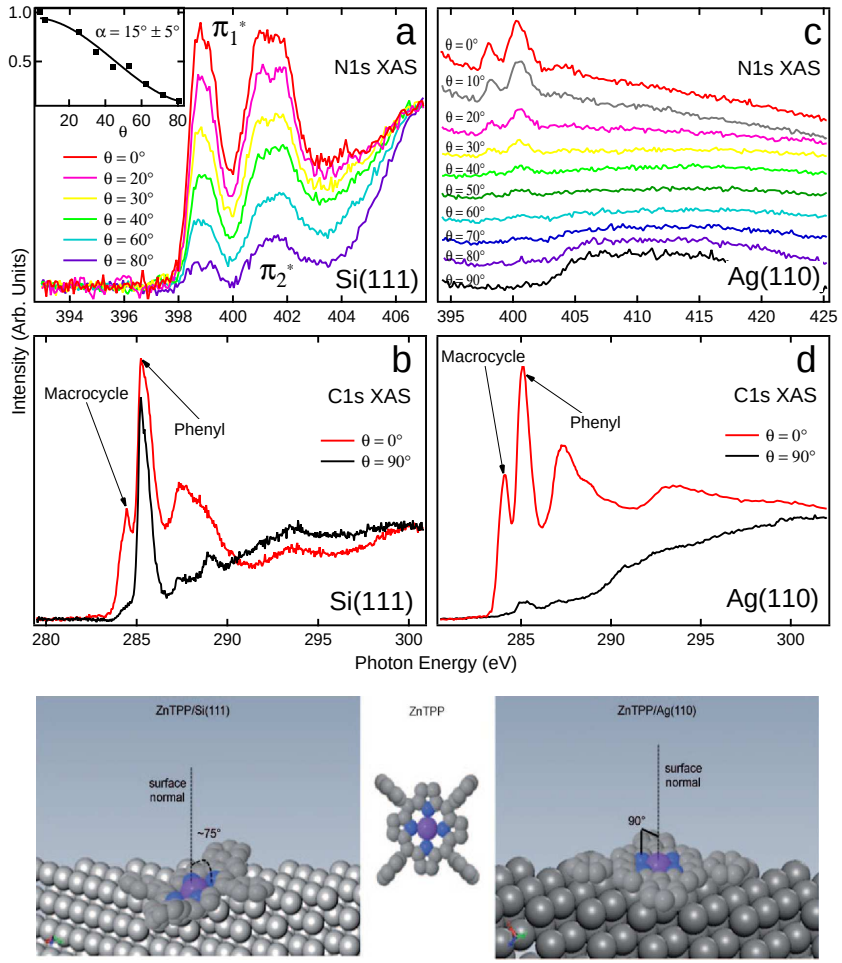

Figure 3.7: The NEXAFS monolayer spectra for the N 1*s* and C 1*s* thresholds of ZnTPP on Si(111) (a,b) and Ag(110) (c,d). a) Selection of the N 1*s* spectra on Si(111). The inset shows the area ratio $\pi_1^*(\theta)/\pi_1^*(0°)$ as a function of the angle θ between the surface normal and the linear light polarization. The angle a between the macrocycle and the surface was obtained by fitting these data with the Stöhr equation for three or more domains (see equation 2.31). b) C 1*s* spectra on Si(111) at $\theta = 0°$ and $\theta = 90°$. c) Complete series of N 1*s* spectra on Ag(110), for which $\alpha = 0°$. d) C 1*s* spectra on Ag(110) at $\theta = 0°$ and $\theta = 90°$. In the C 1**s** spectra the label "macrocycle" on the first peak indicates the absorption transitions from core electron states located on carbon atoms in the macrocycle to the macrocycle π^* states, while the label "phenyl" on to the second strong peak primarly denotes to the transitions occurring from core electron states located on carbon atoms in phenyls to phenyls π^* orbitals. The bottom panel shows a cartoon of the molecular adsorption angle and phenyl orientations of ZnTPP on the Si(111) and Ag(110) surfaces as obtained by NEXAFS experiments.

function is independent on the azimuthal angle. For estimating the area of the peak π_1^*, I accomplished the deconvolution of the NEXAFS spectra by performing a nonlinear least-squares fitting on the experimental data, using gaussian functions, the so-called error functions ("erf") background with exponential decay and an additional linear background. Fits have been repeated by varying the parameters of the fit, e.g. the number of componets required to reproduce the shape of the peak π_1^*, but similar results have been obtained. By using the equation 2.31, the fit of the area of the peak π_1^* vs the polarization angle yields an average tilt angle $\alpha = 15 \pm 5^\circ$ between the vector π^* orbital and the surface normal (see inset of Figure 3.7-a). The error bar originates from the different results derived from each deconvolution performed on NEXAFS spectra. Since in porphyrins the π^* orbital of the macrocycle lie perpendicular to the molecular plane, the tilt angle $\alpha = 15 \pm 5^\circ$ corresponds also to the angle between the macrocycle plane and the surface plane.

In general, the monolayer molecular orientation with respect to the substrate critically depends on the relative strengths of molecule-substrate interaction versus molecule-molecule interaction. The geometrical adaptation due exclusively to the molecule-molecule interaction becomes evident in the multilayer case and it is depicted in Chapter 3.1.1. While we expect the molecule-molecule interactions to be almost the same in the two cases studied herein, the molecule-surface bonds are markedly different, suggesting that the latter interaction as well as the possible substrate reconstruction and termination play an important role in the adsorption geometry.

We can obtain further information on the molecular orientation by looking at the NEXAFS spectra at the C $1s$ threshold. The C $1s$ NEXAFS spectrum is more complicated than the N $1s$ spectrum, because there are more C atoms in the molecule. However, as in the multilayer case, the first π^* peak is related to the C in the macrocycle and the most intense peak is mainly related to the C in the phenyl rings, with a small contribution from the macrocycle. In both cases, the macrocycle peak almost perfectly follows the behaviour of the corresponding π^* structures in the N $1s$ NEXAFS spectrum, confirming that the estimate of the molecular orientation is correct. On the other hand, considering the phenyl peak, it is clear that this feature shows a very small dichroism on Si(111) (suggesting that the phenyl rings have a sort of "disorder"), while the dichroism of the phenyl peak on Ag(110) is huge and follows the macrocycle peak, that is, the phenyl meso-substituents are, like the macrocycle, flat on the surface.

The rotational degrees of freedom of the phenyl meso-substituents and the flexibility of the porphyrin macrocycle allow for a conformational adaptation of the molecule to its local environment [133, 134, 65, 59, 135, 136, 137].

The TPP molecules in gas phase have the phenyl groups almost orthogonal to the macrocycle plane and this position is maintained in solution [128]. On Ag(110) we observe a rotation of the phenyl rings to lie as flat as the macrocycle, obviously due to the adsorption on this substrate.

A direct proof of a similar deformation has been given by Moresco *et al.* [138, 133], who have reported that a metal surface can modify the form of a porphyrin molecule. In particular, they observed that the interaction with Cu(111) makes the phenyl legs of a 3,5-di-tert-butylphenyl porphyrin (TBPP) molecule rotate by 90°, flattening the molecule on the surface. A similar rotation of the meso-substituent rings was observed by Eichberger et al. for tetrapyridyl porphyrin on Cu(111) [134]. On the contrary, on Ag(100) [65] and Cu(100) [138, 133] the phenyl meso-substituents in TBPP are orthogonal to the macrocycle plane.

From comparison with the adsorption of polyaromatic hydrocarbons, one can argue that the conformational flattening of the phenyl legs occurs when the latter ones match the substrate lattice, so that the overlap of the π orbitals with the substrate electron cloud is further increased. In fact, polyacenes are known to adsorb flat on the fcc(110) surface of transition metals, and the azimuthal orientation of their long molecular axis is effectively driven by the matching of the molecular inner structure with the substrate lattice. For instance, pentacene on Cu(110) is oriented along the [110] direction because of the close register between the ring spacing and the periodicity of the close compact atomic rows [139, 140]. On the other hand, the larger lattice spacing of Au(110) and Ag(110) rather favors the orientation along the [001] direction for pentacene [141, 142] and anthracene [143].

Another interesting property observed in Moresco's work [138, 133] is that in Cu(111) the tunneling current flows mainly through the legs because the π orbitals of the porphyrin macrocycle are electronically decoupled from the metallic surface. This means that the interaction between the macrocycle and the metallic surface cannot be very strong, even in a case where the whole TBPP molecule lies flat on the surface.

3.3.2 ResPES study

One possibility to check the degree of interaction between the substrate and the molecular adlayer is the resonant photoemission spectroscopy (ResPES) [56, 116], as accurately described in Chapter 2.2.

Because of the complexity of the processes involved, this technique only gives an upper limit for the charge transfer dynamic timescale. In addition, it is impossible to distinguish whether the excited electron delocalizes to the substrate or to a neighboring atom belonging to the same molecule. In

order to unveil this dynamic, and to distinguish the molecule-molecule from the molecule-substrate delocalization, the ResPES spectra obtained at the interfaces must be compared to those obtained on a thick film, where only the weak electrostatic molecule-molecule interactions are at work [30].

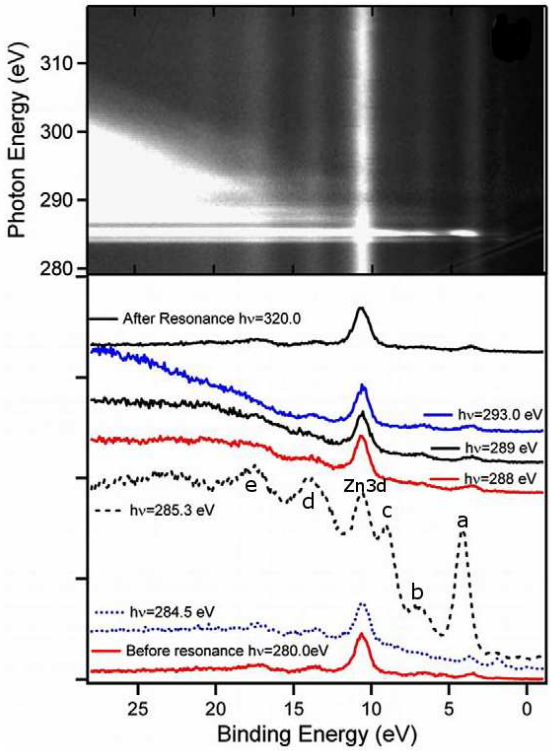

Figure 3.8: Two dimensional intensity plot of the ResPES valence band collected across the C 1*s* absorption threshold for the ZnTPP multilayer. The maximum intensity is in white. Spectra at significant photon energies are shown in the bottom panel. Figure adapted form Ref. [30].

Figure 3.8 shows the complete series of ResPES spectra of the ZnTPP multilayer obtained by scanning the photon energy from 279 eV to 320 eV across the C 1*s* absorption threshold with the light impinging on the sample at normal incidence [30]. The large bump appearing at high binding energy and dispersing with the photon energy is the Auger peak, while the small peak near E_F and dispersing in the opposite direction is the second-order peak. Since the photon energy is scanned across the core level threshold, the chemical selectivity of the NEXAFS spectrum applies to the ResPES spectroscopy and we can recognize whether the macrocycle or the phenyl groups are interacting with the substrate as well as the extent of localization of the various molecular orbitals. It is evident that several features resonate

as a function of the photon energy. In particular, when electrons are excited from C 1s core level to empty orbitals in the phenyls (hν = 285.3 eV), strong resonances (labelled from a to e in the bottom panel of Figure 3.8) appear. The comparison between NEXAFS profile and the integrated pure resonant contributions (i.e. obtained after subtracting an off-resonance spectrum and the Auger peak) has shown that [30] for excitation photon energies below hν = 285.5 eV the electron remains localized for a time bigger than the core-hole lifetime, which in the case of the C 1s of ZnTPP is about 5 fs [121].

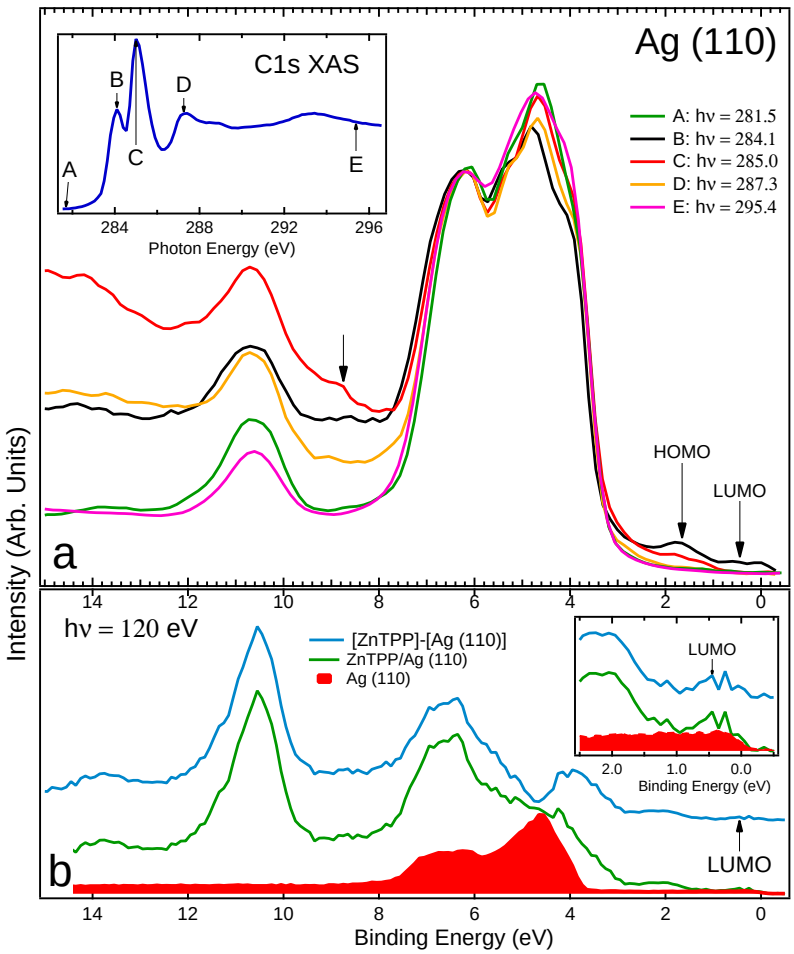

Figure 3.9: Valence band photoemission spectra of 1 ML of ZnTPP on Ag(110). a) Selected valence bands in the C 1s resonant region at the photon energy as indicated in the inset. The resonant features are indicated by arrows. b) Valence band measured at 120 eV together with the clean Ag spectrum. In the inset, the near Fermi level features are shown.

The resonant beahaviour of ZnTPP changes drammatically when a mono-

layer is interacting with Ag(110) surface. Figure 3.9 shows some selected resonant spectra at the C 1s threshold, that is, the valence band were collected with a photon energy that can also excite a C 1s electron to an empty state above the Fermi level. The spectra were taken with the light polarization perpendicular to the substrate surface or p-polarization at $\theta = 0°$ (we remark that in s-polarization conditions, with the electric field parallel to the surface, there are no available π^* states, therefore no excitation-de-excitation processes can be observed). Valence band spectra are dominated by the heavy contribution of the Ag structure, mainly found between 4 and 8 eV of binding energies. In comparison to the ZnTPP multilayer, reliable quenching of the resonances is visible, indicating the strong coupling of the overlayer π orbitals with the substrate states. A small resonance is present for the states near the Fermi level and for a state at about 9 eV as the photon energy is scanned across the phenyl and macrocycle absorption peaks (indicated by arrows). The intensities of these resonance peaks are reduced, but comparable to the multilayer spectrum. Yet when photon is scanned across the phenyl absorption (spectrum **C** in panel a) of Figure 3.9) the huge feature observed in the multilayer spectrum at 3.8-3.6 eV (peak a in Figure 3.8) is completely lost. This observation indicates that the interaction between the ZnTPP and the Ag(110) metallic substrate, even in this situation where the molecule lies flat on the surface, affects the phenyl rings more than the macrocycle, as in the case of TBPP on Cu(111) [138, 133].

Next we focus on the states near the Fermi level that correspond to the highest occupied (HOMO) and the lowest unoccupied (LUMO) molecular orbitals of the pristine ZnTPP. Both the spectral features resonates at hν = 284.1 eV, i.e. at the first macrocycle absorption (spectrum **B** in panel a) of Figure 3.9). The LUMO, which is two-fold degenerate in this molecule [144], is partly filled by electrons transferred from the metal to the ZnTPP. This is confirmed by the valence band photoemission at hν = 120 eV (see Figure 3.9-b), where the molecular states are better resolved. The clean Ag spectrum is shown underneath the monolayer spectrum. Part of the intensity near the Fermi level comes from the s band of Ag, but it is evident that there is a further contribution related to the filled LUMO of the pristine ZnTPP (the states near the Fermi level are highlighted in the inset) centered at about 0.3-0.4 eV. It is hard to say if the filled LUMO may cross the Fermi level giving a metallic character to the overlayer, but some information may come from the analysis of core level photoemission data, as described in the following section.

In the case of Si, it is evident that when the photon energy is scanned across the C 1s absorption peaks several intense resonances are visible. In Figure 3.10, selected resonant valence bands, corresponding to the points

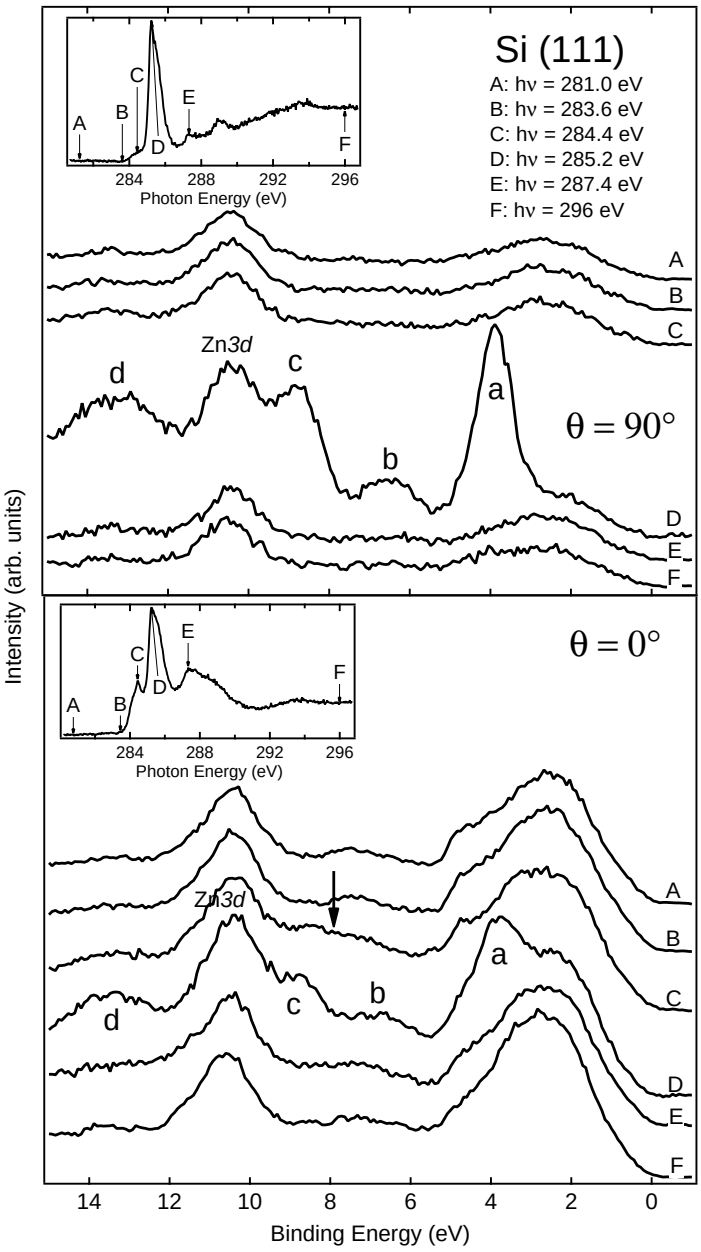

Figure 3.10: The valence band spectra of ZnTPP ML on Si(111) in the C 1*s* resonant region. Top: Selected valence bands with the linear polarization of the light in the surface plane. Bottom: Selected valence band spectra with the linear polarization of the light perpendicular to the surface plane. The insets show the corresponding C 1*s* NEXAFS spectra and the photon energies at which the valence band spectra were taken.

indicated in the insets of the NEXAFS spectra, are plotted. These resonant spectra are obtained by subtracting an integral background (Shirley) [145] and the possible Auger contribution from the photoemission spectra. Well below the resonance region at hν = 281.5 eV (A), the spectrum is mainly dominated by the silicon structures and the Zn 3d states (BE = 10.5 eV). Just below the resonance at hν = 283.6 eV (B) the spectrum appears quite similar to the previous one.

At hν = 284.4 eV (C), a C 1s electron is excited in the macrocycle. Beyond the Si(111) spectrum, that generally dominates the intensity and also depends on the polarization of the light, a weak resonance appears at a binding energy of 8-9 eV (indicated in Figure 3.10 by an arrow). This resonant decay is evident when the polarization is perpendicular to the surface plane ($\theta = 0°$), since the π^* macrocycle state is enhanced, while when the polarization is in the surface plane (c), this state is strongly quenched by polarization effects and no particular decay is observable in the valence band (see NEXAFS spectra in Figure 3.7).

At hν = 285.2 eV (D) the excited states located at the phenyl groups are populated. In this case, strong resonant decays are visible in the photoemission spectra (these are labelled form a to d in analogy with the resonant structure singled out in Figure 3.8), similar to the multilayer resonant behaviour [30]. This indicates that the phenyl group interactions with the Si(111) states are not very strong and the excited electron remains localized for a time comparable to or longer than the core-hole lifetime. For higher photon energies no evident resonant decays are detectable.

All in all, the ResPES spectra suggest that the interaction of the flat adsorbed ZnTPP on Ag(110) is important and involves the meso-substituent rather than the macrocycle, while on Si(111) the presence of an adsorption angle ($\theta = 15°$) and, in particular, the possible rotation of the phenyl rings in positions perpendicular to the macrocycle plane should reduce the interaction with the substrate, that is, the amount of charge transfer. In fact, the resonance on the phenyl rings is similar to the ZnTPP multilayer resonances. Finally, in the case of Ag(110) an electron transfer from the substrate bands to the ZnTPP orbitals is observed.

3.3.3 XPS study

Photoemission measurements further clarify the chemical states of these saturated monolayers of porphyrins. The C 1s spectra are shown in Figure 3.11. The monolayer spectra on Si(111) (d) and Ag(110) (c) substrates are compared with the ZnTPP multilayer (b) and gas-phase (a) spectra. All the spectra were collected with hν = 530 eV, except for the gas-phase spectrum

that was taken at the Gas-Phase beamline of Elettra (estimated resolution of 0.30 eV) by using hν = 382 eV, and was aligned to the multilayer spectrum. The gas-phase spectrum clearly shows a main peak, mainly ascribed to C 1s photoelectrons from the 24 phenyl atoms, and a low binding energy bump. To fit this spectrum, apart from the component due to the 24 phenyl atoms (peak 1), two additional components are considered stemming from the pyrrole carbons (8 atoms each, peaks 2 and 3) and another peak corresponding to the bridge atoms (4 carbon atoms, peak 4). We used a Shirley background [145] and the fit obtained with Doniach-Sunjic (DS) components [146] is superimposed on the spectrum (for more details, see Appendix A).

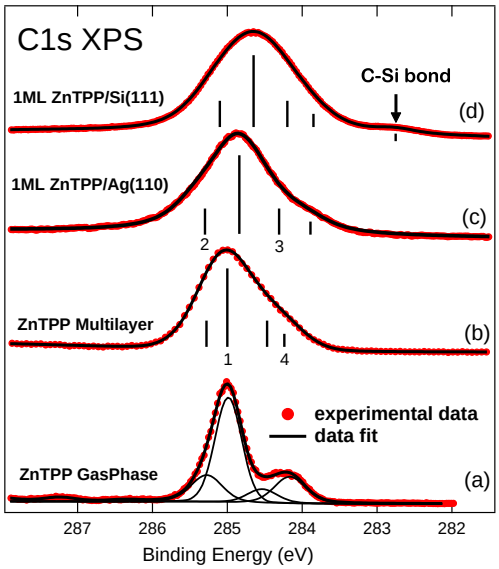

Figure 3.11: C 1s core level spectra and the corresponding fit. The components are only shown for the gas-phase spectrum (a), while for the other spectra, bars corresponding to positions and intensity of the components are shown. For Ag(110) (c) the fit was made using DS components with an asymmetry of 0.10±0.01. The numbers correspond to: 1-phenyl, 2-pyrrole, 3-pyrrole, 4-bridge peaks. The arrow indicates the core level feature due to the interaction with the Si(111) substrate.

The obtained fit corresponds well to the multilayer fit reported in Ref. [26] (shown in Figure 3.11) with the position of the related components indicated by bars) apart from the exchanged positions of the bridge (peak 4) and the low BE pyrrole (peak 3) components. This is probably due to solid-state effects and to different possible rotations of the phenyl legs, which mainly affect the bridge atoms. According to the arguments for the multilayer spectrum, we assigned the pyrrole component under the small peak to C-C atoms (peak 3), while the other component is assigned to C-N atoms in the

pyrrole rings (peak 2).

The C 1s spectrum of the monolayer on Si (d) is quite large and symmetric, which probably indicates that the D_{4h} symmetry of the molecule adsorbed on this substrate is lost and several C atoms contribute with slightly different energies. The C 1s spectrum of the monolayer on Ag (c), on the other hand, shows the asymmetric line shape on the low binding energy side similar to the multilayer and the gas-phase spectra.

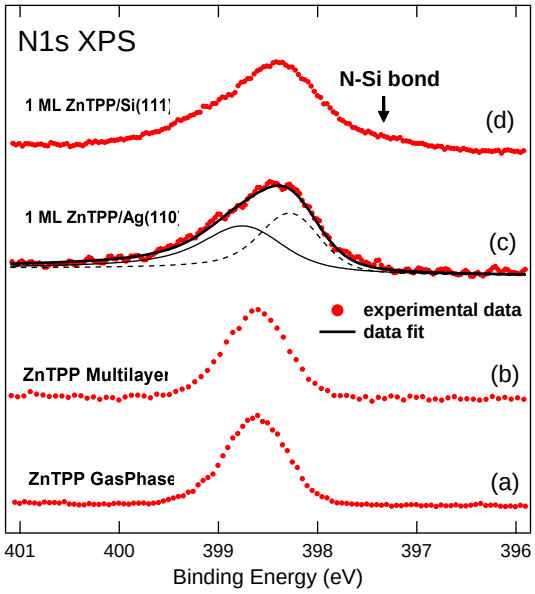

Figure 3.12: N 1s core level spectra. For the Ag(110) (c) the fit, by using two DS components with an asymmetry of 0.10±0.01, is shown. The arrow indicates the core level feature due to the interaction with the Si(111) substrate.

The monolayer data has been fitted adopting the same model used for the gas-phase spectrum although in these cases it is clear that this model may not be completely correct, in particular for the Si(111). Still, some important information can be extracted.

In general we expect the monolayer spectra to be shifted to lower binding energy compared to the multilayer one because of a better polarization screening of the core-hole due to the substrate. In the case of Si(111) the phenyl ring component (peak 1) is shifted to lower energy by 0.35 eV with respect to the multilayer. Although the shift is in the right direction, we cannot completely trust the obtained binding energy since the spectrum was aligned considering the Si $2p_{3/2}$ at 99.36 eV as for the clean substrate and, therefore, all the information related to band bending is lost. However, we note the presence of a small feature at lower binding energy, which is related

to the C-Si bonds [147]. The area of the C-Si peak corresponds to about 2 atoms compared to the total area.

On Ag(110) it is worth noting that the component due to the phenyl rings is at 284.85 eV (i.e. there is a shift to lower binding energies of 0.15 eV with respect to the multilayer), which is very similar to the binding energy of the C 1*s* spectrum of a flat benzene monolayer on Ag(110) [148]. This further indicates that the meso-substituents are flat and interacting with the Ag(110) substrate. An asymmetry parameter (singularity index) of 0.10±0.01 is required for the components to fit the C 1*s* spectrum of the monolayer on Ag(110), which implies that the overlayer is metallic or a semiconductor with a gap lower than our energy resolution (0.1 eV). Moreover, the pyrrole (peak 2) remains at the same position as in the multilayer, that is, it moves 0.45 eV with respect to the corresponding phenyl peak, while the pyrrole (peak 3) stays at the same relative position (i.e. it shifts with the phenyl peak). Also, the bridge peak moves away from the phenyl peak, indicating that the rotation of the phenyl rings influences this peak position and probably the flatness of the macrocycle.

A similar argument is found for the N 1*s* spectrum reported in the bottom panel of Figure 3.12. By fitting the N 1*s* spectrum of 1 monolayer of ZnTPP on Ag(110) (c) we have found two DS components with the asymmetry parameter 0.10±0.01 and the same area but with different widths. The fact that there are two components and not only one as in the case of the multilayer (b) and gas-phase (a) spectra indicates that the interaction with the substrate removes the D_{4h} symmetry of the molecule. The presence of two different widths suggests that two of the N atoms interact more with the substrate than the other two. This can be due to the rectangular substrate symmetry that faces Ag atoms (atop) and bonds (in between) to the N atoms or to a saddle distortion of the macrocycle. Finally, from the N 1*s* spectrum of ZnTPP/Si(111) (d), one feature related to the N-Si interaction is also detectable at lower binding energy (arrow). This actually indicates that the ZnTPP is interacting with the Si through one pyrrole ring and that the phenyl rings are rotated in such a way that they do not interact with the surface.

3.4 Conclusions

In conclusion, depending on the substrate, the adsorption orientation of ZnTPP is mainly mastered by the coupling of the phenyl legs or the macrocycle to the surface. For the Ag(110) substrate it is clear that the ZnTPP is adsorbed with both the phenyl rings and the macrocycle flat on the surface.

The interaction of the molecule with the substrate is stronger for the phenyl rings than for the macrocycle, as indicated by ResPES and core-level photoemission, and the macrocycle is probably distorted. The core level fit of both C 1*s* and N 1*s* requires the use of a DS lineshape with an asymmetry parameter (singularity index) of 0.10±0.01, which is consistent with a possible metallization of the molecular overlayer due to an electron transfer from the substrate.

A different arrangement and interaction are found for Si(111). The macrocycle plane of the molecules is adsorbed with an angle of $15 \pm 5°$. The ResPES behaviour indicates that for the phenyl rings the charge transfer into the substrate is less favorable than in the Ag(110) case and comparable to the multilayer case. Core-level photoemission indicates that the molecule is interacting with the substrate using a macrocycle pyrrole ring, while the phenyl rings are rotated in such a way that it minimizes the interaction with the substrate.

The information obtained indicates that the selected substrate and the interfacial behaviour are important for the controlled self-assembly of nanostructures having several degrees of freedom, such as porphyrins, and offers a number of powerful approaches to enhance the behaviour of porphyrin-based devices.

Chapter 4

2H-TPP/Ag(111)

4.1 Introduction

Free-base porphyrin monolayers on metals offer novel pathways to realize new compounds, because they form novel architectures and patterned surfaces where an ordered array of catalytic, magnetic, optoelectronic and sensing materials can be produced simply by evaporating in ultra-high-vacuum (UHV) the central metal atom. In fact, the macrocycle can host a wide range of metals at the center of the ring, forming metallo-porphyrins [22].

Herein the formation of a monolayer of free metal 2H-tetraphenyl porphyrins (2H-TPP) on Ag(111) is reported. The study of the geometry of the 2H-TPP monolayer and multilayer is of valuable importance in view of the *in-situ* iron metalation of 2H-TPP monolayers that will be related in Chapter 5. Here, it is shown that one of the most used ways to produce a 2H-TPP monolayer on Ag(111), as well as a monolayer of porphyrins on a substrate, e.g. the sublimation of a multilayer in the range 520-570 K [51, 68, 72, 149, 150], allows for a selected de-hydrogenation of both the macrocycle and the phenyl rings and the formation of a new molecule where the phenyl rings are connected to the macrocycle through two carbon bonds, making the complete molecule flat in a configuration similar to phthalocyanines.

4.2 Experimental and computational details

The data have been collected at the ALOISA beamline and in the μ-nanocarbon laboratory of the Elettra Synchrotron facility in Trieste. All the experiments were performed in ultra-high-vacuum (UHV) experimental chambers with a base pressure of 10^{-10} mbar. Highly purified commercial 2H-TPP molecules were sublimated on Ag(111) directly by a home made, resistively

heated, Ta evaporator at 570 K. The Ag(111) surface was prepared by Ar^+ sputtering at 1 keV and annealing at 770 K. The absence of contaminants and the ordering of the surfaces were checked by means of X-ray photoemission spectroscopy and Low Energy Electron Diffraction techniques, respectively. The 2H-TPP monolayer was obtained by sublimating a pre-deposited thick film of 2H-TPP molecules at 550 K. We therefore define a 2H-TPP monolayer as the maximum amount of molecules adsorbed on the substrate surface after the above procedure.

NEXAFS spectra were taken in partial electron yield mode by means of a channeltron facing the sample, while scanning the photon energy across the C and N K-edge with an energy resolution of 100 meV. The low energy secondary electrons have been filtered out by means of a negatively polarized grid (-230 V for the Carbon edge, -370 V for the Nitrogen edge) placed in front of the sample. The orientation of the surface with respect to the linear polarization of the synchrotron beam was changed by rotating the sample around the beam axis while keeping a constant grazing angle of 6 degrees. This scattering geometry allows changing the linear polarization of the light from s-polarization ($\theta = 90°$) to p-polarization ($\theta = 0°$) geometry without variation of the illuminated area on the sample. The raw data were normalized to the total photon flux by dividing the NEXAFS spectrum of the sample with the NEXAFS spectrum taken from the clean substrate in the same experimental conditions.

The XPS data for one monolayer of 2H-TPP on Ag(111) were collected by means of an hemispherical electron energy analyzer with a resolution of 100 meV. The photoemission spectra binding energy was calibrated using the Fermi level of Ag(111).

The STM experiments were carried out using an Omicron UHV RT AFM-STM with ApeResearch electronics. The bias voltage refers to the sample, and the images were recorded in constant current mode. Moderate filtering was applied for noise reduction. Chemically etched W tip was used as STM probe. The tip has been annealed at 700 K by electron bombardment in UHV, in order to remove the native oxide. The STM data were processed with the software Gwyddion [151].

Calculations have been performed within the collaboration with Stephan Blankenburg and Daniele Passerone from EMPA (Dübendorf, Switzerland). All calculations presented here were carried out with the CP2K suite using density functional theory in the mixed Gaussian plane wave scheme [152]. A TZV2P gaussians basis set was used for all atomic species. To model the exchange and correlation functional we used gradient corrections in the parameterization of Perdew-Burke-Ernzerhof (PBE) [153]. The electron-ion interaction was described by the norm conserving pseudopotentials of

Goedecker-Teter-Hutter (GTH) [154]. Van derWaals (vdW) interaction were included through the empirical scheme proposed by Grimme [155]. The single molecule adsorption (full monolayer adsorption) is modeled by periodically repeated slabs with a lateral size of 30.7 × 29.6 Å^2 (29.3 × 29.3 Å^2), containing four atomic Ag layers plus the adsorbed molecule(s). In addition, to understand the role played by TPP multilayer on the final geometry of the adsorbed molecules, we performed large scale simulations by means of a hybrid tight-binding density functional theory (DFTB) / empirical-potentials study as described in Ref. [156]. In this case, the substrate was modeled with ten atomic layers. On top of the Ag(111) slab we put up to 6 layers of TPP. For molecular dynamics (MD) simulations we used the NVT ensemble and temperature was controlled with a massive stochastic thermostat [157].

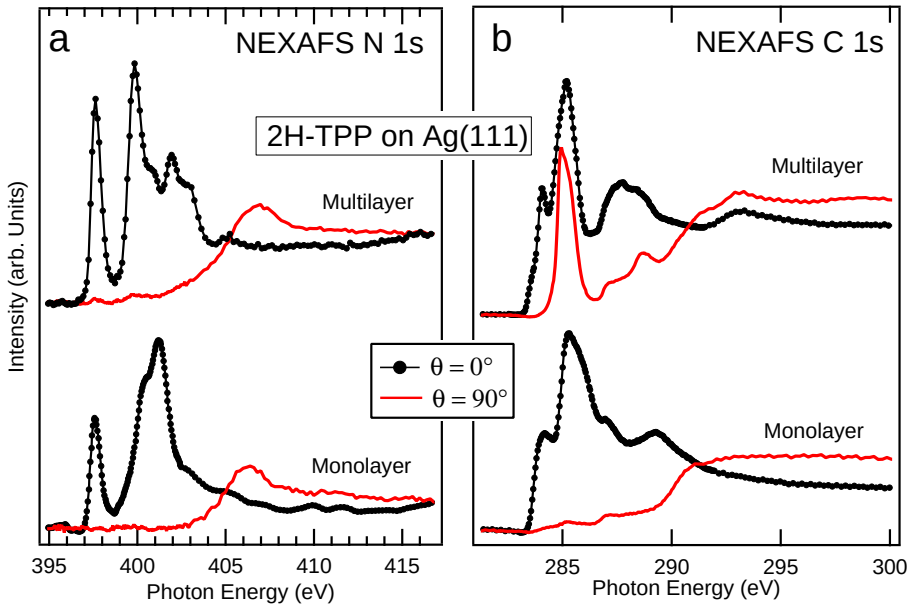

Figure 4.1: NEXAFS spectra at the N 1s (a) and C 1s (b) absorption thresholds for the 2H-TPP multilayer and monolayer on Ag(111). The monolayer was obtained by sublimating the multilayer at 550 K. The spectra were collected in two geometries: with the linear light polarization perpendicular ($\theta = 0°$) and parallel ($\theta = 90°$) to the substrate surface.

4.3 Results and discussion

Figure 4.1-a shows the Near-Edge X-ray Absorption Fine-Structure (NEXAFS) spectra at the N 1s threshold of the 2H-TPP multilayer and monolayer on Ag(111), while Figure 4.1-b shows the NEXAFS spectra at the C

1s threshold. The NEXAFS spectra are made by transitions from the corresponding N or C 1s core levels to the π^* and σ^* empty states of the molecule, (Figure 4.1). The NEXAFS spectra at two important angles are compared: $\theta = 0°$ (polarization perpendicular to the surface plane) and $\theta = 90°$ (polarization in the surface plane). The spectra where normalized at the total photon flux intensity and according to the procedure indicated in Ref. [47] normalized to the σ^* at high photon energy after a pre-edge baseline subtraction. In general, the π^* states that characterize planar organic aromatic molecules consist of a contribution that mainly belongs to a combination of atomic-like p_z orbitals that lie perpendicular to the plane containing the aromatic frame. This is the case of porphyrin: in particular, the π^* generated by the four central nitrogen atoms, are well separated in energy from the remaining empty orbitals, therefore they are easy to study and give a clear indication on the molecular empty states and on the orientation of the molecular skeleton with respect to the hosting surface [47].

Figure 4.1-a shows the N K-edge NEXAFS spectrum of the 2H-TPP in both multilayer and monolayer. The peaks at photon energies smaller than 404 eV are π^* resonances and for their assignment I refer to a former study by Polzonetti *et al.* [158]. It is clear that when $\theta = 0°$ the π^* features are enhanced while the σ^* resonances are completely suppressed, suggesting that the macrocycle, where the N atoms belong, is adsorbed parallel to the substrate surface.

Looking at the C K-edge NEXAFS spectra of Figure 4.1-b, we realize that there are two different behaviours for the multilayer and the monolayer. As it was indicated in in Chapter 3 the C 1s NEXAFS spectrum is practically the superposition of the macrocycle part and the benzene (phenyl) spectrum. The first two features in the peak at h$\nu \approx 284$ eV are assigned to the macrocycle, while the huge absorption structure at h$\nu \approx 285$ eV is mainly due to the phenyl groups π^* states. For the multilayer the macrocycle π^* peaks follow the same behaviour of the N K-edge NEXAFS spectra: when $\theta = 0°$ the π^* features are enhanced while when $\theta = 90°$ the π^* peaks are completely suppressed again suggesting that the macrocycle is adsorbed parallel to the substrate surface. The huge phenyl peak instead shows a very small dichroism suggesting that the phenyl rings either are randomly oriented or have an average aryl angle very close to the magic angle ($\theta = 54.7°$), in a sort of T-shape configuration with the macrocycle. This is not unexpected since in gas-phase and in solution the steric interactions between the hydrogen atoms tend to align the meso-substituents to an aryl angle in the range 50-90° with respect to the macrocycle [128]. In the multilayer the intermolecular forces are mainly Van der Waals, therefore the coupling among the constituent molecules is faint and the phenyl meso-substituents should

be oriented similar to the isolated molecules. This is evident when N K-edge and C K-edge NEXAFS spectra of the 2H-TPP multilayer are compared to the 2H-TPP gas-phase spectra: the multilayer spectra are very similar to the corresponding gas-phase spectra, indicating that the interaction between the molecules is weak (Figure 4.2).

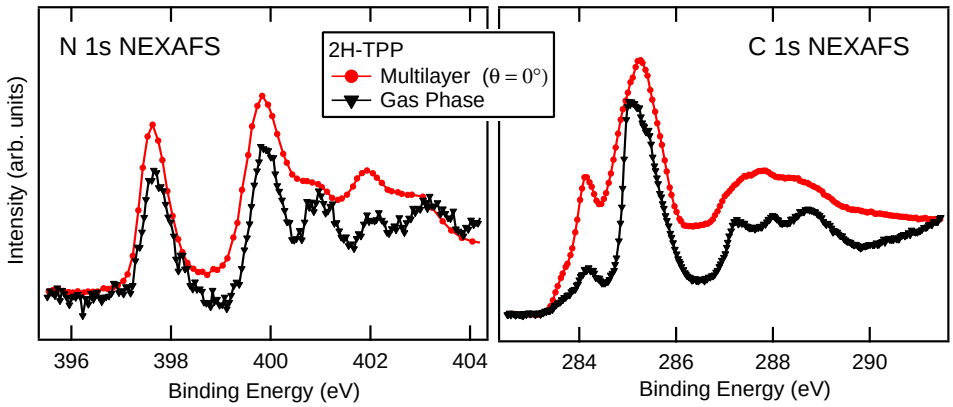

Figure 4.2: N K-edge (left panel) and C K-edge (right) NEXAFS spectra of 2H-TPP in gas phase (triangles) and in multilayer films deposited on Ag(111) (circles). Whereas gas-phase spectra have no dichroic behaviour, in the multilayer case, spectra collected at $\theta = 0°$ (polarization perpendicular to the surface plane) have π^* components of the macrocycle enhanced with respect to the π^* components of phenyls.

For the monolayer the situation is completely different. All the π^* peaks are suppressed when $\theta = 90°$, suggesting that in the present case also the phenyl rings are parallel to the surface. The rotation of the benzene moieties towards the surface has been observed for ZnTPP on Ag(110), as describe in Chapter 3, and for 3,5-di-tert-butylphenyl-porphyrin(TBPP) on Cu(111) [133, 134] and is typically related to the existence of an interaction between the s-p bands of Ag and the π orbitals of the adsorbate carbon atoms. However, on Ag(111) there are no similar reports and the 2H-TPP monolayer obtained in a similar way are expected to have the phenyl ring surfaces rotated with respect to the macrocycle [51, 66, 67, 68, 72, 149]. This observation is related to scanning tunneling microscopy (STM) and the relative density functional theory (DFT) simulation of the STM images: not a direct method.

In order to understand the NEXAFS results, which are instead based on a direct method [47], we also performed DFT, using the mixed Gaussian plane wave scheme, and molecular dynamics calculations on the monolayer and multilayer of 2H-TPP on Ag(111). To study the single molecular adsorption of 2H-TPP on Ag(111), several different geometries (e.g. phenyl rings flat,

perpendicular or rotated by 45°) were probed as a starting point for the structural optimization. The most stable configuration obtained corresponds to a tilted molecule as shown in Figure 4.3 (left panels), where the phenyl ring surfaces are rotated by around 33° at 0 K and 64.5° at 570 K with respect to the macrocycle. The adsorption energy of 2H-TPP in this configuration on Ag(111) at 0 K amounts to 2.8 eV, reflecting the strong interactions between 2H-TPP and the surface.

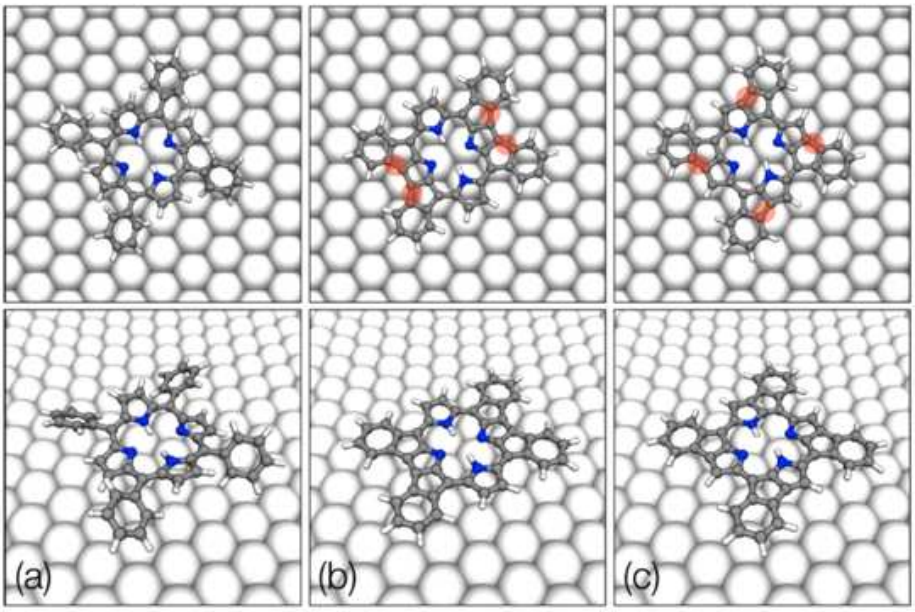

Figure 4.3: Scheme of 2H-TPP molecule where the phenyl ring planes are rotated by around 33° with respect to the macrocycle (a). This configuration is the most stable on Ag(111) according to DFT calculations. De-hydroganetes planar 2H-TPP molecules in case of rectangular (b) and spiral (c) structure. In the corresponding top panels, the new C-C bonds that form after de-hydrogenated are shaded in red.

Given this result, in order to explain the planarity revealed by the NEXAFS measurements, the only hypothesis that can be considered is a chemical and/or structural modification. Here, we want to propose two possible alternatives where de-hydrogenation processes produce planar molecules. Figure 4.3 (central and right panels) shows beside the original 2H-TPP molecule two de-hydrogenated structures with 8 hydrogen atoms less: a rectangular and a spiral one which are with 1.8 eV and 2.1 eV (per molecule) less stable than unmodified molecule, respectively. Despite these conformations are clearly energetically unfavored with respect to the original molecule, it has to be noted that if a de-hydrogenation reaction occurs (e.g. in the range

500-600 K), the hydrogen will desorb from the surface as 2H-TPP and new C-C bond occur; thus the process is irreversible.

To understand whether the presence of a multilayer could enhance or not a de-hydrogenation reaction, we performed molecular dynamics simulations. One and six molecular layers are used to access the influence of the multilayer on the local structure of first layer. Here, the tilting angle of the phenyl rings with respect to the macrocycle surface and the nearest C-C distance d_{C-C} between the phenyl rings and the macrocycle are averaged over the total simulation time of 9 ps at 630 K (a slightly higher T with respect to the experiment has been used to better sample the configurational space. This procedure is frequently used in MD simulations). Table 4.1 reflects the difference between the two cases: by using a multilayer, the titling angle and C-C distance of the first layer is decreased significantly compared to all other layers (2nd to 6th) and, in particular, to the monolayer situation. Additionally, in the case of monolayer the phenyl rings can also temporally flip, which is not happening in the multilayer at all. These circumstances can reduce the aryl-aryl coupling barrier with respect to the monolayer deposition.

layer	**1**	**2**	**3**	**4**	**5**	**6**
$d_{C-C}^{multilayer}$ [Å]	3.0	3.1	3.1	3.1	3.1	3.2
$d_{C-C}^{monolayer}$ [Å]	3.3					
$\alpha^{multilayer}$ [Å]	30.3	33.9	35.3	35.1	36.4	50.9
$\alpha_{C-C}^{monolayer}$ [Å]	62.4					

Table 4.1: Calculated nearest C-C distance d_{C-C} between the phenyl rings and the macrocycle and tilting angle of the phenyl rings with respect to the macrocycle surface for each of the layer of a multilayer (6 layer) and for a monolayer. These results are obtained by averaging over the total simulation time of 9 ps at 630 K.

Moreover it has to be noted that, due to the starting presence of a multilayer, formation of the rectangular molecules is unlikely to happen: while the chiral molecules preserve the 2D square lattice arrangement imposed by the multilayer, the rectangular ones would change the 2D square periodicity.

Finally, we note that possible substrate reconstruction and interactions mediated by surface with charge transfer from the substrate to the 2H-TPP, as revealed by photoemission in Chapter 5, must be explicitly taken into account, and gas-phase expectations based on intermolecular interactions and the static-surface approximation are not the solely forces working in this system. These new forces obviously tend to rotate the phenyl rings even more toward the substrate surface to increase the interaction between the s-p bands of Ag and the π orbitals of the adsorbate carbon atoms.

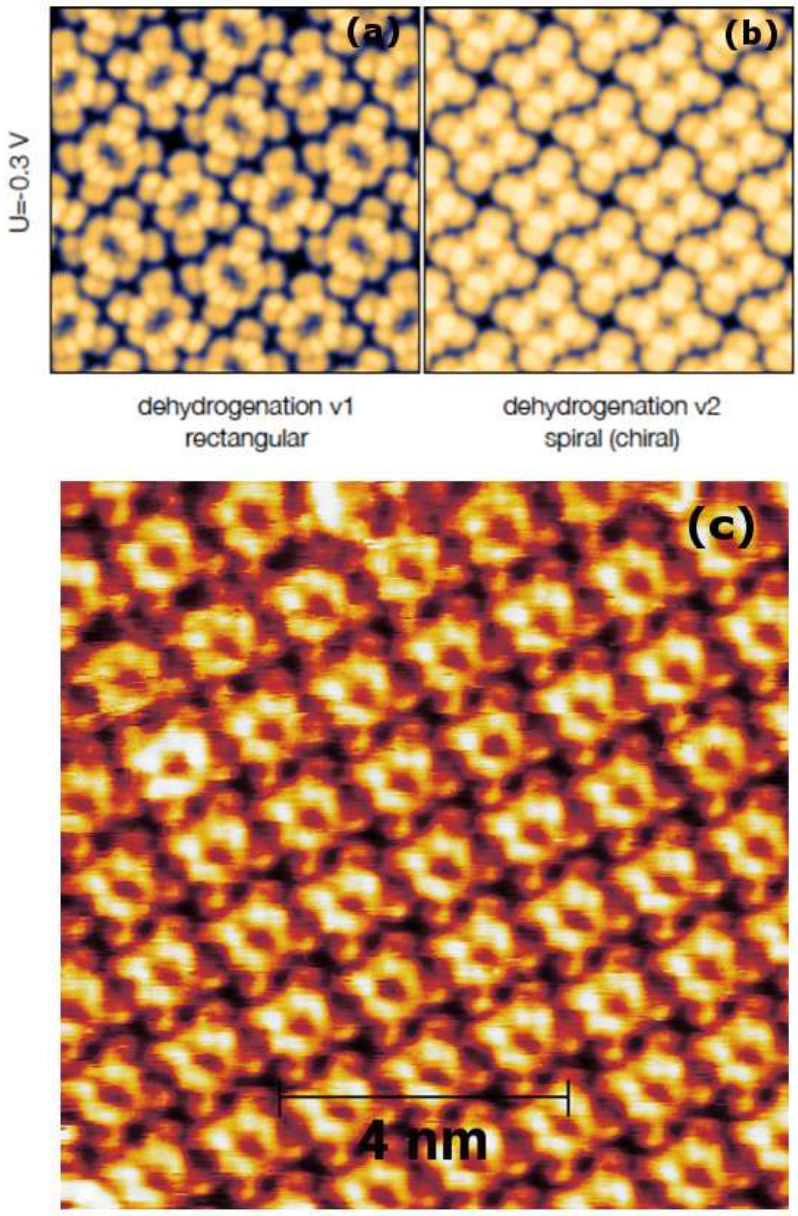

Figure 4.4: Simulated STM micrographs at -0.3 V for 2H-TPP monolayer on Ag(111) in rectangular configuration (a) and in the spiral one (b)compared to the experimental STM image taken at the same voltage (c).

The possible STM micrograph at -0.3 V has also been simulated in both rectangular and chiral cases (Figure 4.3-a and Figure 4.3-b, respectively) and compared with the experimental STM image taken at the same voltage (Figure 4.3-c). The experimental micrograph displays the monolayer obtained after the thermal desorption of the multilayer. Contrary to the rectangular case, the experimental agreement with the simulated images in the chiral case is very good. In this operating condition, the molecular density of states expresses a non-symmetrical charge distribution of the four peripheral phenyl groups, as opposed to a symmetrical charge distribution for the macrocycle. The asymmetry of each phenyl rings corroborates the hypothesis of the carbon de-hydrogenation.

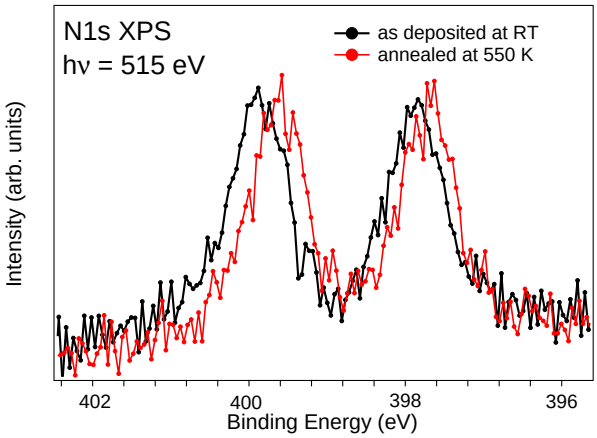

Figure 4.5: N 1*s* XPS spectra of 0.7 ML of 2H-TPP on Ag(111) after RT deposition (triangles) and after annealing at 550 K (circles). The spectra were collected with photon energy hν = 515 eV.

The last proof we need to further test this molecular modification reaction hypothesis is to check what happen when a submonolayer is deposited at room temperature and then annealed at 550 K. Figure 4.6 shows the N 1*s* and C 1*s* NEXAFS spectra of about 0.7 ML of 2H-TPP deposited at RT (top) and after the annealing at 550 K (bottom). The NEXAFS spectra after the RT deposition clearly evidence the phenyl rings rotated in a situation alike the multilayer, with a conformation having the macrocycle flat and the phenyl ring forming a T-shape configuration (Figure 4.6, top). Fitting the NEXAFS spectra at C *K*-edge and considering the area of the absorption peak at $h\nu = 285.3$ eV (which is assigned to the first π^* transition occurring at phenyls) we obtain and average angle of 41$\pm$2° for the phenyl rings with respect to the substrate plane. After the annealing at 550 K a clear rotation of the four peripheral phenyl groups, with their surface rings parallel to the

substrate, is observed (Figure 4.6-b, bottom). We also note that, while the N 1*s* photoemission spectrum does not change (both in intensity and shape) after the annealing (Figure 4.5) indicating that there is no de-protonation of the nitrogen atoms, the N 1*s* NEXAFS spectrum modifies (Figure 4.6-a). This modification is related to the interaction of the macrocycle with the substrate: after the room temperature deposition phenyl rings act like a spacer between the Ag and the macrocycle (with a possible distance of about 5.3 Å), while after the annealing at 550 K the flat rotation of the phenyls reduces the Ag-macrocycle distance to about 2.9 Å increasing the macrocycle interaction. The observed lineshape now is exactly like the monolayer lineshape reported in Figure 4.1-a. In fact, the N 1*s* XPS spectrum of the submonolayer after annealing (Figure 4.5) shifts towards lower binding energy (about -0.3 eV), confirming that after annealing the macrocycle have increased its interaction with the substrate.

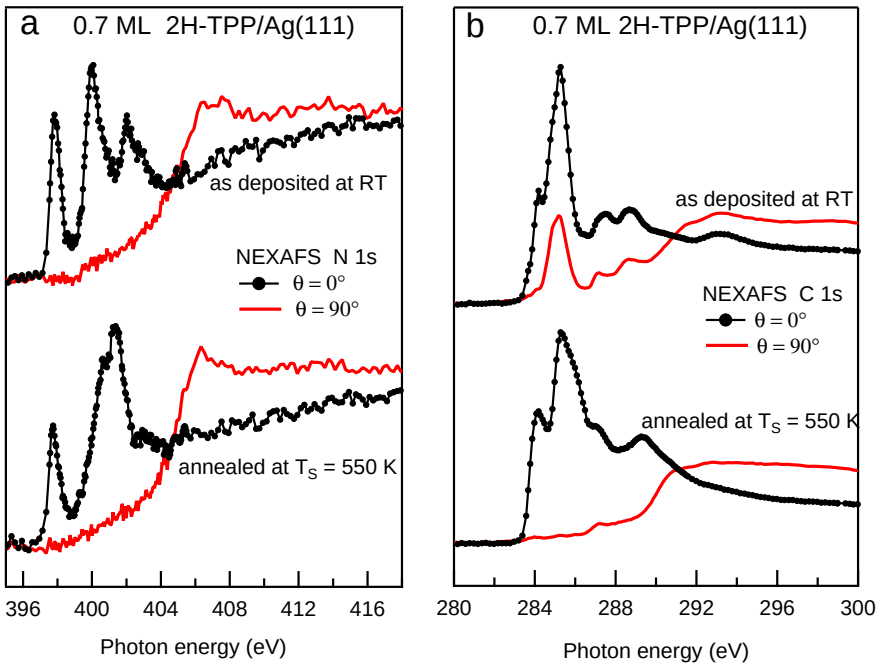

Figure 4.6: NEXAFS spectra at the N 1*s* (a) and C 1*s* (b) absorption thresholds for 0.7 ML of 2H-TPP on Ag(111). The submonolayer is monitored after RT deposition (top spectra) and after annealing at 550 K (bottom spectra). The spectra were collected in two geometries: with the linear light polarization perpendicular ($\theta = 0°$) and parallel ($\theta = 90°$) to the substrate surface.

4.4 Conclusions

In conclusion, we have demonstrated that one monolayer of 2H-TPP prepared by thermal desorption of the corresponding multilayer at 550 K adsorb with both the macrocycle and the phenyl flat on Ag(111). DFT and molecular dynamics calculations suggest a possible molecular reaction and modification of porphyrins to explain this adsorption conformation: the de-hydrogenation of eight carbon atoms in the remaining monolayer after the multilayer desorption with the formation of four new aryl-aryl carbon bonds. The initial presence of the multilayer seems to reduce the aryl-aryl coupling barrier and to select the chiral instead of the rectangular geometry in the modified molecule. The chemical reaction produces a more stable molecule that forms a patterned square lattice on the Ag(111) and that can be eventually further modified by the introduction of the central metal atoms.

Chapter 5

FeTPP/Ag(111)

5.1 Introduction

In-situ metalation of porphyrin and phthalocyanine molecules is of great interest for the characterization of pure species in a controlled environment. A particurarly important aspect of the chemical reactivity is the selective reaction of metal ions with the macrocycle of adsorbed porphyrins and phthalocyanines under vacuum conditions.

Recently, it has been shown that by exposing a monolayer of 2H-5,10,15,20-tetraphenylporphyrin (2H-TPP) anchored on Ag(111) to a beam of Co atoms, the interaction of the cobalt with the porphyrin macrocycle is achieved, resulting in the formation of cobalt(II)-tetraphenylporphyrin (CoTPP). Afterwards, it was attested that 2H-TPP on Ag(111) reacts in a similar way with other metals such as Zn, Ce and Fe [67, 68].

Of considerable interest is the metalation of 2H-TPP with iron under vacuum conditions. Being able to undergo reversible redox reactions, iron porphyrins play a key role in a number of oxidative catalytic processes, such as in hemoglobin and cytochrome P450 [62, 63]. As a counterpart, the high sensitivity toward oxidation renders these molecules very difficult to handle and to sublimate as a pure compound [60]. To stabilize the highly reactive metal, only iron porphyrins with Cl attached are commercially available. Thus, the recent works on Fe-Tetraphenylporphyrin (FeTPP) formation under UHV conditions by exposing free-base TPP monolayers to a beam of Fe has opened up the possibility to characterized the pure compound *in-situ*. Although there are several studies on this subject, in particular related to Fe metalation, the model of the molecular structural configuration and adaptation onto the substrate surface needs to be refined as well as the study of the single layer has to be clarified from the core level spectroscopy point of view

before and after the metalation.

Here we report the characterization of the electronic states and the geometrical adaptation of the molecules during the synthesis of a pure 2H-TPP and FeTTP layers on Ag(111) single crystal. The considerations on the geometry of 2H-TPP monolayer and multilayer assessed in Chapter 4 allows to evaluate possible modification of the molecular configuration due to Fe metalation. By means of high-resolution core levels and valence band X-ray photoemission (XPS) and Near Edge X-ray Absorption Fine Structure (NEXAFS) spectroscopies, performed with Synchrotron radiation source, we directly evaluate the Fe complexes formation and characterize the electronic structure of the specimens when passing from 2H-TPP to FeTPP in both the monolayer and multilayer cases.

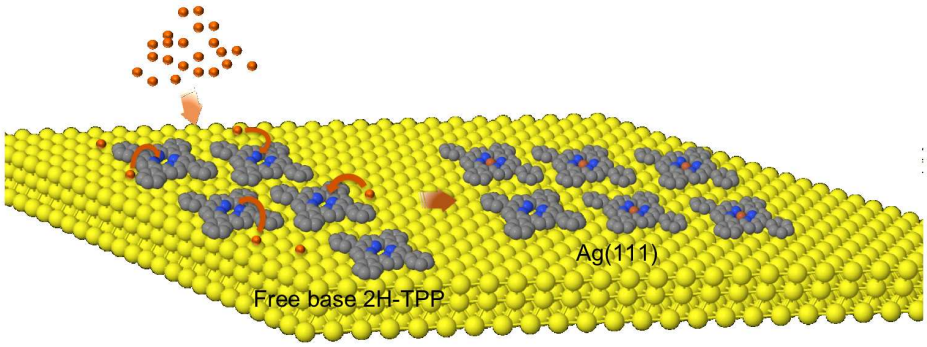

Figure 5.1: *In-situ* metalation of 2H-TPP molecules anchored on Ag(111) by exposing them to a beam of Fe (left). FeTPP formation (right)

5.2 Experimental section

The data have been collected at the ALOISA (NEXAFS) and BACH (Photoemission) beamlines at the Elettra Synchrotron facility in Trieste. All the experiments have been performed in ultrahigh-vacuum experimental chambers at a base pressure of 10^{-10} mbar. Highly purified (99.999 %) commercial 2H-TPP was used and it was sublimated on Ag(111) directly by a home made, resistively heated, Ta evaporator at 570 K. The Ag(111) surface has been prepared by Ar^+ sputtering at 1 keV and annealing at 700 K. The absence of contaminants and the ordering of the surfaces has been checked by means of XPS, Reflective High Energy Electron Diffraction and Low Energy Electron Diffraction techniques. The 2H-TPP monolayers (ML) have been obtained by sublimating a pre-deposited thick film of TPP molecules at $\approx$ 530 K. We therefore define 1 ML of 2H-TPP as the maximum amount of

molecules adsorbed on the substrate surface after the above procedure. Fe atom evaporation has been done by means of a highly focused electron bombardment evaporator (Omicron). After each Fe evaporation the substrate was annealed to $\approx$ 400 K for the metal diffusion.

NEXAFS spectra have been taken in partial electron yield by means of a channeltron facing the sample, while scanning the photon energy across the C and N K-edge with an energy resolution of 100 meV [159]. The low energy secondary electrons have been filtered out by means of a negatively polarized grid (-230 V for the Carbon edge, -370 V for the Nitrogen edge) placed in front of the sample. The orientation of the surface with respect to the linear polarization of the synchrotron beam has been changed by rotating the sample around the beam axis while keeping a constant grazing angle of 6 degrees [49]. This scattering geometry allows to change from linear s-polarization ($\theta = 90°$) to p-polarization ($\theta = 0°$) without variation of the illuminated area on the sample. The raw data were normalized to the total photon flux by dividing the NEXAFS spectrum of the sample with the NEXAFS spectrum taken from the clean substrate in the same experimental conditions.

The XPS data for 1ML TPP on Ag(111) have been collected by means of an hemispherical electron energy analyzer VSW CLASS 150. The analyzer is at 60° from the incident photon beam, in the horizontal plane. The photoemission measurements have been collected with a -4° angular acceptance and a total resolution of 150 meV and 360 meV respectively with a photon energy of 175 eV and 530 eV [160]. The binding energies (BEs) of the photoemission spectra were calibrated using the Fermi level of Ag(111).

5.3 Results and discussion

5.3.1 XPS and NEXAFS study

X-ray photoemission spectra provide the straightforward evidence of the Fe coordination. In particular, the N 1s spectrum of the porphyrin is expected to change when the iron is bound at the center of the macrocycle. In fact, the N 1s spectrum of 2H-TPP has two components that can be easily resolved, whereas the N atoms are equivalent in FeTPP and just one peak is expected. The 2H-TPP spectrum for multilayer reported in Figure 5.2 is composed by two peaks: the one at higher binding energy is assigned to the two pyrrolic N atoms (-NH-), while the lower BE peak corresponds to the two iminic ones (-N=) [127]. The BE values obtained by fitting the spectra and reported in Table 5.1 are in good agreement with similar results already reported in

literature [68].

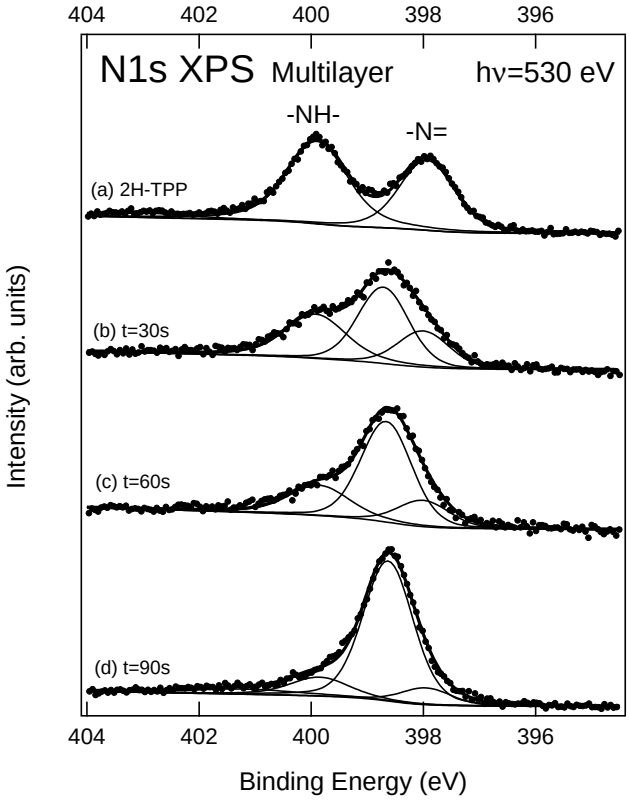

Figure 5.2: XPS spectrum of the N 1s region on a 2H-TPP multilayer before and after Fe deposition steps. The used photon energy was hν = 530 eV. The formation of the peak at BE = 398.6 eV gives evidence of the N-Fe coordination.

Evaporation step	Normalized Peak Area		
	-N=	-NH-	NFe
no Fe (*TPP only*)	0.42	0.58	-
$1^{st}(t_{evap} = 30s)$	0.22	0.33	0.45
$2^{st}(t_{evap} = 60s)$	0.16	0.23	0.61
$3^{st}(t_{evap} = 90s)$	0.09	0.13	0.78
BE *(eV)*	397.9	399.9	398.6

Table 5.1: Formation of FeTPP multilayer on Ag(111): normalized intensity and BE of N 1s components of the photoemission spectra in Figure 5.2.

The immediate deduction looking at Figure 5.2-a is that the pyrrolic peak is larger than the iminic one. The multilayer fit procedure was done

by means of a Shirley background and Voigt integral functions. Using the same gaussian function, the "best fit" returned a gaussian FWHM of 0.65 eV convoluted with the lorentzian peaks associated to the N atoms components. The values for Γ_N and Γ_{NH} (lorentzian width) are 0.74 eV and 0.88 eV respectively. However it is difficult to assert that the two kind of N $1s$ atoms, with such a Γ difference of 0.14 eV, have a different core-hole lifetime that should be related to very distinct de-excitation mechanisms. The core hole de-excitations are mainly due to Auger transitions, therefore it is controlled by the Coulomb matrix elements that might hardly be different in the two cases. On the other hand, the presence of two nitrogen bonded with H introduces different vibrational coupling due to additional N-H bond vibrations [161], which are expected to broaden the pyrrolic peak because of a Franck-Condon mechanism in the photoemission process. The corresponding unresolved fine structure can be effectively taken into account by considering a gaussian broadening of the core-level linewidth. Therefore we made a second fit by assuming that both nitrogen components have the same Γ width and by changing the gaussian FWHM. This gives a $\Gamma = 0.84$ eV and the two FWHM equal to 0.65 eV and 0.59 eV for the pyrrolic and the iminic peaks respectively.

The normalized peak areas, listed in Table 5.1, show a clear uneven proportion of the two N components. We explain the small disproportion between the two N components with a photoelectron diffraction effect. Indeed the ordering of the molecular film enhances the photoelectron diffraction modulation in the experiment geometry (electrons are collected at $\theta = 60°$ with respect to surface normal).

Since core level spectroscopy experiments extract information on the electronic structure, the comparison between NEXAFS and XPS and their data analysis can clarify the electrical character of the molecular film. In Figure 5.3-a we report the NEXAFS spectra at the N K-edges for the 2H-TPP multilayer deposited on the Ag(111) substrate for the angles $\theta = 0°$ and $\theta = 90°$ between the linear light polarization and the normal to the surface. All the NEXAFS spectra of 2H-TPP multilayer and monolayer displayed in this chapter are the same presented in Figure 4.1 of Chapter 5 and will serve here for a direct comparison with the metalized cases.

As expected from the NEXAFS N $1s$ spectrum of Figure 5.3-a, we observe that the first two π^* transitions correspond to the two peaks visible in photoemission indicating that an electron transition from both of the two non-equivalent N $1s$ core levels into the same empty state is allowed. When we take a closer look at the energy positions, we notice that the first π^* peak is shifted towards lower energies by 0.3 eV with respect to the corresponding XPS BE. This generally happens for a semiconducting or insulating system.

In fact, when an atom in an extended system is core ionized, the surrounding system responds trying to screen the hole state. In metallic systems the screening is complete, leading to a final state that is essentially neutral [162]. Therefore the XPS core level binding energy is expected to correspond to the threshold for the NEXAFS spectrum.

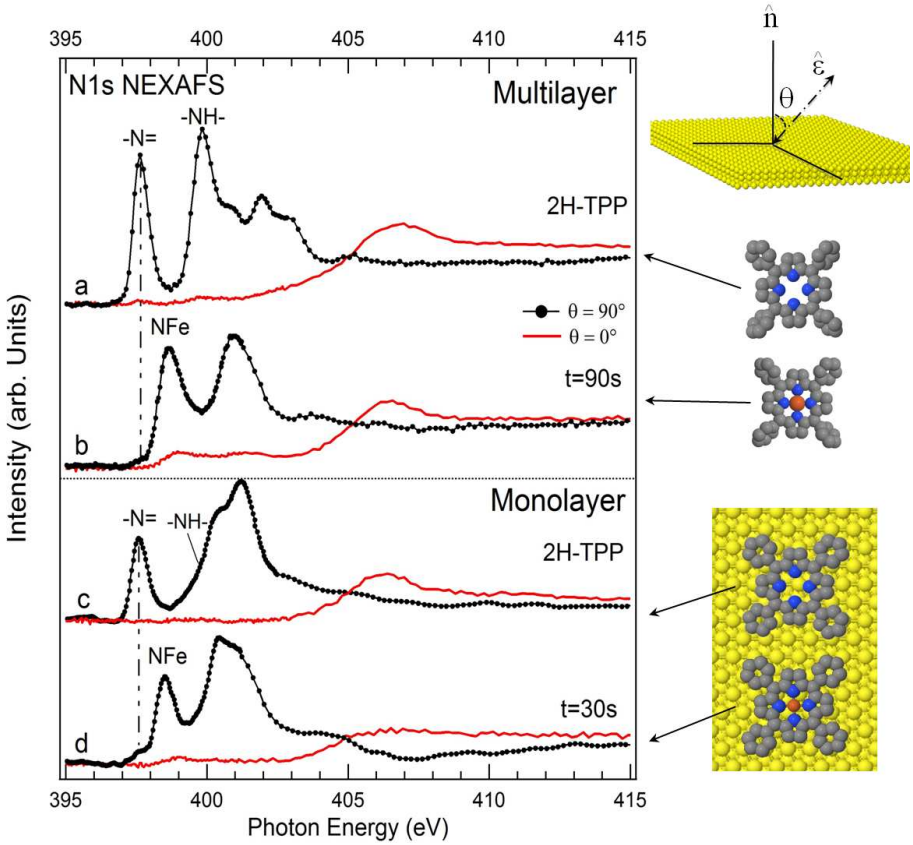

Figure 5.3: NEXAFS spectra at the N 1*s* threshold for multilayer (a,b) and monolayer (c,d). The spectra are taken in linear s-polarization ($\theta = 90°$) to p-polarization ($\theta = 0°$).

This is contrary to the situation for insulating or semiconductor system which are weakly bonded to a metallic surface. The XAS process produces a neutral state while the XPS process produces locally ionic states. Also in this case there is a screening of the core ionization process but it involves no charge transfer to the adsorbed atom or molecule, but it is restricted to a polarization of the substrate. The coupling between the adsorbate and the substrate is in these cases too small for charge transfer to occur on the timescale of the photoionization process. In this case, a difference between the energy of the XAS and XPS spectral features is observed, implying that very different states are reached. In the case of multilayer FeTPP/Ag(111),

the XAS state has the lowest energy and represents the completely screened state, due to Coulomb interaction between the core-hole and the excited electron. This is not reached in XPS due to the weak coupling between the adsorbate and the substrate.

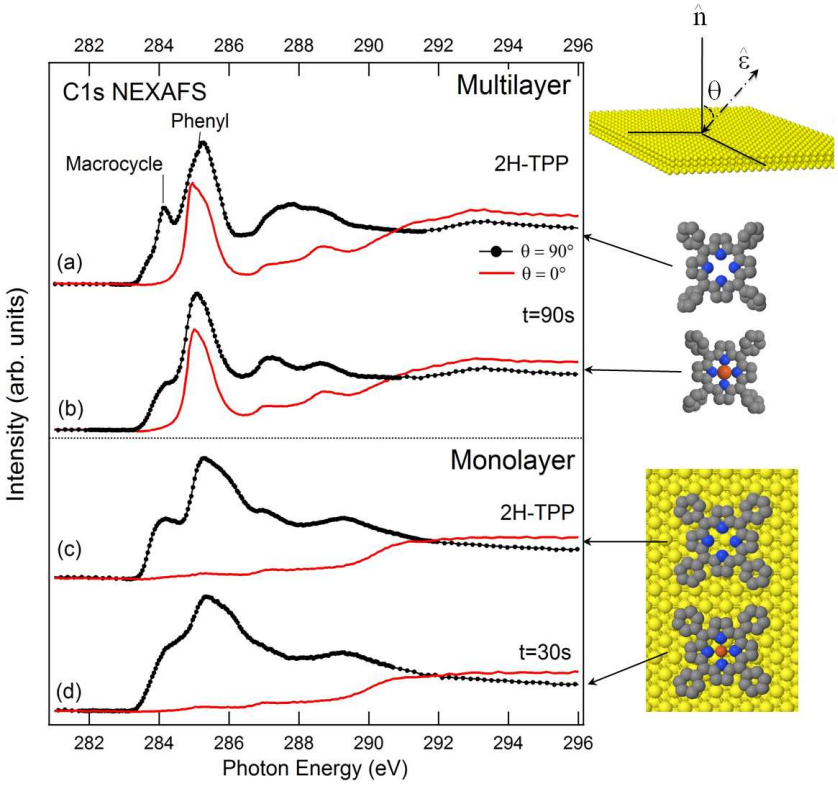

Figure 5.4: NEXAFS spectra at the C 1s threshold for multilayer (a,b) and monolayer (c,d). The spectra are taken in linear s-polarization ($\theta = 90°$) to p-polarization ($\theta = 0°$). The labels "macrocycle" and "phenyl" indicating the main absorption transition are drawn only in spectrum (a) but apply to all the spectra. The label "macrocycle" on the first peak at about 284.3 eV indicates the absorption transitions from core electron states located on carbon atoms in the macrocycle to the macrocycle π^* states, while the label "phenyl" on the second strong peak at about 285.2 eV denotes the transitions occurring from core electron states located on carbon atoms in phenyls to phenyls π^* orbitals.

In the following, the metalation of the multilayer is analyzed. In this case, the multilayer corresponds to approximately 4 layers, as estimated from the attenuation of the Ag 3d signal[1]. With our experimental rate of Fe deposition

[1]The film thickness has been estimated from the equation $I = I_0 \cdot \exp -d/\lambda$, where I_0 is the intensity of the Ag 3d peak before the porphyrin deposition, I is the intensity of the same peak after the porphyrin deposition, d is the film thickness and λ is the depth

we can monitor the metallation of this thin film in resonable experimental time. As already said, the evidence of the *in-situ* complex formation comes from the N 1s spectra taken before and after the Fe evaporation. In Figure 5.2 we show the sequence of the N 1s lineshape changes during Fe evaporation.

The two inequivalent nitrogen components (separated by 2 eV) present in the macrocycle shrink to one as the Fe atoms are evaporated and react with the deposited porphyrin multilayer. The N 1s spectrum changes towards a single peak configuration, which corresponds to 4 equivalent nitrogen atoms in the macrocycle, all unprotonated and coordinated with a single Fe atom. By fitting these core levels we found the pyrrolic peak (-NH-) at BE = 399.9 eV, the iminic N one (-N=) at BE = 397.9 eV and the peak corresponding to the N-Fe bond at BE = 398.6 eV.

As it is shown in Figure 5.2-d, the metalation of the multilayer film was almost complete, since the area corresponding to N-Fe component is the 78% of the total. The Fe atom coordination at the center of the porphyrin macrocycle, evidenced from photoemission measurements, is confirmed by the N 1s absorption spectra (Figure 5.3-b). For example the first two π^* peaks of the 2H-TPP NEXAFS spectrum shrink to a single one located at a photon energy of hν = 398.6 eV (Figure 5.3-b). The presence of a small shoulder at lower energy confirms that not all of the molecules have been metalized. The π^* states at higher photon energies ($>$ 400 eV) are also related to the macrocycle and their changes after the metal evaporation can be associated with the Fe coordination. In particular the whole FeTPP NEXAFS spectrum looks similar to the one of NiTPP [164], further suggesting the bonding of Fe atoms at the center of the macrocycle.

From Figure 5.3-b we notice that the peak at 398.6 eV is not completely quenched when the polarization is in the surface plane ($\theta = 90°$). Even if no clear peaks are visible at $\theta = 90°$, the presence of this feature suggests that, in the FeTPP multilayer, the four nitrogen atoms slightly change their orientation because of the Fe atoms coordination. On the other hand looking at the C 1s NEXAFS (Figure 5.4-b) it is evident that the macrocycle carbon atoms have not changed their orientation. This distortion of the planar configuration, seen for the nitrogen and missing in the case of carbon indicates the unchanged macrocycle orientation with a possible saddle configuration. Differently from the 2H-TPP, in the metalized case (Figure 5.3-b) the absorption peak at 398.6 eV which corresponds to the transition N 1s $\rightarrow$ LUMO appears at the exact BE of the corresponding photoemission core level. This is the case for a metallic or quasi-metallic like behaviour, since the Coulomb

escape for the Ag 3d electrons at the kinetic energy measured in the experiments, which is 20 Åaccording to [163]

interaction is screened by conduction electrons.

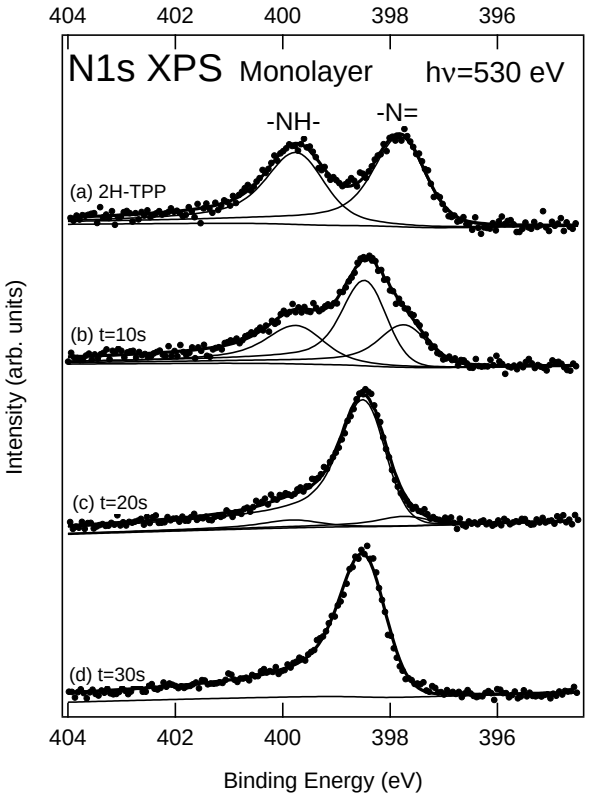

Figure 5.5: XPS spectrum of the N 1*s* region on a 2H-TPP ML before and after Fe deposition steps. The used photon energy was hν = 530 eV. The formation of the peak at BE = 398.4 eV gives evidence of the N-Fe coordination.

The same experiment done for the multilayer has been reproduced for one monolayer. We define the monolayer as the saturated layer obtained by desorbing the multilayer at 550 K. Since the monolayer displays a flat configuration, as evidenced by NEXAFS results (see Figure 5.3-c, Figure 5.3-d and the relative discussion in Chapter 4), the estimated coverage of the clean unreconstructed Ag(111) surface by our XPS measurements for the monolayer is about one 2H-TPP molecule (44 C and 4 N atoms) every 27 Ag atoms [66]. This is in agreement with other determination of the saturated 2H-TPP monolayer on Ag(111) and gives a reliable way to estimate the further amount of Fe deposited. Moreover, it is also clear, taking into account the atomic photo-ionization cross-sections, that the Ag signal is predominant in the overall XPS spectrum and that a large counting statistics is required to highlight the N 1*s* spectrum features. In fact the Ag 3*d* plasmon strongly modifies the XPS background in the N 1*s* region as well as the Ag 3*s* peak

almost superimposes to the Fe $2p$.

The XPS N $1s$ spectra for 2H-TPP monolayer are shown in Figure 5.5. The fit of the N $1s$ core-level spectra of Figure 5.5 has been performed in agreement with the same procedure used for the multilayer. The modification in the background due to the presence of Ag $3d$ plasmons have been taken into account by adding to the fit procedure a polynomial function together with the Shirley background. In addition, the N peaks clearly show a certain degree of asymmetry with respect to the multilayer case, which is typically expected for metallic systems. This can be explained in first place with a strong interaction of the molecule with the metallic substrate which is further emphasized by the presence of the Fe atoms. For this reason the monolayer data "best fit" procedure has been done using Doniach-Sunjic [146] functions, i.e. integral expressions taking into account the peak asymmetry in the photoemission process related to the electronic transitions at very small energy across the Fermi level for metallic systems (for more details, see Appendix A).

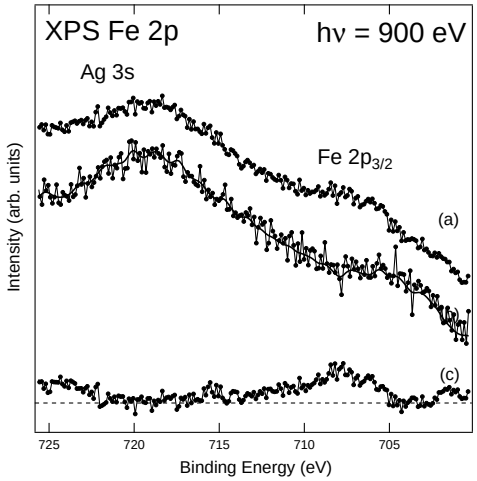

Figure 5.6: (a) XPS spectrum of the Ag $3s$ and Fe $2p_{3/2}$ region on a 2H-TPP ML after Fe deposition (t = 30 s). (b) XPS spectrum of the Ag $3s$ region on the clean Ag(111) (dots) overlapped to the same spectrum after binomial smoothing (line). (c) Difference spectrum obtained by subtracting the smoothed spectrum (b) to spectrum (a). The used photon energy was hν = 900 eV.

First of all, the XPS N $1s$ (but this is true also in the case the XPS C $1s$) molecular peak positions rigidly shifts towards lower binding energies by 0.2 eV with respect to the multilayer case, as evidenced by comparing the values reported in Table 5.1 and in Table 5.2. This is related to an interface

dipole formation with a net charge transfer to the adsorbate layer. Such a strong interaction lead to a high adsorption energy. In fact above 600 K the monolayer molecules start to decompose and it is not possible to desorbe the intact molecules. Moreover this should lead to a decrease of work function of the metal substrate due to the interface dipole formation.

Evaporation step	Normalized Peak Area			α
	-N=	-NH-	NFe	
no Fe (*TPP only*)	0.52	0.48	-	0.11
$1^{st}(t_{evap} = 10s)$	0.28	0.26	0.46	0.13
$2^{st}(t_{evap} = 20s)$	0.075	0.065	0.86	0.19
$3^{st}(t_{evap} = 30s)$	-	-	1.0	0.21
BE *(eV)*	397.7	399.7	398.4	

Table 5.2: Monolayer of Fe-TPP complex formation on Ag(111): normalized intensity, Doniach-Sunjic asymmetry and BE of N 1s components of the photoemission spectra in Figure 5.5.

The peak width of the two components (i.e. -N= and -NH-) is different, as in the multilayer case, and accordingly we fitted the data assuming the same lorentzian width (Γ) and changing the gaussian FWHM. The obtained values are Γ = 0.50 eV and the FWHMs are 0.77 eV and 0.80 eV for the iminic and the pyrrolic peak respectivrly. A clear progression in the asymmetry parameter (α), as the Fe complexation takes place, is also visible and reported in Table 5.2. According to the area values listed in Table 5.1 and Table 5.2 we reckon that, as expected, for the monolayer there is a smaller photoelectron diffraction effect than for the multilayer in this adsorption geometry.

The metalation procedure has lead to an almost fully metalized ML, as shown by the single peak of the N 1s spectrum (Figure 5.5-d), with an evaporation of 0.030 $\pm$ 0.005 ML of Fe (about 1 Fe atom every 4.9 $\pm$ 0.5 N atoms). The spectrum taken in the Fe 2p region for the full FeTPP monolayer formation (t = 30 s, corresponding to Figure 5.5-d) is displayed in Figure 5.6-a. Comparison with the spectrum taken in the same region for the clean Ag(111) (Figure 5.6-b) indicates that, when monolayer Fe metalation is completed, the Fe 2p peak is still a very small structure, hardly distinguishable from the background because of the unavoidable presence of the Ag 3s signal. This is evident from difference spectrum (c), obtained by subtracting the smoothed spectrum (b) from spectrum (a). Binomial smoothing of the experimental spectrum (b) (line in Figure 5.6b) has been adopted for reducing the noise signal in the difference spectrum (c).

For the NEXAFS spectrum we have repeated the iron evaporation procedure on a new ML. In this case the ML metalation was not complete as shown by the small pre-edge feature in Figure 5.3-d. The N 1s NEXAFS of the 2H-TPP ML, shown in Figure 5.3-c, presents the first π^* absorption peak at hν = 397.7 eV as the BE of the N 1s iminic component measured in photoemission. The correspondence with the photoemission BE is found also for the first π^* transition (Figure 5.3-d) in the case of a "fully" metalized 2H-TPP. Again this agrees with the metallic behaviour of the monolayer (both 2H-TPP and FeTPP) as shown by core level XPS and as we will discussed later on by valence band (VB) data. Moreover, the monolayer adsorption orientation and conformation are still controlled through the coupling of phenyl legs to the substrate. The flat conformation of phenyl legs in the monolayer simultaneously predefines the relative molecular orientations and reduces the degrees of freedom for the Fe complex formation towards the already reached lowest energy situation. The influence of the Fe metallic centre in the porphyrin core has only minor effects for the geometry of the macrocycle in the monolayer case.

Finally, our metalation results on the monolayer are in perfect agreement with those obtained by Bai et al. for phthalocyanine metalation on Ag(111) [69]. In fact on this substrate the 2H-TPP lies flat, both with macrocycle and phenyl rings, as the phtalocyanine. Therefore the Fe metalation is probably not a surface mediated process since the flat geometry leaves no space underneath the molecules for Fe diffusion, as instead it would be if the phenyl rings were rotated.

5.3.2 Valence band study

The metal coordination during the deposition of iron atoms can additionally be followed in the valence band region. Aiming to a better understanding of these spectra, we have compared the valence band data of the multilayer with those of the monolayer. Indeed, a parallel experiment has been done to directly obtain a FeTPP monolayer by thermal desorption of the corresponding FeTPP multilayer. In Figure 5.7 we report the valence band data of a FeTPP multilayer (a), of one monolayer of FeTPP (b) obtained by depositing Fe on a monolayer of 2H-TPP and the valence band resulting by the thermal desorption of the metalized FeTPP multilayer (c). The latter (c) almost completely matches the one obtained after step-by-step Fe evaporation (b) indicating the reliability of the two methods. It is worth noting that the whole FeTPP molecular complex has been desorbed from the multilayer, showing that the Fe-porphyrin bond is extremely stable and strong.

The sequence of the ML valence band spectra shown in Figure 5.8 are

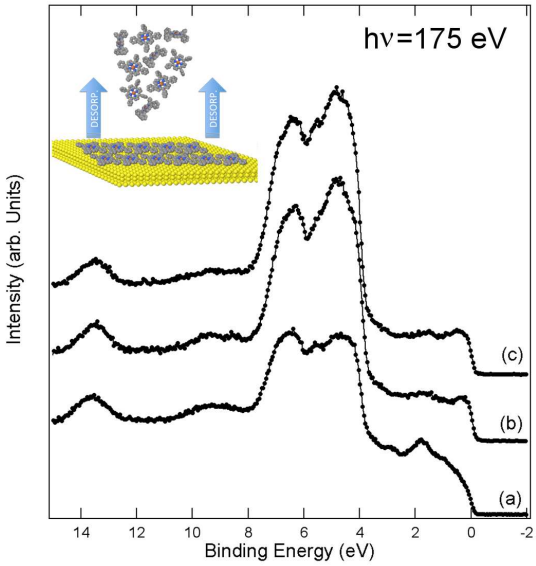

Figure 5.7: Raw data valence band spectra of a FeTPP multilayer (a), of the corresponding ML (b) and the ML obtained by desorption of the multilayer (c). The used photon energy was hν = 175 eV.

raw data subtracted by the valence band of the clean Ag surface taken in the same conditions. This procedure allows the direct visualization of molecular orbitals and modified substrate features as long as the metal coordination takes place, without the strong background of the metallic substrate (Ag 4d at BE = 4.5 eV and Ag Fermi edge as shown in the inset of Figure 5.8).

In the 2H-TPP VB, the HOMO band crosses the Fermi level. This experimental evidence, together with the presence of an asymmety parameter (α) in the XPS N 1*s* fit, the rigid shift of the core level peak positions toward lower BEs and the equivalence in energy of the first NEXAFS N 1*s* absorption peak and the BE of the N 1*s* iminic component, confirms the metallic character of the free-base TPP monolayer. As the metalation proceeds, new features at the Fermi level edge appear (indicated by arrows in inset B) and smoothly increase indicating an overlap between the Fe and the Ag bands in that region. The main change in these spectra is the increasing intensity of the HOMO band that crosses the Fermi level as the iron goes into the macrocycle. Considering that the subtraction exclude any effect coming from the flat and much less intense *sp*-bands of the clean substrate, the growth of the peak near the Fermi level is due to the *d* orbitals of the iron. According to calculations, in fact, in Fe porphyrin isolated molecules HOMO level is expected to have Fe-*d* character [165]. While Fe *d*-states are expected to hybridize with the neighboring N *p*-states in the energy range 1-5 eV below

the Fermi level, a minor hybridization with the N states is predicted for Fe d states near the Fermi level [165] Therefore, we suppose that the charge transfer process from the substrate to the molecules is enhanced by the possible hybridization between the perpendicular d orbitals (i.e. the d_{z^2}) and the silver states.

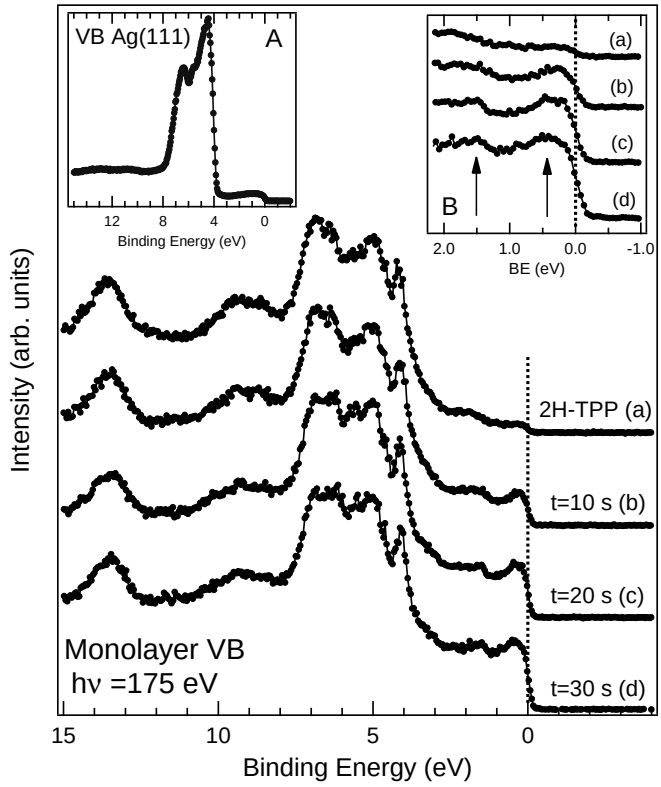

Figure 5.8: Valence Band structure of 2H-TPP ML during Fe metalation. The sequence of the ML valence band spectra are raw data subtracted by the valence band of the clean Ag surface (inset A) taken in the same conditions. The spectral region close to the Fermi edge is magnified in inset B. The used photon energy was hν = 175 eV.

Moreover the visualization of the valence bands is also important for monitoring the Fe adatoms dosing on the molecular layer. In fact an excess of Fe due to cluster like deposition would have immediately resulted in a stronger peak located at the Fermi edge in comparison with the molecular features, which has not been noticed in this case.

To deepen the analysis of the multilayer valence bands we show the sequence of spectra taken during the metalation in Figure 5.9. The effect of the Fe coordination is followed in the bottom panel of Figure 5.9 where the reported valence band has been obtained by subtracting the spectrum of the

2H-TPP multilayer to the valence band after each evaporation step. This procedure highlights the molecular changes during the Fe atoms coordination. The major changes are below 7 eV and in particular there is a clear growth of states near the Fermi level and an apparent metallic behaviour.

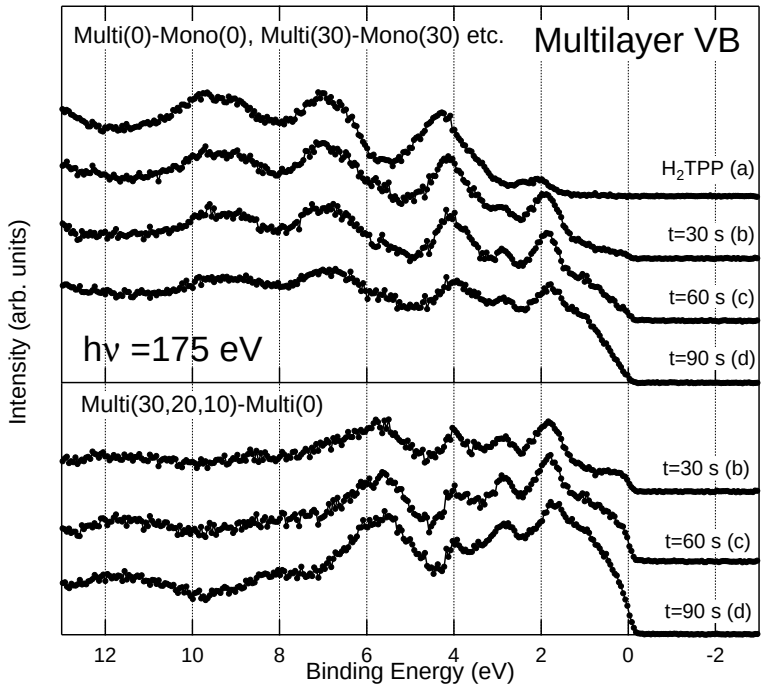

Figure 5.9: Valence band structure of 2H-TPP multilayer during Fe metalation. The reported valence band has been obtained (top panel) by subtracting the spectrum of the 2H-TPP multilayer to the valence band after each evaporation step, (bottom panel) by subtracting from each multilayer spectrum the valence band of the corresponding intermediate step taken on the monolayer. The used photon energy was hν = 175 eV.

In order to highlight the overlayer molecular features, considering that we have only four layer and that the Ag signal is dominant, in the top panel of Figure 5.9 we have subtracted from each spectrum the valence band of the corresponding intermediate step taken on the monolayer reported in Figure 5.8. In this case the ML metalation is assumed to be more or less similar to the corresponding first layer metalation on the multilayer. This method is quite rough, yet we notice that the valence valence band of the 2H-TPP obtained in this way almost completely matches the valence band of the 2H-TPP molecules in gas phase, as observed in Figure 5.10. This is expected from porphyrin molecules, which are known to hardly interact in multilayer systems (see, e.g., Chapter 3 and Chapter 4) and confirms the reliability of

the method applied for obtained the TPP overlayer valence band.

From the spectra in top panel of Figure 5.9 it appears that Fe metalation influences the states near the Fermi level (0-3 eV), but the layers above the first are non-metallic with a density of states that goes almost linearly to zero at the Fermi level. Therefore, the intensity at the Fermi level seen in multilayer valence band is instead due to the metallization of the monolayer. From the comparison between the spectra of Figure 5.8 and those of Figure 5.9 we conclude that the charge injection from the substrate is confined to the first monolayer.

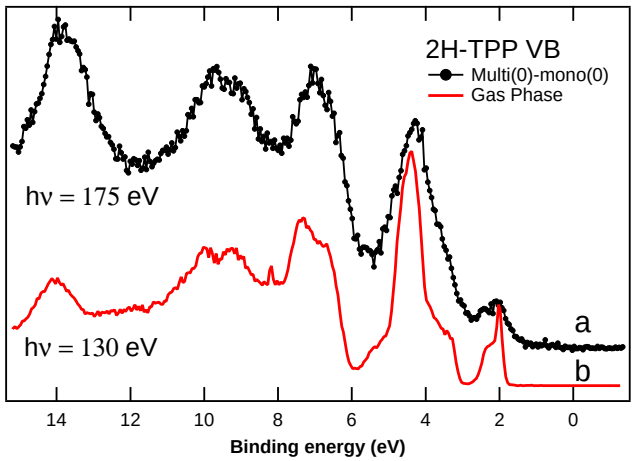

Figure 5.10: Valence Band structure of 2H-TPP multilayer (a) collected with photon energy hν = 175 eV. This spectra is the raw data subtracted by the valence band of the 2H-TPP monolayer taken in the same experimental conditions. Valence Band structure of 2H-TPPP molecules in gas phase (b), collected with photon energy hν = 130 eV.

5.4 Conclusions

In-situ Fe atoms coordination with Tetraphenylporphyrin molecules has been successfully reproduced in UHV on Ag(111), by following an already known recipe [68]. An extensive surface characterization by means of XPS, valence band and NEXAFS with synchrotron radiation source has followed the subsequent coordination steps for the monolayer and multilayer cases.

The study of the monolayer case showed a metallic behaviour for the film, despite of the small Fe atom presence, as confirmed by the XPS fitting functions that have required the introduction of an asymmetry. Both core level and valence band photoemission results have given evidence that the

charge injection from the substrate is more likely confined to the first monolayer. The metallic state of the first layer evolves with Fe complexation due to *d*-states hybridization with the *sp*-bands of the substrate.

As discussed in Chapter 4, the NEXAFS spectra of 2H-TPP monolayer and multilayer, taken in *s* and *p* light polarization at N 1*s* and C 1*s* thresholds, have evidenced the flat configuration for the macrocycle and showed that the phenyl groups lie flat in the case of the monolayer while having non-flat orientation in the multilayer. The multilayer Fe metalation of the TPP molecules favours a macrocycle saddle shape, while in the monolayer the conformation of phenyl legs and the interection with the substrate reduce the degrees of freedom of the macrocycle towards the already reached lowest energy situation. The influence of the Fe metallic centre in the porphyrin core has only minor effects in the monolayer case.

The geometrical adaptation of the molecules in the monolayer has implications on the possible hypothesis for the metalation mechanism. It suggests a diffusion of Iron on the porphyrin film and excludes the hypothesis of a surface mediated dopant diffusion in favor of a simple adatom hopping to the reaction sites.

Chapter 6

FeOEP/Ag(111)

6.1 Introduction

In-situ metalation of free-base tetraphenyl porphyrin molecules with several ions (such Fe, Zn, Co and Ce) has been largely documented by STM imaging micrographs and photoemission studies, performed with laboratory X-ray sources (see, e.g. [67, 68]). In Chapter 5, Fe atoms coordination with Tetraphenyl porphyrin molecules has been successfully reproduced in UHV on Ag(111), and the application of synchrotron radiation based techniques allowed for additional information on the complex electronic structure and geometrical conformation. Nevertheless, to the best of our knowledge, no similar direct metalation experiments have been performed so far on free-base Octa-Ethyl-Porphyrins (2H-OEP). In octaethyl-porphyrins, one ethyl group is attached to each of the eight β carbon atoms belonging to the porphine. In Figure 6.1, the octaethyl-porphyrin is represented when a Fe atom is coordinated in the center of the porphine ring (FeOEP), leading to the removal of the two hydrogens that in the free-base porphyrin (2H-OEP) are bonded to the pyrrole nitrogen atoms.

Recently, the Fe octaethylporphyrins monolayer on ferromagnetic substrates (Co and Ni) has attracted the attention of the scientific community beacuse of its intruguing magnetic properties [33, 135]. In particular, it has been observed that Fe magnetic moment can be switched in plane or out of plane by a magnetization reversal of the substrate. In these experiments, however, only Fe(III)-octaethylporphyrin-Cl molecules have been employed, since the presence of Cl attached to the iron atom is required to stabilize the highly reactive metal at the center [61]. The possibility to produce stable Fe-porphyrins with no Cl atoms and characterize them in situ is therefore of fundamental interest for furher understanding the magnetic properties of

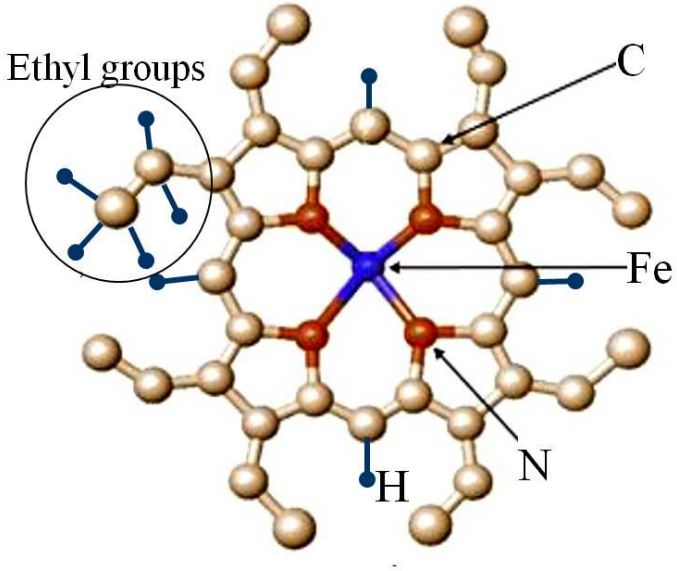

Figure 6.1: Fe octaethyl-porphyrin (FeOEP) molecule. The hydrogen atoms constituting the ethyls are represented for clarity only for one group (inside the black circle).

the Cl-free compound.

Here, the characterization of the electronic states and the molecules geometrical adaptation during the synthesis of pure 2H-octaethylporphyrin (2H-OEP) and Fe octaethylporphyrin (FeOEP) layers on Ag(111) single crystal is reported. Following the assessed recipe for Fe metalation of 2H-TPP, the progressive in-situ metalation of the OEP monolayer and multilayer on the Ag(111) surface has been carried out in UHV environment. Core level spectroscopies directly substantiated the synthesis with information on the complex electronic structure. Additionally, a preliminary study on the geometrical conformation of the molecules is presented.

6.2 Experimental section

The data have been collected at BACH beamline at the Elettra Synchrotron facility in Trieste. All the experiments have been performed in ultrahigh-vacuum experimental chambers at a base pressure of 10^{-10} mbar. Highly purified (99.999 %) commercial 2H-TPP was used and it was sublimated on Ag(111) directly by a home made, resistively heated, Ta evaporator at 570 K. The Ag(111) surface has been prepared by Ar^+ sputtering at 1 keV and annealing at 700 K. The absence of contaminants and the ordering of

the surfaces has been checked by means of XPS and Low Energy Electron Diffraction techniques. The 2H-OEP monolayers (ML) have been obtained by sublimating a pre-deposited thick film of OEP molecules at $\approx$ 530 K. We therefore define 1 ML of 2H-OEP as the maximum amount of molecules adsorbed on the substrate surface after the above procedure. Fe atom evaporation has been done by means of a highly focused electron bombardment evaporator (Omicron). After each Fe evaporation the substrate was annealed to $\approx$ 400 K for the metal diffusion.

NEXAFS spectra have been taken in partial electron yield by means of a 16-channel detector, while scanning the photon energy across the and N K-edge with an energy resolution of 100 meV. The absorption spectra were recorded in partial electron yield, collecting simultaneously the photocurrent emitted by the sample and the reference current I_0 from the horizontal refocusing mirror of the beamline as a function of the incident photon energy. The NEXAFS data were normalized by the reference I_0 to the absorption edge jump, and the energy scale was always calibrated with XPS photoemission spectra in the region of Ag $3d_{5/2}$ (BE = 368.1 eV).

To observe dichroism, the NEXAFS spectra have been recorded at RT with two different geometries; in both cases horizontally polarized radiation was used (better than 99 %) changing the direction of the incident radiation from normal (90° with respect to the surface plane) to grazing angle (30° with respect to the surface plane). Since the light polarization vector is perpendicular to the synchrotron beam, this corresponds to an angle θ between the light polarization vector and the normal to the surface of 90° (in plane polarization) and 30° (out-of-plane polarization), respectively.

The XPS data for 1ML OEP on Ag(111) have been collected by means of a hemispherical electron energy analyzer VSW CLASS 150. The analyzer is at 60° from the incident photon beam, in the horizontal plane. The photoemission measurements have been collected with a -4° angular acceptance and a total resolution of 150 meV and 360 meV respectively with a photon energy of 175 eV and 530 eV [160]. The binding energies (BEs) of the photoemission spectra were calibrated using the Fermi level of Ag(111).

6.3 Results and discussion

6.3.1 XPS and NEXAFS study

As in case of 2H-TPP (see Chapter 5.3.1), the changes in X-ray photoemission N 1s spectrum are used to evidence the Fe coordination. In fact, the two components in the N 1s spectrum of 2H-OEP (representing two inequivalent

N atom species) are expected to merge in a single peak when Fe atoms coordinate in the macrocycle.

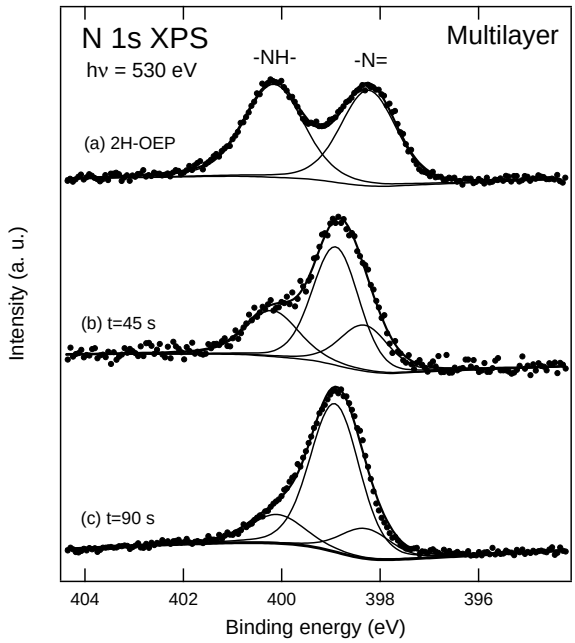

Figure 6.2: XPS spectrum of the N 1s region on a 2H-OEP multilayer before and after Fe deposition steps. The used photon energy was hν = 530 eV. The formation of the peak at BE = 398.9 eV gives evidence of the N-Fe coordination.

The 2H-OEP spectrum for multilayer has been reported in Figure 6.2. The multilayer corresponds to approximately 4 layers, as estimated from the attenuation of the Ag 3d signal. Such a thin film should guarantee the possibility to follow the Fe metalation of the OEP overlayer in a reasonable experimental time, as demonstrated in Chapter 5 for TPP multilayer. In the N 1s spectrum of multilayer the peak at higher binding energy is assigned to the two pyrrolic N atoms (-NH-), while the lower BE peak corresponds to the two iminic ones (-N=) [127]. The BE values obtained by fitting the spectra are reported in Table 6.1 and indicate that in 2H-OEP multilayer, while the energy distance between the two components remains constant (2 eV), the N 1s peak positions shift of about 0.3 eV toward higher binding energy with respect to the 2H-TPP miltilayer case (see Table 5.1).

The multilayer fit procedure was done by means of a Shirley background and Voigt integral functions. As for TPP experiments, we assume that both nitrogen components have the same lorentian Γ width but different gaussian FWHM. This gives a Γ=0.85 eV and the two FWHM equal to 0.56 eV and 0.8 eV for the pyrrolic and the iminic peaks respectively. While Γ and the

Evaporation step	Normalized Peak Area		
	-N=	-NH-	NFe
no Fe (*OEP only*)	0.52	0.48	-
$1^{st}(t_{evap} = 45s)$	0.23	0.23	0.54
$2^{st}(t_{evap} = 90s)$	0.16	0.16	0.68
BE *(eV)*	398.2	400.2	398.9

Table 6.1: Formation of FeOEP multilayer on Ag(111): normalized intensity and BE of N 1s components of the photoemission spectra in Figure 6.2.

FWHM of the pyrrolic components are quite similar to the corresponding values of the 2H-TPP multilayer spectrum, the FWHM of the iminic peak is notably larger.

This value can be explained by assuming that the iminic peak actually consists of two components. The splitting of the iminic components can be deduced also by NEXAFS spectra at the N K-edges for the 2H-OEP multilayer (Figure 6.3-a), in which it is evident that at least two components are required to account for the shape of the low energy absorption peak at hν = 397.7 eV, i.e. the peak of the N 1$s \rightarrow \pi^*$ transition for the iminic groups (-N=). The presence of two components in the iminic peak of both N 1s XPS and NEXAFS spectra indicates that the two N iminic atoms (-N=) are not equivalent in the macrocycle. The breaking of symmetry in the molecule may be induced, for exemple, by the particular packing configuration assumed by 2H-OEP molecules in multilayer, as discussed later.

Accordingly to the previous discussion, a new fit for the N 1s XPS spectrum of 2H-OEP multilayer has been made (not reported). While the fit parameters for the pyrrolic peak result the same, the two components of the iminic peak are found at BE = 398.0 eV and BE = 398.6 eV, with a very similar area.

However, since in the following discussion on Fe metalation we are only interested in the evolution of the Fe-N peak in comparison with the total area of the components of the unmetalated molecules, the iminic peak will be fitted with only one component for simplicity.

The molecular order of 2H-OEP molecules in multilayer can be inspected through the linear polarization dependence of the NEXAFS spectra. In Figure 6.3-a we report the NEXAFS spectra at the N K-edges for the 2H-OEP multilayer deposited on the Ag(111) substrate for the angles $\theta = 90°$ and $\theta = 30°$ between the light polarization vector and the normal to the surface. Spectra are normalized to the intensity of the σ^* states at hν = 415 eV.

In Figure 6.3-a the first two π^* transitions separated by 2 eV correspond to the two peaks visible in photoemission, indicating that an electron transition from both of the pyrrolic and iminic N 1s core levels into the same empty state is allowed. If we focus on the polarization dependance of the first peak at hν = 397.7 eV representing the N 1s $\rightarrow$ π^* transition for the iminic groups (-N=), which is well separated from the remaining absorption transition peaks, we don't observe a complete quenching of the π^* states at $\theta = 90°$, as in case of 2H-TPP multilayer (see Chapter 4).

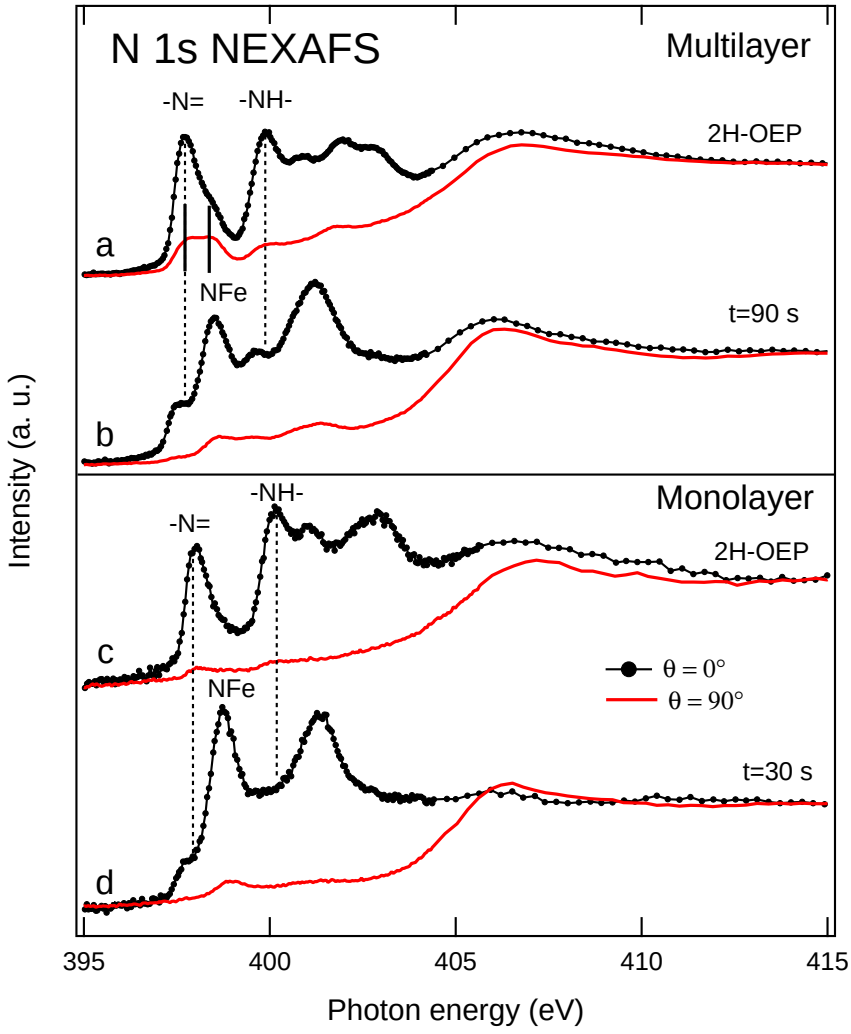

Figure 6.3: NEXAFS spectra at the N 1s threshold for multilayer (a,b) and monolayer (c,d). The spectra are collected with an angle θ between the light polarization vector and the normal to the surface of $\theta = 90°$ (in plane polarization) and $\theta = 30°$ (out of plane polarization), respectively.

In order to determine the polarization dependance of the area of the first peak, we accomplished the deconvolution of the NEXAFS spectra by performing a nonlinear least-squares fitting on the experimental data, usign gaussian functions, the so-called error functions ("erf") background with exponential decay and an additional linear background. As discussed before, the first peak assignd to the N $1s \rightarrow \pi^*$ transition for the iminic groups (-N=) clearly consists of two components and it is therefore reproduced in the fit by two gaussian function at hν = 397.7 eV and hν = 398.3 eV (the position of the two gaussian function are indicated in Figure 6.3-a by thick bars). Incidentally, the difference in position of these two components (0.6 eV) is equal to that found for the corresponding components in the N $1s$ XPS spectrum fit, supporting the previuos analysis made on N $1s$ spectrum.

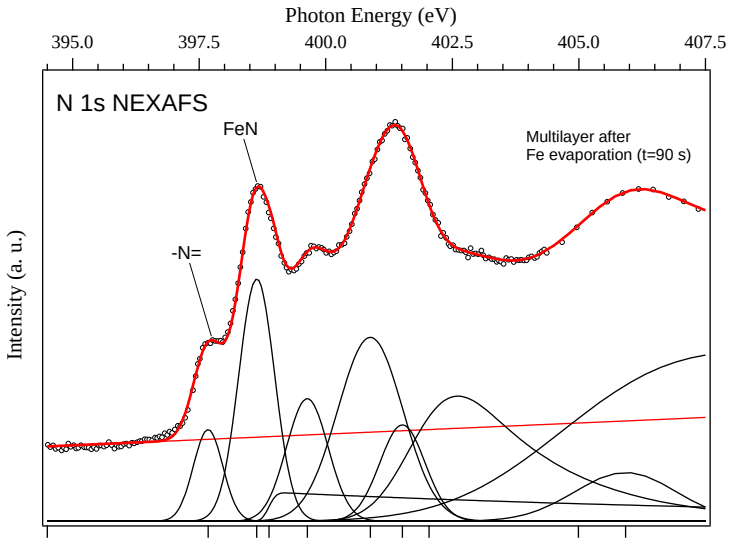

Figure 6.4: NEXAFS spectra at the N $1s$ threshold of a multilayer after Fe evaporation (t = 90 s). The spectrum has been fitted with gaussian components (bottom part), which have been shifted in intensity by an arbitrary constrant for clarity. In particular, the first peak at hν = 397.7 eV derived from the -N= groups of the not metalated molecules in the monolayer, while the second one (hν = 398.6 eV) correspond to the first absorpion transition from N $1s$ core level of the metalated molecules.

By fitting the total area of the first peak as a function of the linear polarization angle with the equation 2.30, we obtain an average tilt angle of $36° \pm 5°$ between the π^* orbitals of -N= atoms and the substrate. Since the N atoms are only located within the macrocycle and π^* orbitals lie perpendicular to the macrocycle plane itself, this value indicates the angle between the molecular macrocycle and the Ag surface.

Another interesting information is obtained by looking at the energy po-

sitions of the two components in the first π^* peak, which are shifted towards lower energies by 0.3 eV with respect to the corresponding XPS BE. This generally happens for semiconducting systems, as observed for 2H-TPP multilayer, and it is due to Coulomb interaction between the core-hole and the excited electron.

In the following, the metalation of the multilayer is analyzed. The evidence of the *in-situ* complex formation comes from the N 1s XPS spectra taken before and after the Fe evaporation. In Figure 6.2 we show the sequence of the N 1s lineshape changes during Fe evaporation.
As motivated before, for iminic peak we have considered the values resulting when only one component is used in the fit. The two inequivalent nitrogen components (separated by 2 eV) that are present in the macrocycle shrink to one as the Fe atoms are evaporated and react with the deposited porphyrin multilayer. In fact, Fe atoms are inserted in the macrocycle and the four nitrogen atoms turn to be all equivalent. By fitting these core levels we found the pyrrolic peak (-NH-) at BE = 400.2 eV, the iminic N one (-N=) at BE = 398.2 eV and the peak corresponding to the N-Fe bond at BE = 398.9 eV. In Table 6.1, the normalized peak areas of N 1s spectra are listed. As it can be observed in Figure 6.2-c, the metalation of the multilayer film is almost complete, since the area corresponding to N-Fe component is the 68% of the total.

The Fe atom coordination at the center of the porphyrin macrocycle is also confirmed by the N 1s absorption spectra (Figure 6.3-b). Indeed, the first two π^* peaks of the 2H-OEP NEXAFS spectrum shrink to a single one located at a photon energy of about hν = 398.6 eV (Figure 6.3-b). The presence of a shoulder at lower energy confirms that not all of the molecules have been metalized.

From Figure 6.3-b it can be noted that, also in this case, the peak at about 398.6 eV is not completely quenched when the polarization is in the surface plane ($\theta = 90°$). The fitted N 1s NEXAFS spectrum of the almost metalized 2H-OEP multilayer for ($\theta = 30°$) is displayed in Figure 6.4, as an example. In particular, it is shown that the first peak at hν = 397.7 eV derives from the -N= groups of the not metalated molecules in the multilayer[1], while the second one (hν = 398.6 eV) corresponds to the first absorpion transition from N 1s core level of the metalated molecules. By fitting the area of the peak at hν = 398.6 eV as a function of the linear polarization angle, we obtain an

[1]Since the intensity of this peak is low compared with the intensity of the peak at hν = 398.6 eV, in the fit we have used for simplicity just one component for the unmetalated peak instead of the two found in the N 1s NEXAFS spectra fit of the 2H-OEP multilayer (Figure 6.3-a). This choice hardly affects the results of the polarization dependence presented here.

average tilt angle of $27° \pm 5°$ between the macrocycle plane and the surface of the substrate. This suggest that the four nitrogen atoms slightly change their orientation because of the Fe atoms coordination. However these results must be taken with caution, because the fits are based on only two angles and C 1s NEXAFS are not available for confirming the orientation of the whole macrocycle. It should be reminded, in fact, that in case of Fe metalization of the 2H-TPP multilayer, only the combination of the C 1s NEXAFS and N 1s NEXAFS data allowed to determine a distortion of the planar configuration of the macrocycle, which cannot be hypothized for metalized OEP through the N 1s NEXAFS data only.

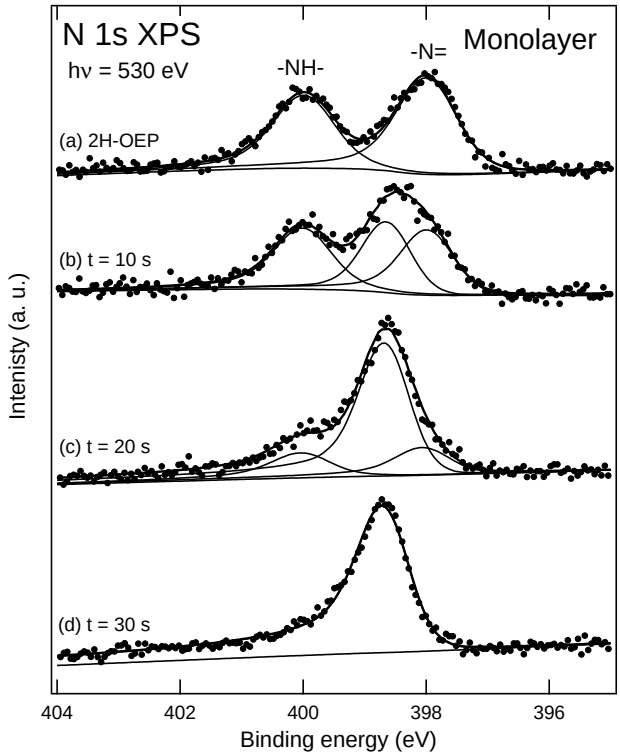

Figure 6.5: XPS spectrum of the N 1s region on a 2H-OEP ML before and after Fe deposition steps. The used photon energy was hν = 530 eV. The formation of the peak at BE = 398.4 eV give evidence of the N-Fe coordination.

Unlike the TPP multilayer case, in the metalized case (Figure 6.3-b) the first transition appears at a BE lower than the corresponding photoemission core level, indicating that the core hole is not efficiently screened by the sourrounding electrons as in metalated TPP molecules.

The same experiment done for the multilayer has been reproduced for one monolayer. We define the monolayer as the saturated layer obtained by

desorbing the multilayer. Being the Ag signal predominant in the overall XPS spectrum, a large counting statistics is required to highlight the N 1s spectrum features, with the Ag 3d plasmon that strongly modifies the XPS background in the N 1s region.

The XPS N 1s spectra for 2H-OEP monolayer are shown in Figure 6.5. The fit of the N 1s core-level spectra of Figure 6.5 has been performed in agreement with the same procedure used for the multilayer. The modification in the background due to the presence of Ag 3d plasmons have been taken into account by adding to the fit procedure a polynomial function together with the Shirley background. As for the XPS N 1s spectra of the TPP monolayer, the N peaks clearly show a certain degree of asymmetry with respect to the multilayer case, which is typically expected for metallic systems. Also in this case, the strong interaction of the molecule with the metallic substrate which is further emphasized by the presence of the Fe atoms is taken into account by using Doniach-Sunjic [146] functions in the "best fit" procedure (for more details, see Appendix A).

The comparison of the values reported in Table 6.1 and in Table 6.2 evidences that the XPS N 1s positions of all molecular peaks rigidly shifts towards lower binding energies by 0.3 eV with respect to the multilayer case, as observed for the TPP molecules. Again, we relate this effect to an interface dipole formation with a net charge transfer to the adsorbate layer. This strong interaction is manifested through a high adsorption energy, confirmed by the observation that above 550 K the monolayer porphyrins start to decompose and it is not possible to desorbe the intact molecules.

As done for the multilayer case, we have fitted the N 1s spectrum of the free-base OEP monolayer (Figure 6.5-a) by assuming the same lorentzian width (Γ) and different gaussian FWHMs for all the components. In this manner, we have obtained $\Gamma = 0.52$ eV and the FWHMs 0.74 eV and 0.79 eV for the iminic and the pyrrolic peak, respectively. These value are very close to those found from fit of the N 1s XPS spectrum of 2H-OEP monolayer. A clear progression in the asymmetry parameter (α), as the Fe complexation takes place, is also visible and reported in Table 6.2.

Before checking the molecular conformation on the substrate, we focus on the metalation of 2H-OEP molecules. The metalation procedure has lead to an almost fully metalized ML, as shown by the single peak of the N 1s spectrum (Figure 6.5-d). For the NEXAFS spectra we have repeated the iron evaporation procedure on a new ML. In this case, metalation was not complete as shown by the small pre-edge feature in Figure 6.3-d. The N 1s NEXAFS of the 2H-OEP ML, shown in Figure 6.3-c, presents the first π^* absorption peak at h$\nu = 398.0$ eV, i.e. at the same BE of the N 1s iminic component measured in photoemission. Thus, 2H-OEP monolayer has a

Evaporation step	Normalized Peak Area			α
	-N=	-NH-	NFe	
no Fe (*OEP only*)	0.55	0.45	-	0.05
$1^{st}(t_{evap} = 10s)$	0.35	0.33	0.32	0.06
$2^{st}(t_{evap} = 20s)$	0.17	0.15	0.68	0.12
$3^{st}(t_{evap} = 30s)$	-	-	1.0	0.20
BE *(eV)*	398.0	400.0	398.7	

Table 6.2: Formation of FeOEP monolayer on Ag(111): normalized intensity, BE and Doniach-Sunjic asymetry of N 1s components of the photoemission spectra in Figure 6.5.

metallic character as the 2H-TPP monolayer. The correspondence with the photoemission BE is found also for the first π^* transition (occurring at hν = 398.7 eV, Figure 5.3-d) of a "fully" metalized 2H-OEP. Again this agrees with the metallic behaviour of the monolayer, as shown by core level XPS and valence band (VB) data (see next section).

Finally, the monolayer adsorption orientation is checked by polarization dependence of N 1s NEXAFS spectra. From Figure 6.3-c it can be noted that the peak at hν = 398.0 eV is not completely quenched when the polarization is in the surface plane ($\theta = 90°$). Fitting the area of this peak as a function of the linear polarization angle we obtain an average tilt angle of $17° \pm 5°$ between the macrocycle plane and the surface of the substrate. On the other hand, by fitting the area of the peak hν = 398.7 eV in Figure 6.3-d as a function of the linear polarization angle, a tilt angle of $21° \pm 5°$ between the macrocycle plane and the surface of the substrate is calculated. It is hard to say if the coordination of Fe atoms may alter the film ordering, because the angles found before and after Fe evaporation in the monolayer experiments are equal within the error bars ($\pm$ 5°).

The angles found for 2H-OEP and FeOEP monolayer are not unexpected for octaethylporphyrins. For example, we have measured the NEXAFS spectra at both the N and C K-edges of a monolayer of cobalt octaethylporphyrins (CoOEP) adsorbed on Ag(110) (Figure 6.6-a and -b), and their dichroic behaviour indicates that each molecular macrocycle is tilted with respect to the metal surface by about 20° [125].
In that study, calculations on the possible orientation of 2H-OEP (without Co) in a c-5x5 unit cell[2] have been also made [125]. In these calculations only the steric interaction is considered, thus neglecting the Ag substrate.

[2]This choice is motivated because a c-5x5 unit cell configuration is observed for CoOEP monolayer on Ag(110) in experimental scanning tunneling microscopy (STM) images [125].

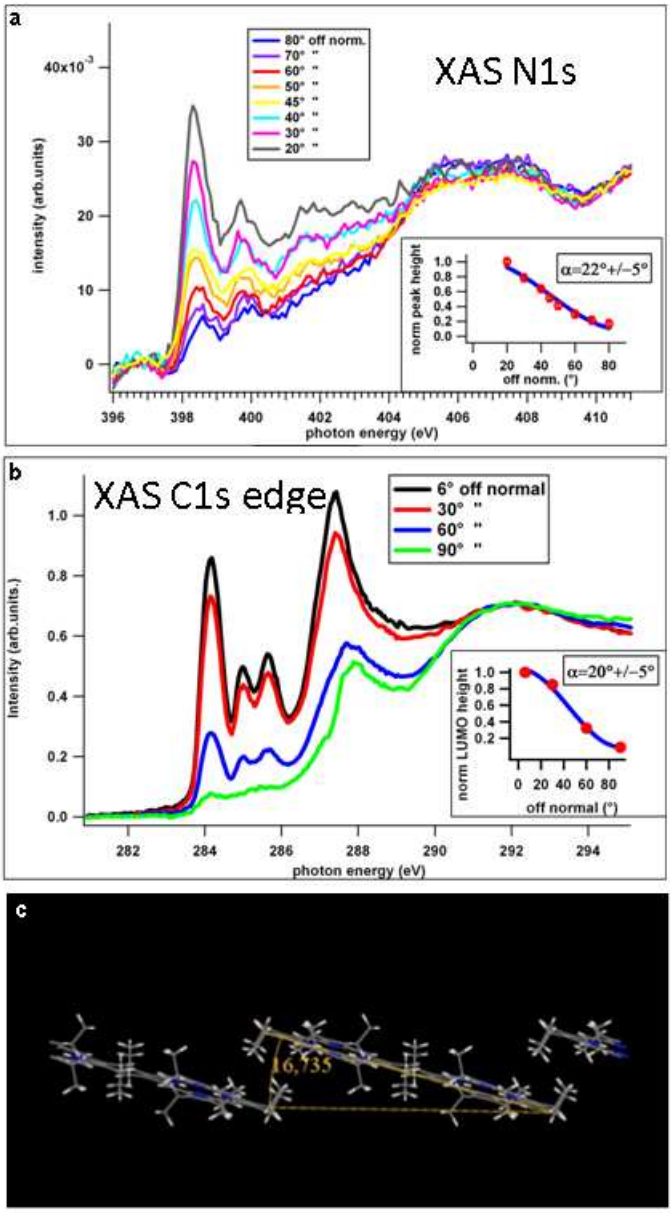

Figure 6.6: (a) NEXAFS spectra at the N K-edge of CoOEP monolayer on Ag(110). These spectra have been collected with different polarization directions of the light with respect with the normal to the Ag(110) plane. In the inset, the normalized intensity of the first peak for each spectrum is plotted (red dots) along with the fit (blue line) using the angular dependence function given in Ref. [47]. (b) same as (a) for the C K-edge. (c) equilibrium configuration of 2H-OEP molecules in a c(5x5) lattice obtained by calculations. Figure adapted from [125].

The minimum-energy configuration of such a monolayer is achieved when the molecules are tilted about 17° with respect the surface plane to optimize steric hindrance, as displayed in Figure 6.6-c. From theoretical results, it has been deduced that the experimental geometry of the CoOEP monolayer arises from a trade off between the molecule/metal interaction (which determines the periodicity of the interface) and the repulsive molecule/molecule interaction (which determines the tilt of the molecules) and is not governed by the specific metal centre. These conclusions are in agreement with the similar tilt angles that have been experimentally measured for 2H-OEP and FeOEP monolayer on Ag(111), confirming the adsorption angle is unlikely to be determined neither by the metal center nor by the choice of the substrate.

The average tilt angles of the porphyrin macrocycle with respect to the surface plane resulting from polarization dependence of NEXAFS spectra are summarized in Table 6.3.

Evaporation step	Film	Substrate	Average tilt angle
no Fe (OEP only)	Multi	Ag (111)	$36° \pm 5°$
Fe evaporation (t = 90s)	Multi	Ag (111)	$27° \pm 5°$
no Fe (OEP only)	Mono	Ag (111)	$17° \pm 5°$
Fe evaporation (t = 90s)	Mono	Ag (111)	$21° \pm 5°$
CoOEP [125]	Mono	Ag (110)	$20° \pm 5°$
2H-OEP (simulations) [125]	Mono	no	$17° \pm 5°$

Table 6.3: Average tilt angles of the porphyrin macrocycle with respect to the surface plane for 2H-OEP molecules on Ag(111), before and after Fe evaporation, both in multilayer and monolayer films. These results derives from polarization dependence of NEXAFS spectra displayed in Figure 6.3. In addition, the average tilt angles of CoOEP monolayer on Ag(110) (obtained in NEXAFS measurements) and of 2H-OEP monolayer (induced in calculations) are reported from Ref. [125].

It is worth noting that 2H-OEP molecules clearly change their orientation on going from multilayer to monolayer (before evaporation, α goes from an average angle of 36° to 17°). Evidently, the non-bonding forces (like van der Waals) and the steric repulsion between the hydogens composing the ethyl groups and the hydrogens attached to the carbon bridges are optimized in multilayer by further tilting the macrocycle planes. The molecular packing achieved in multilayer may also be responsible of the chemical alterations observed for the macrocycle, for which the two iminic atoms are not equivalent as in the free molecule.

6.3.2 Valence band study

The effect of metal coordination during the deposition of iron atoms are also observable in the valence band region.

As in case of TPP, we have performed a parallel experiment to directly obtain a FeOEP monolayer by thermal desorption of the corresponding FeOEP multilayer. In Figure 6.7 we report the valence band data of a FeOEP multilayer (a), of one monolayer of FeOEP (b) obtained by depositing Fe on a monolayer of 2H-OEP and the valence band resulting by the thermal desorption of the metalized FeOEP multilayer (c). The latter (c) catches the main features of the one obtained after step-by-step Fe evaporation (b) indicating the reliability of the two methods in case of OEP likewise for TPP.
It is worth noting that the whole FeOEP molecular complex has been desorpted from the multilayer, showing that the Fe-porphyrin bond is extremely stable and strong.

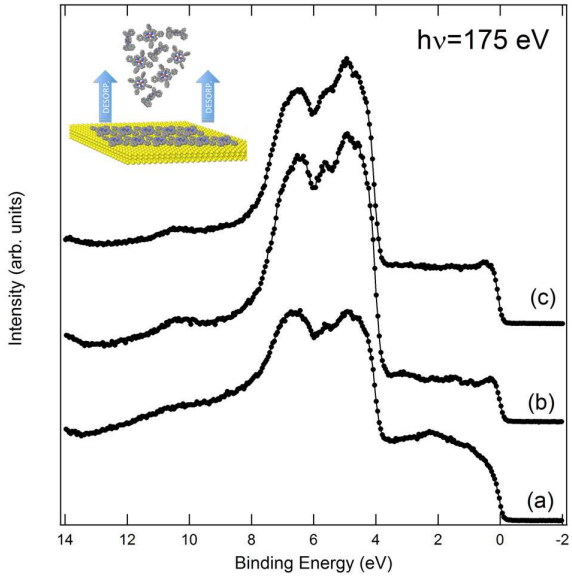

Figure 6.7: Raw data valence band spectra of a FeOEP multilayer (a), of the corresponding ML (b) and the ML obtained by desorption of the multilayer (c). The used photon energy was hν = 175 eV.

The sequence of the ML valence band spectra shown in Figure 6.8 are raw data subtracted by the valence band of the clean Ag surface taken in the same conditions. As pointed out in Chapter 5.3.2, this procedure allows, by removing the strong background of the metallic substrate (Ag 4d at BE = 4.5 eV and Ag Fermi edge), to highlight the modifications on molecular orbitals during the metal coordination.

Likewise the 2H-TPP monolayer, in the 2H-OEP VB the HOMO band crosses the Fermi level. This experimental evidence, together with the presence of an asymmety parameter (α) in the XPS N 1s fit, the rigid shift of the core level peak positions toward lower BEs and the equivalence in energy of the first NEXAFS N 1s absorption peak and the BE of the N 1s iminic component, confirms the metallic character of the free-base OEP monolayer. As the metalation proceeds, new features in the 0-7 eV energy range appear and smoothly increase. The main change in these spectra is, however, the increasing intensity of the HOMO band that crosses the Fermi level (indicated by an arrow) as the iron goes into the macrocycle. As discussed in Chapter 5.3.2 the growth of the peak near the Fermi level is assigned to the d orbitals of the iron. In fact, calculations for Fe porphyrin isolated molecules predicted that HOMO level has Fe-d character, with a minor hybridization with the N states [165]. Instead, Fe d-states are expected to hybridize with the neighboring N p-states in the energy range 1-5 eV below the Fermi level [165]. Therefore, we hypothesize also for FeOEP on Ag(111) that the charge transfer process from the substrate to the molecules is enhanced by the possible hybridization between the perpendicular d orbitals (i.e. the d_{z^2}) and the silver states.

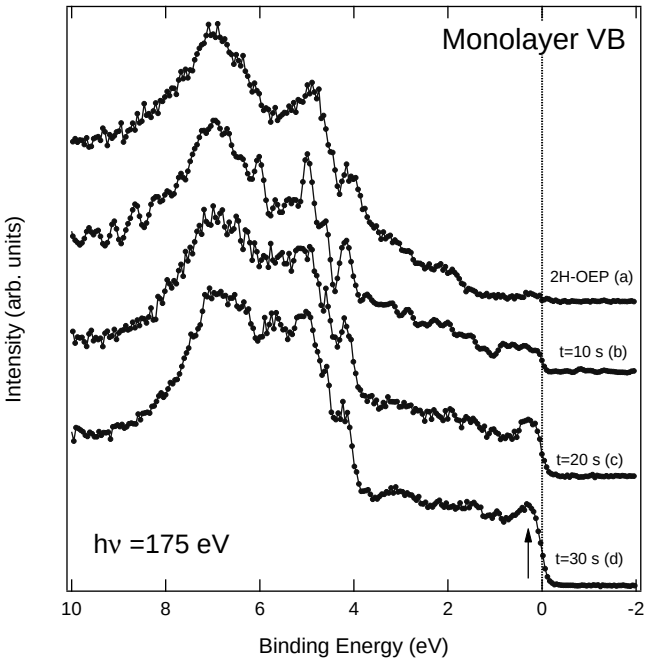

Figure 6.8: Valence Band structure of 2H-OEP ML during Fe metalation. The sequence of the ML valence band spectra are raw data subtracted by the valence band of the clean Ag surface taken in the same conditions. The used photon energy was hν = 175 eV.

Finally, the multilayer valence band taken during the metalation are displayed in Figure 6.9. Following the same procedure as in the TPP case, in bottom panel of Figure 6.9 the reported valence band has been obtained by subtracting the spectrum of the 2H-TPP multilayer to the valence band after each evaporation step, in order to highlight the molecular changes during the Fe atoms coordination. The major changes are confined below 7 eV, with an evident clear growth of states near the Fermi level and an apparent metallic behaviour.

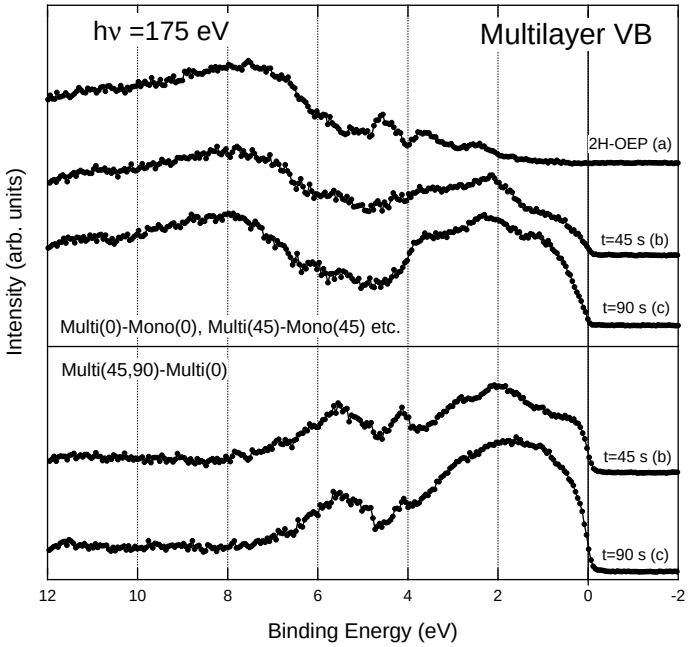

Figure 6.9: Valence Band structure of 2H-OEP multilayer during Fe metalation. The reported valence band has been obtained (top panel) by subtracting the spectrum of the 2H-OEP multilayer to the valence band after each evaporation step, (bottom panel) by subtracting from each multilayer spectrum the valence band of the corresponding intermediate step taken on the monolayer. The used photon energy was hν = 175 eV.

However, considering that we have only four layer, a relevant contribution from monolayer is expected in these spectra. Therefore, in order to disclose the overlayer molecular features, in the top panel of Figure 6.9 we have subtracted from each spectrum the valence band raw data of the corresponding intermediate step taken on the monolayer, so that also the contribution from Ag valence band is removed. This method is quite rough, yet we notice that the valence valence band of the 2H-OEP obtained in this way almost completely matches the valence band of the 2H-OEP molecules in gas phase, as observed in Figure 6.10. This is expected from porphyrin molecules, which

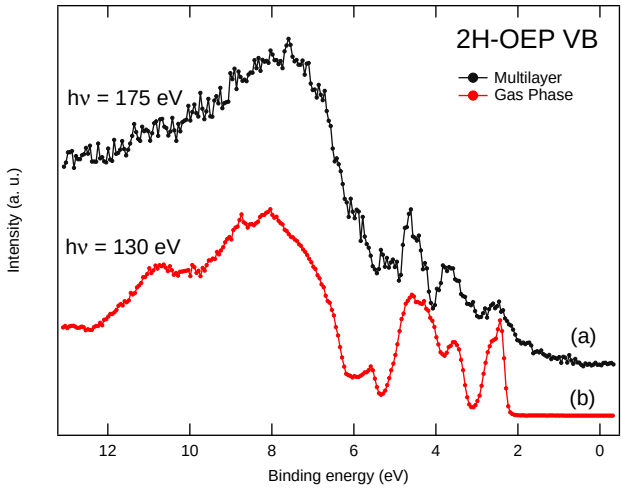

Figure 6.10: Valence Band structure of 2H-OEP multilayer (a) collected with photon energy hν = 175 eV. This spectra is the raw data subtracted by the valence band of the 2H-OEP monolayer taken in the same experimental conditions. Valence Band structure of 2H-OEP molecules in gas phase (b), collected with photon energy hν = 130 eV.

are known to hardly interact in multilayer systems (see, e.g., Chapter 3 and Chapter 4) and confirms the reliability of the method applied for obtained the OEP overlayer valence band.

In Figure 6.9 (top panel), we notice that, as in case of TPP, the layers above the first are non-metallic with a density of states that goes almost linearly to zero at the Fermi level. Therefore, the intensity at the Fermi level seen in multilayer valence band is instead due to the metallization of the monolayer. From the comparison between the spectra of Figure 6.8 and those of Figure 6.9, we conclude that that the charge injection from the substrate is confined to the first monolayer.

6.4 Conclusions

In-situ Fe atoms coordination with Octaethylporphyrin molecules has been successfully reproduced in UHV on Ag(111), following the same procuedure as for Tetraphenylporphyrins Chapter 5. The employment of synchrtron-radiation-based techniques allowed to determine the subsequent Fe coordination steps for the monolayer and multilayer cases.

The study of the 2H-OEP molecules adsorbed on Ag(111) showed a metallic behaviour for the monolayer, both before and after the Fe coordination. In fact:

- the HOMO band of 2H-OEP crosses the Fermi edge and increases its

intensity as the iron goes into the macrocycle;

- the comparison between the XPS N 1*s* binding energy (with respect to the Fermi level) and the correspondent NEXAFS excitation energies evidences a complete screening of the XPS core hole, before and after Fe evaporation;

- the XPS fitting functions have required the introduction of an asymmetry parameter (singularity index) that increases as the metalation of molecules proceeds.

Both core level and valence band photoemission results from the multilayer case have given evidence that the charge injection from the substrate is more likely confined to the first layer. The metallic state of the first layer evolves with Fe complexation, probably due to Fe *d*-states hybridization with the *sp*-bands of the substrate. These results highlights that, under equivalent experimental conditions, Fe metalation is accomplished in both 2H-TPP and 2H-OEP deposited on Ag(111) with comparable characteristics.

Whereas flat conformation of the macrocycle is found for 2H-TPP monolayers on Ag(111), the 2H-OEP molecular plane in monolayers is observed to be tilted with respect the surface plane to optimize steric hindrance caused by ethyl groups. Since a similar configuration is predicted in 2H-OEP monolayer simulations, indipendenlty from the presence of a substrate [125], the fundamental role of lateral groups in molecular packing is evidenced. The addition of a central atom such as Fe scarcely affects the molecule orientation, as confirmed also by data of CoOEP monolayer on Ag(111) [125], althogh, at this level of analysis, a distortion of the macrocyle cannot be excluded. Finally, while in 2H-TPP the presence of additional layers inflences only the rotation angle of the lateral phenyl groups, in 2H-OEP multilayer the macrocycles occur to be further tilted with respect the surface plane, along with possible chemical modification of the iminic groups.

Chapter 7

Eumelanin thin films on ITO: chemical disorder in basic model-tetramers

7.1 Introduction

The physical and chemical properties of eumelanins are defined by their macromolecular structure but, despite many scientific efforts, a complete model of eumelanin aggregation behaviour has not been assessed yet. Eumelanin is known to originate from the oxidative copolymerization of 5,6-dihydroxyindole (DHI) and 5,6-dihydroxyindole-2-carboxylic acid (DHICA) [93]. Their oxidative forms - dihydroxyindole (HQ), quinone-imine (QI) and indolequinone (IQ) - are also included in the system [94], but it remains unclear how these monomeric units are connected together to form a secondary structure (all the monomers included in eumelanin compound are sketched in Figure 1.4).

Lately, a stacked oligomer model has been proposed to describe ultrastructural organization of eumelanin [16]. According to this model, the agglomeration of eumelanin is a hierarchical self-assembly process with planar protomolecules aggregating into larger structures that finally form the morphology of the macroscopic pigment. The identification of the chemical structure of protomolecule is therefore the starting point for the construction of consistent structure-property-function relationships, but the details of the connectivity of the basic monomers in protomolecules remain one of the major questions.

The absence of a detailed chemical characterization is mainly due to intractability of eumelanin from the analytical perspective, since it is chemi-

cally and photochemically very stable and virtually insoluble in most common solvents. Besides, the practical difficulty in manipulation has long constituted a deterrent from incorporating melanin in electronic and optoelectronic devices.

Very recently, it has been shown that synthetic eumelanin aggregates obtained by dispersion of powders in water droplets deposited onto copper substrates are amenable to soft X-ray spectroscopy measurements of electronic properties [101]. However, owing to eumelanin insolubility in water, these films are far from being continuous and homogeneous and they have been proved to crack and deteriorate over a couple of months after the preparation.

In this chapter, the experimental and theoretical investigation of polymerization effects on the electronic properties of high quality eumelanin thin films is reported. The first goal of this study is the production of continuous thin films suitable for a detailed spectroscopic characterization in UHV conditions. The films have been prepared by drop casting from a solution of melanin powder aggregates in dimethyl sulfoxide (DMSO) and can be regarded as reference samples for the study of eumelanin in condensed phase. Indeed, they resulted to be homogeneous, flat on a nanometric scale, and virtually free from contamination arising from the solvent (mainly sulphur from DMSO).

The electronic structure of eumelanin thin films has been investigated by means of X-ray absorption and photoemission spectroscopies. The experimental data have been compared to *ab initio* density-functional calculations of the occupied and unoccupied electronic states of the isolated monomers participating to the eumelanin macromolecule. However, the way the single monomers are brought together to form macromolecules is a fundamental issue to clarify, since polymerization may have important consequences on the electronic properties. In order to single out the polymerization effects, we followed a bottom-up scaling approach to establish the minimum supramolecular level of organization that can provide a consistent spectroscopical picture of an altogether complex and highly disordered system. This evaluation is rather important because, owing to the inherent heterogeneity in the natural material and the difficulties associated with chemical analysis of the full macromolecular system, the $bottom-up$ molecular approach may be the way to reach a final assessment of the melanin electronic properties.

In the present chapter, a tetramer macro-cycle, made by three hydroquinones and one indolequinone, is found to reproduce the observed polymerization effects at the N K-edge, while preserving the experimental spectral weight among the different monomers. This tetramer is different from that predicted for the synthesis from isolated monomers, providing an experimen-

tal evidence of the role of the reaction path on the stabilization of macrocycles in condensed phase eumelanin.

7.2 Experimental and computational details

Commercially available melanin powders (Sigma-Aldrich, cat. no. M8631), prepared by oxidation of tyrosine with hydrogen peroxide, have been used for the experiment. Film growth was primarily monitored by Atomic Force Microscopy (AFM) operating in tapping mode (TM) in ambient conditions.

Atomic Force Microscopy (AFM) imaging showed that eumelanin dissolved in DMSO and deposited by drop casting on indium tin oxide (ITO) covered glass substrates provided quite homogeneous films that did not display charging effects upon photoionization, with a thickness of about 80-100 nm. In Figure 7.2 a selected 20×20 μm^2 image of eumelanin film is displayed. For this purpose, a Solver PRO-M microscope (NT-MDT Co., Zelenograd, Russia) was used with ìMasch silicon cantilever (triangular tip, 330 KHz, 48 N/m - MikroMasch, Estonia). The images was collected at 256 x 256 pixel resolution at a scan rate of 1 Hz. The image was both flattened (zeroth order) and square-fit (second order) with the Gwyddion 2.18 software package [151], developed for the analysis of SPM images. From Figure 7.2 is evident that the film is continuous, with (about 0.44 nm RMS). It is worth noting that the RMS roughness of the clean ITO surface is larger (about 3 nm on a 10×10 μm^2 image). These films have therefore been selected for the spectroscopy experiments.

Raman spectroscopy was also used to estimate the relative content of basic monomers in our films, as was done for aggregates deposited onto Cu substrates [101]. In Raman spectroscopy, monochromatic light, usually from a laser in the visible, near infrared, or near ultraviolet range interacts with vibrational, rotational, and other low-frequency modes in a system, resulting in the energy of the laser photons being shifted up or down [166]. The shift in energy gives information about the phonon modes in the system, provideing specific information on the identification of analytes, characterization of sample matrices, and molecular spectroscopic information useful in the structural elucidation of unknowns [167]. The experimental spectrum has been obtained by exciting the sample with a He-Ne laser ($\lambda = 632.8$ nm) and by measuring the scattered light with a LABRAM spectrometer coupled with a confocal microscope. The experimental spectrum is finally compared with that obtained from a weighted mix of the three monomers Raman spectra. The fitting was carried out by minimizing the root-mean-square (rms) difference between the measured spectrum and the weighted mix. The fit-

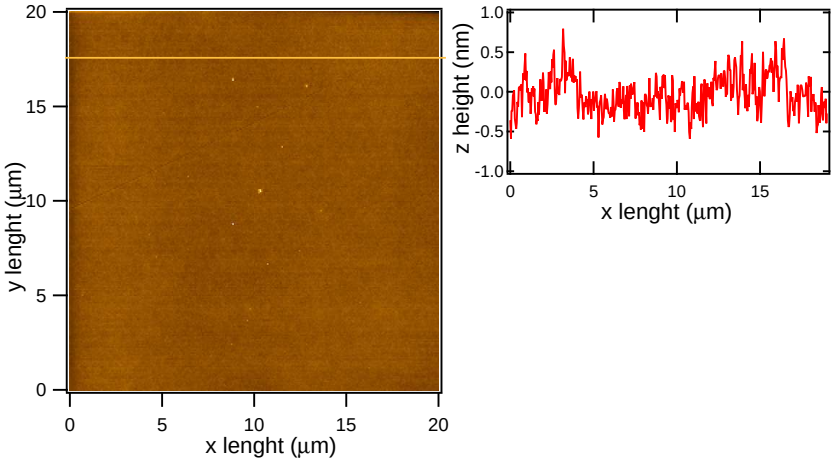

Figure 7.1: Tapping-mode AFM images (20x20 μm^2) of eumelanin films on ITO (left). The maximum height Z is 4 nm. Image line profile (right) taken at along the horizontal line in the height image. Note that the z height scale differs at least of four orders of magnitude from the x lenght scale.

ting parameters were the weights of the single monomer contributions. The monomer Raman spectra have been drawn according to the computational results of Powell *et al.* [98].

The Near Edge X-ray Absorption Fine Structure (NEXAFS) and soft X-ray Photoemission Spectroscopy spectra have been measured at the ALOISA beamline of the ELETTRA synchrotron light source in Trieste (Italy), whereas sample preparation and characterization was carried out at the Surface Science and Spectroscopy Lab of the Catholic University (Brescia, Italy).

Calculations have been performed within the collaboration with Ralph Gebauer and Prasenjit Ghosh from The Abdus Salam International Centre for Theoretical Physics (ICTP) in Trieste (Italy). The geometry and electronic properties of the monomers and the oligomers in the gas phase have been studied using the *ab initio* DFT based Quantum-Espresso package [168]. The monomers (cubic box of side 13.75 Å), the IH dimer (box dimensions 13.75 x 19.26 x 13.75 Å) and the IHHH and QIQI tetramers (box dimensions 19.26 x 19.26 x 13.75 Å) were placed in large boxes to ensure negligible interactions between the periodic images. For all the cases the molecules lie in the xy-plane (Figure 7.2). Brillouin zone integrations have been performed using Γ point only. We have used the PBE [153] form of generalized gradient approximation for the exchange-correlation energies. Ground state geometries and electronic structure of the monomers and oligomers have been calculated using ultrasoft pseudo-potentials (UPP) [169] and cut offs of 25 Ry and 300

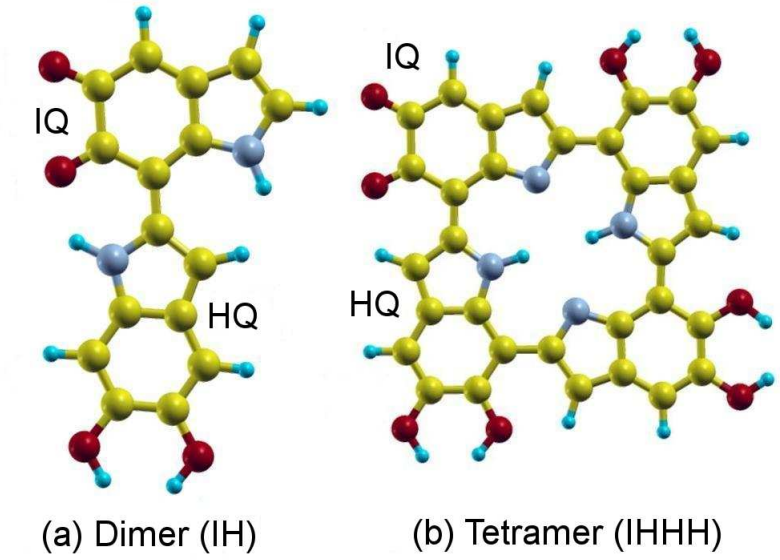

Figure 7.2: Model protomolecules for eumelanin: (a) a dimer composed of IQ-HQ (IH) and (b) IQ-HQ-HQ-HQ (IHHH) tetramer (gold = C, red = O, grey = N and light blue = H).

Ry for the plane-wave basis set and the augmentation charge introduced by UPP respectively.

Within the dipole approximation, the spectral intensity $I(\epsilon)$ of the X-ray absorption spectra is given by:

$$I(\epsilon) \propto \sum_{f} |\langle \psi_{1s} | \mathbf{r} | \psi_f \rangle|^2 \delta(\epsilon_f - \epsilon_{1s} - \epsilon) \tag{7.1}$$

where $\mathbf{r}$ is the position operator, ϵ is the energy of the incident X-ray, ϵ_f and ψ_f are the Kohn Sham (KS) eigenvalue [170] and eigenfunction respectively of the f^{th} conduction band of the excited molecule respectively, ϵ_{1s} and ψ_{1s} are the energy eigenvalue and the energy eigenfunction of the $1s$ level of the element whose NEXAFS spectra is to be calculated. The summation f extends to all the energy levels above the HOMO of the molecule. The KS eigenvalues have been convoluted by a Gaussian of width 0.24 eV.

Since we are using pseudopotential based DFT, in which the core electrons and the strong nuclear potential have been replaced with a pseudopotential, we do not have information regarding the ψ_{1s} orbital of the atom whose spectra we are interested in calculating, when it forms a molecule through interaction with other atoms. However, based on the assumption that the core orbitals are relatively unaffected by differences in the chemi-

cal surroundings of the atoms, the ψ_{1s} orbital can be obtained from an all electron calculation of the atom and can be used in evaluating the transition matrix elements. While there are more sophisticated approaches for obtaining the ψ_{1s} orbital [171, 172], this approach yields results which are in reasonably good agreement with the experiments.

The electron excitation can be modelled by the Slater's transition state theory [173, 174], where half an electron can be promoted from a core state to the excited state. The difference between the final and initial values correspond to the excitation energies [175]. The excitation energies can also be evaluated by calculating the differences in total energy in which a whole electron is promoted from a core state to an excited state and the system is still in the ground state. This is also called the ΔSCF approach. However, for both the above mentioned approaches, it is necessary to do a DFT calculation for each individual excited state, thus making the procedures computationally demanding. A less expensive alternative is to calculate the virtual orbitals of the system in the presence of a half core hole (HCH) or a full core hole (FCH) on the absorbing nucleus. The excited electron is usually removed from the system [176, 177, 178]. Since previous calculations suggests that for molecules and clusters the HCH technique provides a better agreement with experiment, while for condensed phase the FCH is a better approximation [179, 176, 177, 178, 180, 181, 182, 183], we use the HCH technique in order to calculate the NEXAFS. It should be noted that due to the presence of the core hole in the pseudopotential of the excited atom, such calculations model the relaxation of the valence electrons following the excitation.

We have performed spectral calculations for C and N. For the excited atoms, we have used Troullier-Martin type norm-conserving pseudopotential with a wave function cut off of 70 Ry. The pseudopotentials have been generated using the atomic code which is also a part of the Quantum-Espresso package. We have used electronic configurations of $1s^{1.5}2s^22p^2$ and $1s^{1.5}2s^22p^3$, and cut off radius of 1.20 and 1.23 a.u. (for $l = 0$ and $l = 1$, where the later channel is local) for C and N respectively. In such pseudopotential-based calculations the energy of the core states is not directly available. Therefore absolute excitation energies are not computed. Our calculations provide relative excitation energies, and throughout the paper we shift the excitation energies by an arbitrary constant for better visual comparison with experiment. The computed spectra of different molecules are aligned with respect to each other using the vacuum level as a reference.

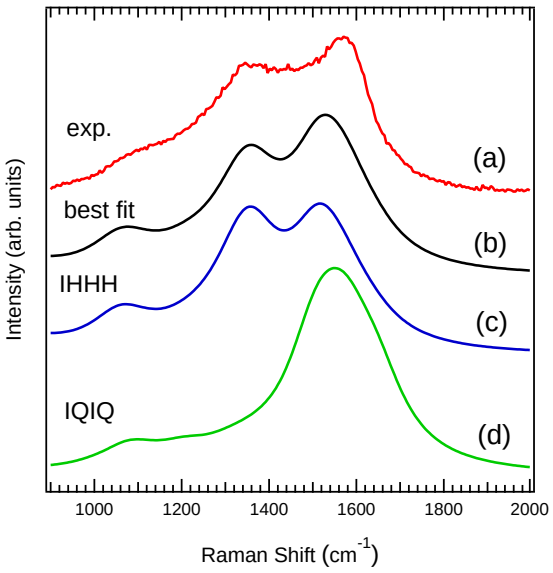

Figure 7.3: Measured Raman spectrum of the melanin thin films on ITO (a) compared with the best fit based on a linear combination of monomers (b) and with the calculated spectra of IHHH (c) and QIQI (d).

7.3 Results and discussion

7.3.1 Raman and optical spectroscopies

In agreement with previous results [101], experimental Raman measurements (Figure 7.3-a) indicate that the eumelanin spectrum does not depend on the sample preparation, but can be superposed to that of precursor powders. Furthermore, the Raman spectrum does not change with time over at least one year after the first measurements, and virtually identical spectra have been collected from different batches purchased over the years. This is assumed as a proof of the sample stability and therefore of the reproducibility of the experimental conditions. The best fit in Figure 7.3-b is obtained through a linear combination of the HQ monomer (about 70%) and of the IQ monomer (about 30%), while QI is virtually absent.

The wavelength dependent optical density (OD) spectrum in the UV-VIS range data is shown in Figure 7.4. The OD is define as the product of the absorption coefficient α and the film thickness x, and has been obtained from the Lambert-Beer law $T = \exp -OD$, where T is the transmittance I/I_0 of the eumelanin film. In the inset of Figure 7.4 the square root of the OD has been fit with a straight line in order to estimate the band gap, as is usually done in amorphous semiconductors [184]. From the fit, an energy gap of

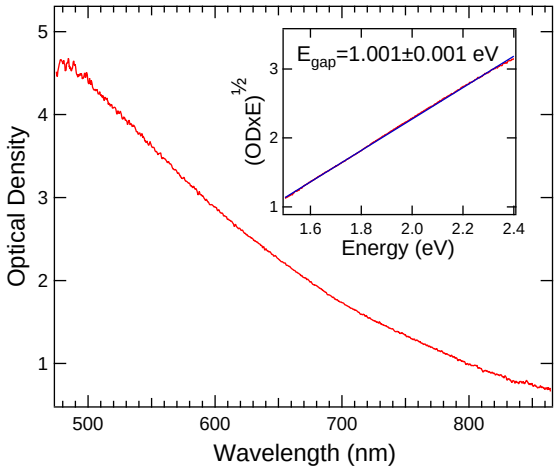

Figure 7.4: Absorption spectrum of eumelanin deposited on a ITO in the visible range. In order to estimate the band gap, the $OD^{1/2}$ has been fit with a straight line.

about 1 eV has been evaluated for the present samples.

7.3.2 Photoemission spectroscopy and density of states

Figure 7.5 shows the valence band photoemission spectrum obtained with $h\nu = 281.6$ eV photons from the synchrotron (a), as well as with an Al K-α X-ray source, i.e. $h\nu = 1486.6$ eV (b). Unlike the featureless UV-VIS optical spectrum (Figure 7.4) typical of melanin samples (see, e.g., [77]), the features observed in the valence band photoemission spectrum are still well separated from one another, enabling an effective comparison with theoretical calculations. In Figure 7.5-a,b several spectral features, labelled as V_A to V_F, can be singled out, indicating that the molecular character of the electronic states is preserved in the solid state.

First of all, it should be observed that the linewidth of all experimental bands does not change with the experimental resolution, which is about 150 meV for synchrotron radiation and about 1 eV for the Al K-α source. This suggests that the band width is an intrinsic effect of the thin films, very likely due to polymerization effects. On the basis of a previous comparison with the calculated DOS of HQ (the prevalent monomer) through a projection on several orbitals [101], the overall energy range can be divided into three regions, separated by vertical dashed lines in Figure 7.5. The first ranges from BE = 0 eV to BE = 10 eV and is characterized by a relevant contribution from carbon π orbitals, that is not found elsewhere in the calculated spectrum. The second region ranges from 10 to 20 eV, with a relevant contribution from carbon σ orbitals. Finally, the third region ranges from 20 to 30 eV,

with a prevalent contribution from carbon, nitrogen and oxygen shallow core levels. The calculated HQ DOS (Figure 7.5-f) catches the main experimental features in the valence band region. The IQ DOS (Figure 7.5-g) also seems to agree with the experimental data with a worse agreement with respect to HQ in the shallow core level region (i.e. below experimental peak E).

As a first exploration of the polymerization effects, we have considered the tetramers resulting from an IQ-HQ-HQ-HQ (IHHH) (Figure 7.2-b) and QI-IQ-QI-IQ (QIQI), both of which have an inner porphyrin-like ring according to the model proposed by Kaxiras *et al.* [95]. It is important to observe that in IHHH the IQ:HQ ratio (25:75) is quite close to that estimated from Raman data (30:70), indicating that IHHH tetramer could be regarded as the most abundant and stable aggregation form of eumelanin in the present samples, prepared by oxidation of tyrosine with hydrogen peroxide. Actually the calculated Raman spectrum for IHHH (Figure 7.3 -c) is quite similar to that obtained from the best fit (Figure 7.3-b). On the other side, the Raman spectrum calculated on the basis of the relative weight of monomers in QIQI (Figure 7.3-d) is quite far from the experimental data, and therefore exclude significant contributions from QIQI macro-cycles in the present samples.

However, according to Kaxiras *et al.*, IHHH has the largest negative formation energy[1], while QIQI has the largest positive formation energy. Their results suggests that, at least in gas phase, formation of QIQI is more probable than IHHH. Our calculations of the formation energy of IHHH and QIQI yield values of -3.44 eV and 0.81 eV respectively. Although the results agree qualitatively with those of Ref. [95], the differences in the absolute values of formation energies may be due to the use of different types of exchange correlation functionals and pseudopotentials.

Since the composition of the films obtained from Raman measurements indicate the presence of IHHH, while a comparison of the relative energies of IHHH and QIQI (calculations neglect the effect of the chemical environment during the formation process) favors the presence of the latter, it seems that during the synthesis in the condensed phase of the present melanin samples, the reaction path stabilizes the IHHH tetramer. In fact, we have to considere that the the actual synthesis process (of both synthetic and natural eumelanin) proceeds in a solution and not in a isolated enviroment that would be experimentally achievable only if isolated and completely formed monomers react, e.g., UHV conditions. Indeed, the presence of intermediate

[1]the formation energy of the teramer is defined as the difference between the ground state energy of the equilibrium configuration of the four isolated constituents monomers and the ground state energy of the equilibrium configuration of the polymerized tetramer. Therefore, a positive formation energy means a most stable configuration of the tetramer with respect to the isolated four constituent monomers.

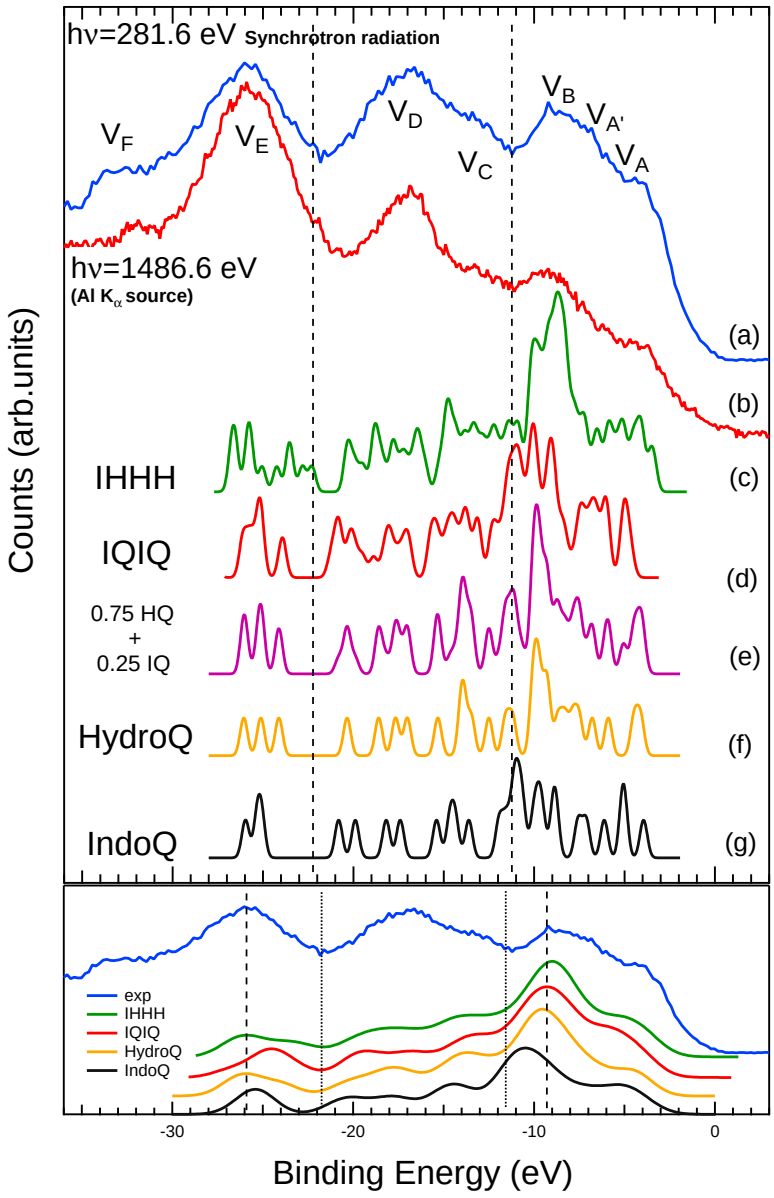

Figure 7.5: Top panel: Photoemission spectra of synthetic eumelanin collected by exciting the sample with hν = 281.6 eV (a) and hν = 1486.6 eV (b) photon energies. The main bands are labelled from V_A to V_F. Calculated density of states of the tetramers IHHH (c) and QIQI (d), of a weighted mix of IQ and HQ (e), and of the monomers HQ (f) and IQ (g). Bottom panel: calculated spectra convoluted with a gaussian function (FWHM = 1.0 eV).

reactive products derived from amino acids (tyrosine) and the contribution of redox agents to the actual synthesis are likely to alter the reaction path considered in calculations.

To test the reliability of these model protomolecules we have done calculations for the occupied DOS and the C 1s and N 1s NEXAFS, the results of which are presented in the following, for both IHHH and QIQI.

Another important issue regarding the geometry of tetramers is the H termination of the N atoms inside the ring. For IHHH we considered two cases: (a) in which the all the N atoms are terminated with H (IHHH*) and (b) in which only two of the N atoms are H terminated (IHHH). In fact, despite IQ and HQ monomers have N atoms bonded intrinsically to H atoms, it is not unlikely that the complex reactions occurring during synthesis lead to de-hydogenation of the single monomers. On the other hand, Kaxiras calculations [95] neglect this possibility, favouring the presence of QI monomers (N atoms are not bonded to H) in the final protomolecules. We find that (b) is energetically more favorable than (a) which has a formation energy of -4.88 eV. This is not unexpected considering that the presence of four hydrogens in the center of the macrocycle results in a large unstability due to steric repulsions. In fact, in porphyrins, whose molecular structure is well-known and experimentally demonstrated, there are only two hydrogens attached to N atoms in the macrocycle ring (see Figure 1.1).

When examining the DOS of the IHHH and QIQI tetramers (Figure 7.5-c and d), the agreement with experimental data is better than the case of isolated monomers. In particular, in the region below peak V_A a broad band is found for IHHH DOS and likewise, also the contribution in the shallow core level region is now spread in a larger BE range. In order to show the extent of polymerization effects in the IHHH tetramer, the IHHH DOS is compared to that of a linear combination of HQ and IQ (Figure 7.5-e), accounting the same ratio as in the IHHH tetramer. It is clear that a linear combination still retains a monomer-like structure and the electronic states in the different specific regions are not as much spread as in the case of tetramer. Moreover among the two tetramers, the DOS of IHHH is in better agreement with the experimental one, suggesting the presence of IHHH than QIQI in the sample. This is also clear when the calculated spectra are convoluted with a gaussian function (FWHM = 1.0 eV), as shown in the bottom panel of Figure 7.5. Although the calculated spectra show a similar sequence of main features, the fitting to the experimental data evidences differences on the intensity and energy of the main spectral features, which make the theoretical spectrum of the IHHH tetramer the closer to the experimental data, while the worse agreement is given by the isolated IQ monomer.

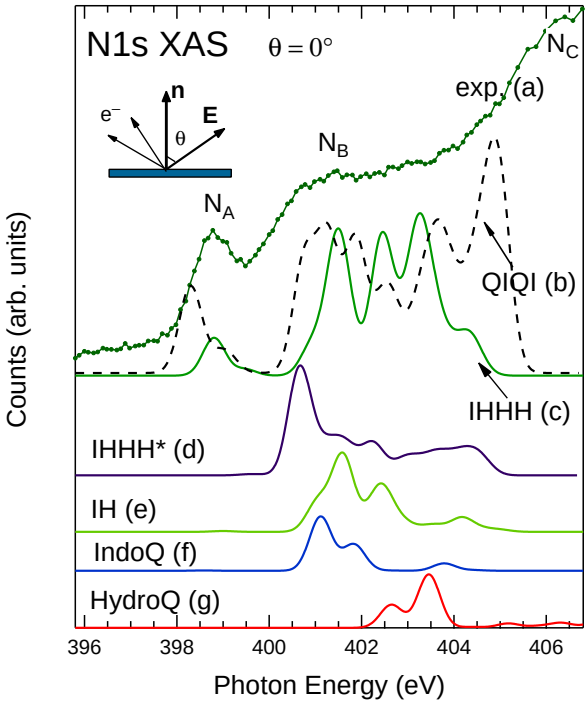

Figure 7.6: (Experimental N 1*s* NEXAFS spectrum (a); calculated NEXAFS spectra of the QIQI (b) and IHHH tetramers (c), the IHHH tetramer with 4 hydrogens in the ring (IHHH*,d), the dimer IH (e), the monomer IQ (f) and the monomer HQ (g). The experimental spectrum has been collected across C K-edge at nearly grazing photon incidence with linear polarization of light perpendicular to the thin film surface ($\theta = 0°$).

7.3.3 NEXAFS study

A distinct evidence of polymerization effects is obtained by analyzing the N 1*s* NEXAFS spectrum. The analysis of this spectrum does not require a deconvolution of the spectral weight on different atoms as in the case of C, as each monomer contains one single N atom. The experimental data are dominated by the two features N_A and N_B respectively at 398.7 and 400.7 eV (Figure 7.6-a), which have a clear counterpart in the calculated NEXAFS spectrum of QIQI and IHHH (Figure 7.6-b and c respectively). While the first feature results from transitions to the LUMO of the tetramers, the second feature is due to several transitions to other unoccupied states higher in energy.

It is quite interesting to observe that the peak at 398.7 eV does not appear in the calculated NEXAFS of the monomers (Figure 7.6-e and -f), the dimer (Figure 7.6-c) and in IHHH*. This indicates that: (i) presence of the N_A peak can be reproduced in the calculated NEXAFS spectrum provided that

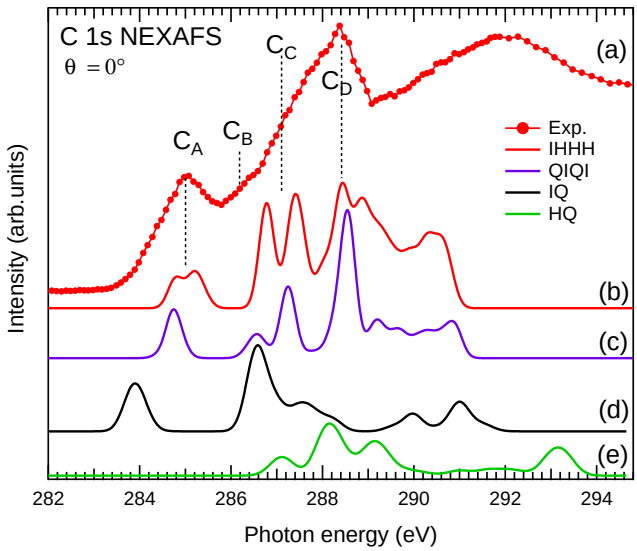

Figure 7.7: C 1*s* NEXAFS spectrum (a) compared with the calculated NEXAFS spectra of the IHHH (b) and QIQI tetramers (c), the monomer IQ (d) and the monomer HQ (e). The experimental conditions are those specified for Figure 7.6

polymerization has occurred in eumelanin and (ii) presence of more H atoms in the ring makes the tetramer unstable due to steric repulsions.

Finally we consider the C 1*s* NEXAFS spectrum (Figure 7.7). As already observed, the experimental C 1*s* NEXAFS spectrum has a sharp peak C_A at 285.2 eV followed by three features C_B, C_C and C_D detected at higher photon energies. This spectrum has been compared with the ones computed for the monomers and tetramers (Figure 7.7b-e). The calculated spectra of HQ is in worse agreement with the experimental one, with the first peak missing. Though the spectra for IQ has features similar to the experimental one, the relative positions of the peaks are quite different from the measured spectra. For both the tetramers, the calculated spectra are in good agreement with the experimental data. C_A results due to transitions to the π^*-like LUMO and LUMO+1 as is usually found in hydrocarbon rings [47], while in the region at higher photon energies there is significant contribution from σ^* states.

7.4 Conclusions

In conclusion, by using soft X-ray spectroscopies, we have been able to probe the density of states of both occupied and unoccupied electronic levels of

eumelanin in the condensed phase. A good agreement with the experimental data is found with the calculated DOS of the HQ monomer, but a better agreement is found when the IHHH tetramer with two N atoms terminated with H atoms is considered. This shows to which extent the calculated electronic structure of single monomers catches the main features of solid state aggregates. Due to polymerization, the local environment of the N atoms differs completely from that of the individual monomers (suggested by absence of the first feature in the N 1s NEXAFS of the monomers). Moreover the Raman spectroscopy measurements and a comparison between the experimental and the calculated NEXAFS spectra suggest that during the synthesis of condensed phase eumelanin from the oxidation of tyrosine, the IHHH tetramer is stabilized, unlike the calculations on synthesis from gas phase where the QIQI tetramer resulted to be the more stable [95], indicating that the exploration of the more stable forms of eumelanin protomolecules cannot be carried out without considering the environmental conditions of the melanin synthesis processes.

Chapter 8

Nanostructured K-doped eumelanin layers: morphology, structural and electronic properties

8.1 Introduction

In eumelanins, the high affinity for metal ions is one of the most characteristic features of this pigment (for a complete review, see Ref. [105]). Natural eumelanin normally contains Mg(II), Ca(II), Na(I), K(I) and almost all the first row transition metals, enabling storage, release, and exchange in human body. Beacuse the high content of metal ions in the natural pigment, one requisite point is to establish the effect of metal binding on the eumelanin electronic and structural properties.

Since melanogenesis occurs in a saline enviroment, it is not possible to examine sistematically how metal cations affect melanin aggregation. However, Liu and Simon [108] observed that, after treatment with ethylenediaminetetraacetic acid (EDTA, which extracts di- and multivalent metal cations), the size of eumelanin granules measuring 150 nm in diameter (i.e., the **(iv)** level of aggregation according to the hierarchical self-assembly model described in Chapter 1.2.2 [16]) gradually decreases. For synthetic eumelanin, cations may be introduced during the deposition process. As pointed out in Chapter 1.2.3, synthetic eumelanin is likely to be composed by the same oligomeric entity as natural eumelanin [13, 17, 18, 19], but, on a microscopic scale, it occurs as an amorphous conglomerate and no regular shaped elements can be singled out [20]. Incidentally, in Fe-doped thin films grown by

electrodeposition round-shaped particles measuring about 100 nm in diameter appear [109], but it is not clear if this behaviour is due to the presence of cations or to the deposition technique employed, because comparison with other deposition techniques is not reported. Concerning the electronic structure, eumelanin containing metal ions has not been explored with soft X-ray electron spectroscopies yet.

In this chapter, potassium is chosen as a dopant element for investigating the effects on the morphological, structural and electronic properties of eumelanin thin films. The study is divided in two parts. In the first part the role of K in the growth of melanin thin films is explored. Two kind of substrates for the growth have been selected: gold thin films evaporated on mica or indium tin oxide (ITO) films deposited on glass. Both substrates were chosen to be conductive, which is an important feature in view of possible device applications of eumelanin thin films, such as organic electronic devices. Furthermore two deposition techniques have been considered: electrodeposition or drop-casting of eumelanin powders dispersed in DMSO. This choice is motivated by the fact that other techniques such as thermal evaporation or sputtering may affect the chemical integrity of the eumelanin monomers. Besides, electrodeposition is a technique that allows a good control on the film growth in the perspective of technological applications. Finally, K was added to the eumelanin-DMSO solution as KBr. Salt addition was specifically required for electrodeposition, but it can be used also in the drop-casting to dope eumelanin with K. On the basis of the analysis carried out in the fist part, among the samples doped with K we resorted to consider the sample obtained by electrodeposition on gold for the study of structural and electronic properties. Based on this choice, in the second part of our study we are able to probe the effects of K doping on structural propertiesof the thin films, with particular emphasis on possible self-assembling effects. Finally, a preliminary analysis on the influence of K ions on electronic properties is presented, focussing on the electronic states close to the HOMO energy region.

8.2 Experimental section

Commercially available eumelanin powders (Sigma-Aldrich, cat. no. M8631), prepared by oxidation of tyrosine with hydrogen peroxide, have been used for the experiment. Eumelanin samples were prepared on indium tin oxide (ITO) covered glass substrates (Sigma-Aldrich, cat. no. 576352, surface resistivity 100 Ω/sq) or on substrates of gold thin layers evaporated on mica substrates. To produce the latter, approx. 200 nm of gold were evaporated

onto freshly cleaved mica in a UHV chamber with a base pressure of $5x10^{-7}$ mbar, following the process described in [185] and [186]. Prior to use, the gold substrates were flame annealed by sweeping a concentrated hydrogen flame over the gold surface at a distance of 2-3 cm.

Table 8.1 summarizes the main features of the four samples under consideration in the present study. For each sample, the eumelanin solution concentration was always the same, i.e. 10 mg/ml. Sample A was produced by drop-casting 10 μl of a solution of eumelanin in DMSO (purity 99.6%, Sigma Aldrich CAS 67-65-5) on 0.4 cm^2 ITO substrates. This was left to dry at room temperature in a preferably unperturbed environment. Potassium doping was achieved by resorting to an electrodeposition technique, where KBr (purity 99%, Carlo Erba CAS 7758-02-3) was added as an electrolyte to a solution of eumelanin in DMSO. Electrodeposited eumelanin films were grown by electrochemical self-assembly on a gold substrate (sample B) or on ITO covered glass substrate (sample C); this method consists of the immersion of the gold or ITO substrates in a synthetic melanin-containing DMSO solution. Due to its solubility in DMSO, potassium bromide (KBr) was found to yield a sufficient conductivity to the solution. In particular, through vigorous stirring and up to twenty minutes of sonication in an ultrasonic bath, 0.2 M of KBr was dissolved in DMSO. The Au or ITO electrodes were polarized in a conventional two-electrode cell for 1 hour at $-$ 1.0 V in the working solution to grow melanin films. A sheet of graphite with a thickness of 0.5 mm was used as counter electrode. The current was constantly controlled during the deposition process. The initial current quickly decreased to a constant value indicating that once a first layer of melanin had formed on the gold film, the resistance of the system was virtually determined by this first layer. After a few minutes, the current approached a final value and remained stable. Experiments with different gold or ITO surface areas produced different absolute currents but remarkably reproducible current densities of 0.049 ± 0.003 A/mm^2 for gold and 0.039 ± 0.003 A/mm^2 for ITO. We do not exclude that different, though comparable, current densities can affect to some degree the sample morphological properties. However, the conclusions we will draw by comparing the two electrodeposited samples are not dependent on this detail.

The melanin-covered Au and ITO electrodes were then removed from the cell, carefully rinsed in milliQ purified water, then cleaned in ethanol and finally dried under a nitrogen flux. In both samples, the electrodeposited film covers a surface of about 0.5 cm^2. Finally, sample D was obtained by drop-casting 10 μl of the same solution used for sample B and C on ITO substrates.

Film growth was primarily monitored by Atomic Force Microscopy (AFM)

operating in tapping mode (TM) in ambient conditions. For this purpose, a Solver PRO-M microscope (NT-MDT Co., Zelenograd, Russia) was used with ìMasch silicon cantilever (triangular tip, 330 KHz, 48 N/m - MikroMasch, Estonia). Images were collected at 512 × 512 pixel resolution at a scan rate of 1 Hz. Images were either flattened (zeroth order) and/or were square-fit (second order) with the Gwyddion 2.18 software package [151], developed for the analysis of SPM images. X-ray Diffraction measurements were carried out at the W.1.1 beamline at the HASYLAB Synchrotron Facility in Hamburg, Germany. The Near Edge X-ray Absorption Fine Spectroscopy (NEXAFS) and soft X-ray Photoemission Spectroscopy (XPS) spectra have been measured at the ALOISA beamline of the Elettra synchrotron in Trieste (Italy). NEXAFS spectra were taken in partial electron yield mode by means of a channeltron detector and the energy resolution was better than 100 meV. Polarization (linear) dependent NEXAFS spectra have been collected keeping the grazing angle fixed at 6° with respect to the surface sample [49]. NEXAFS spectra measured at the C and N K-edges have been calibrated with a precision of 0.01 eV by simultaneous acquisition of the $1s \rightarrow \pi^2$ gas phase transitions of CO and N_2 at $h\nu = 287.40$ and $h\nu = 401.10$ eV, respectively. The XPS overall energy resolution was set at 300 meV. The XPS spectra binding energies (BE) of sample B and sample A were calibrated against the Au $4f_{7/2}$ signal (BE = 84.0 eV [187]) and the In $3d_{5/2}$ signal (BE = 445.2 eV), respectively.

Before photoemission and NEXAFS measurements all the samples were annealed in vacuum systems at 120°C, allowing a complete removal of ethanol and water adsorbed. The sample preparation and characterization were carried out at the Surface Science and Spectroscopy Lab of the Catholic University (Brescia, Italy) and in Micro-and-Nanostructure Lab at Elettra facility (Trieste).

Preliminary characterization with X-ray photoemission (XPS) spectroscopy

Sample code	Deposition technique	Salt	Substrate	Roughness (nm)
A	DC	-	ITO	0.24
B	ED	KBr	Gold	5.5
C	ED	KBr	ITO	16
D	DC	KBr	ITO	18

Table 8.1: Main features of the four melanin thin films considered in this work. DC = drop-casting, ED = electrodeposition. The roughness is calculated from the 1.5 x 1.5 μm^2 AFM scans.

of the samples has shown that the thin films obtained from powders diluted in DMSO were not contaminated by sulphur, suggesting that the solvent itself was not present in the sample after drying in air at RT for 24 hours. Furthermore, the C:O:N intensity ratio estimated from C 1*s*, O 1*s* and N 1*s* XPS core level peaks was very close to that predictable from the single monomer composition. Finally, when KBr is dissolved into DMSO, no detectable trace of Br has been found in the electrodeposited thin films.

8.3 Results and discussion

8.3.1 Morphology

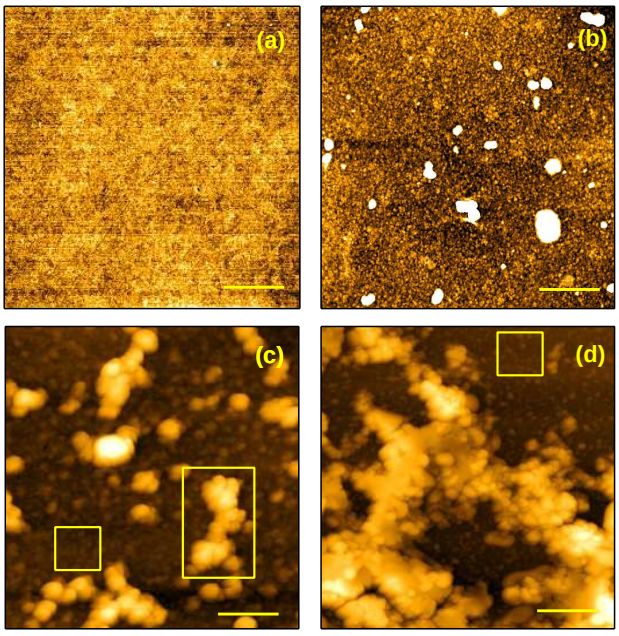

Figure 8.1: Tapping-mode AFM images (10×10 μm^2) of the four samples. The scale bar in the images is 2 μm. (a) sample A, Z scale 2.3 nm; (b) sample B, Z scale 190 nm; (c) sample C, Z scale 320 nm; (d) sample D, Z scale 715 nm. The squares and the rectangle in (c) and (d) indicate homogeneous areas and irregular agglomerates, respectively, considered for the description of the different samples.

Atomic force microscopy has been used for inspecting the morphological structure of the films and for the AFM images the root-mean-square (RMS) surface roughness has been calculated. In Figure 8.1, the 10×10 μm^2 images of the four samples under investigation are shown. According to Figure 8.1-a,

eumelanin dissolved in DMSO and deposited by drop-casting on indium tin oxide (ITO) covered glass substrates (sample A) provides quite homogeneous films, without any hole or crack. The sample is flat, with an extremely reduced RMS roughness of about 0.4 nm; even when the inspected area is increased up to 50x50 μm^2 (not reported), the RMS remains lower than 1 nm. At this level of magnification, no morphological structures are discerned for this sample. It is worth noting that the RMS roughness of the clean ITO surface is only about 3 nm (on a 50×50 μm^2 image) but, since the thickness of eumelanin films is dozen of nm, the RMS roughness of eumelanin films is not influenced by the ITO surface roughness.

The 10×10 μm^2 image of the sample electrodeposited on gold substrates (sample B, Figure 8.1-b) shows some remarkable differences with respect to sample A. First, the film is not flat but is characterized by a granular surface composed of round-shaped units with diameter lower than 100 nm. Secondly, above this continuous film larger aggregates with spherical shape and diameters of up to 800 nm and height up to 200 nm can be occasionally detected. These structures are composed of smaller units about 50 nm in size. The RMS roughness of the total area under investigation is 21 nm, definitely larger than the value estimated from Figure 8.1-a. However the RMS roughness decreases to 6.5 nm when the contribution from larger aggregates is excluded in the calculation, yet this value is far from that evaluated for the drop-casted sample.

The surface of eumelanin electrodeposited on ITO substrates (sample C) is shown in Figure 8.1-c, from where it is evident that, compared to samples A and B, the film is discontinuous and morphologically heterogenous. Spherical particles with diameter within 500 nm and height within 200 nm are the prevalent structures which can be found isolated or to form larger and irregular-shaped agglomerates (rectangle in Figure 8.1-c) with lateral dimension of a few microns and height of 700-800 nm. Nevertheless, all these aggregates clearly comprise smaller round-shaped components, which are comparable in shape and dimension to the smallest units identified in the film electrodeposited on gold substrates. Indeed, these smaller components also determine the granular aspect of the homogeneous areas (e.g., square in Figure 8.1-c) that have been detected in the sample, indicating that, in spite of the inhomogeneities, the features we observe share a common origin. The homogeneous areas texture will be more closely analysed in Figure 8.2.

Finally, the surface of the drop-casted sample on ITO substrates obtained from a solution of eumelanin, DMSO and KBr (sample D) is displayed on Figure 8.1-d. In this film, the morphological disorder is dramatically increased and the largest aggregates can reach dozen of microns in lateral size. These aggregates evidently comprise smaller spherical particles measuring up

to 200 nm in diameter. Though the amount of KBr to be dissolved in DMSO was kept below the solubility limit of the salt in the solvent, we cannot exclude that KBr microcrystals are present in the larger aggregates. However, several homogeneous areas with granular aspect can be still identified on the sample surface (square in Figure 8.1-d). Through a comparison of sample A and D, we can conclude that addition of salt yields large agglomerates on the film surface, with lateral dimensions up to 1 μm and height up to 800 nm. The size and the number of these agglomerates seem to decrease for the ED samples (sample B and C).

In order to better characterize the surface granularity of these samples, higher-resolution images of the melanin films have been acquired; in particular, the 1.5×1.5 μm^2 AFM images have been collected in the most homogeneous areas of each sample (Figure 8.2), such as those identified by a square in Figure 8.1-c and Figure 8.1-d.

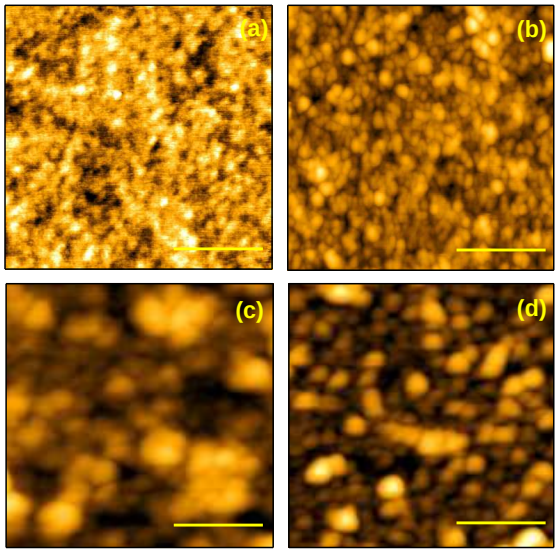

Figure 8.2: Tapping-mode AFM images (1.5×1.5 μm^2) of the four samples. The scale bar in the images is 500 nm. (a) sample A, Z scale 1.5 nm; (b) sample B, Z scale 35 nm; (c) sample C, Z scale 80 nm; (d) sample D, Z scale 200 nm.

At this magnification, a granular structure becomes evident also on the surface of sample A. The film appears to consist of particles of about 50 nm in diameter. These corpuscles outcrop above the surface for less than 1 nm, as the very low RMS roughness value indicates (0.24 nm).
Figure 8.1-b,c and -d show the surfaces of sample B, C, and D respectively, and confirm that these films consists of small particles. At this scale, there

is a clear progressive increase of the RMS roughness going from sample A to sample D: this value starts from 0.24 nm in sample A and increases of at least one order of magnitude in sample B (5.5 nm) and in samples C (16 nm) and D (18 nm), i.e. whenever the KBr salt is added to the solution. Therefore, among the K-doped samples, sample B is more uniform in height. For these samples, the minimum size of the agglomerates is about 50 nm, while a finer grain is detectable for sample A, i.e. for the sample grown without K.

The effect of the salt on eumelanin morphology is particularly evident when the shape and the size of eumelanin particles are inspected on a scale of 250×250 nm^2 (Figure 8.3-b): in sample B (but a similar analysis can be achieved in sample C and D), the granules of 50 nm in diameter have a defined rounded shape (Figure 8.3-b), they emerge on the surface by at least 10 nm (bottom panel of Figure 8.3-b) and no further constituents are detected; in sample A, the corpuscles of 50 nm have not a defined contour, they outcrop for less than 0.5 nm (bottom panel of Figure 8.3-a) and smaller particles of 10-20 nm in diameter may be recognized to further constitute them.

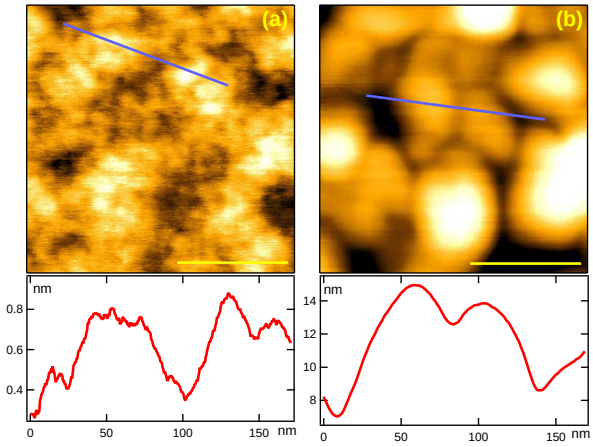

Figure 8.3: Tapping-mode AFM images (250×250 nm^2) of (a) sample A, Z scale 0.9 nm and (b) sample B, Z scale 15 nm. The scale bar in the images is 100 nm. In the bottom panels, cross sections of the agglomerates taken at along the oblique lines in the height images.

We conclude that the presence of KBr in the starting synthetic eumelanin solution yields (i) granules bigger than 50 nm in lateral dimension and higher than 1 nm on the more homogeneous areas of the film, regardless the deposition technique employed (Figure 8.2 and Figure 8.3) and (ii) large agglomerates, that can be reduced by ED, on an otherwise relatively uniform

surface (as shown in Figure 8.1). This effect is particularly significant if the drop-casted samples A and D are compared (Figure 8.1-a and d): using the same substrate and with no external force driving the film growth (like in the electrodeposition process), the morphology of eumelanin films highly depends on the use of potassium in the starting solution, in particular, potassium is fundamental in the assembly of eumelanin aggregates.

Recently, electrochemical deposition of synthetic eumelanin films on gold substrates in aqueous solution has been reported [109]. Also in this case, the granulation is strongly developed when Fe is added to the solution. It is also worth considering the eumelanin aggregates observed on SEM images by Nofsinger *et al.* [20] in biological samples: in that work, Sepia eumelanin, whose native environment is a saline solution that naturally incorporates several metal ions, is clearly composed of spherical particles varying in lateral dimension from about 50 to 250 nm and these corpuscles are, in turn, composed of 15 nm granules; on the other hand, synthetic eumelanin from a metal free solution appears to be structureless on a micrometric scale Figure 8.1-a.

This seems to indicate that metal ions which exhibits a binding affinity with eumelanin could lead to the aggregation of spherical granules with lateral dimension of 50-200 nm, that, according to the hierarchical model proposed by Clancy et al. is the third assemblage stage of the natural melanin formation [16].

At the light of the results presented in this Section, we observe that due to the low density of the large aggregates detected at low magnification (Figure 8.1) and because of the low RMS measured on the 1.5×1.5 μm^2 scale (Figure 8.2), sample B can be selected to probe the effects of K on the structural and electronic properties of eumelanin thin films.

8.3.2 X-ray Diffraction

XRD measurements were conducted on electrodeposited eumelanin on gold substrates and (as a reference) on drop-casted eumelanin thin films on gold substrates from a solution of DMSO and eumelanin powder. The angle dispersive specular scans are plotted against the momentum transfer q_z (Figure 8.4),

$$q_z = \frac{4\pi}{\lambda} \cdot sin\theta \tag{8.1}$$

where $\lambda = 1.1808$ Å is the wavelength used for the experiment. The spectra are dominated by substrate signal originating from mica and gold. On the drop-casted sample, no discernible features different from those of the substrate are distinguished. On the electrodeposited sample a pronounced

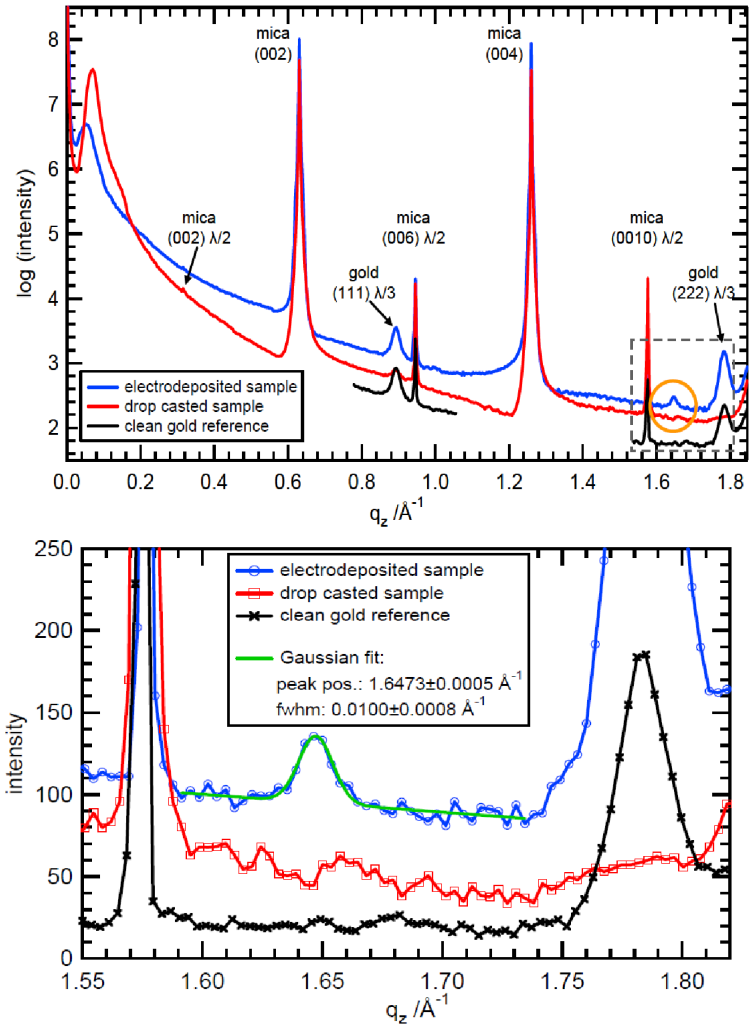

Figure 8.4: Specular X-ray diffraction scans of eumelanin dissolved in DMSO and drop-casted on gold substrates and eumelanin electrodeposited on gold substrates (sample B). These samples are compared to the pristine gold/mica reference. In top panel, the peak assigned to melanin is marked by a circle, whereas the area marked by a dashed box is represented in detail in the bottom panel.

peak is observed at $q_z = 1.647 \pm 0.0005$ Å$^{-}1$; the peak position was determined by fitting the peak to a Gaussian curve with a linear background. The occurrence of this peak cannot be explained by scattering from the gold/mica substrate since it is absent in the reference spectrum, as well as in the scan of the drop-casted melanin film. It can therefore be ascribed to the electrodeposited melanin.

According to the Bragg formula, the position of this peak corresponds to a lattice spacing of $d = 3.81$ Å. This is likely due to the parallel stacking of the planar protomolecules to form the fundamental eumelanin oligomeric units. Indeed this value differs from that found by Cheng et al. [17] in synthetic eumelanin, i.e. 3.45 Å. The modification of the interlayer distance could indicate that potassium ions, which are present in eumelanin electrodeposited film, are able to diffuse within the eumelanin granules (which are at least 50 nm in diameter, as suggested by Figure 8.2-b) and intercalate between the eumelanin protomolecule layers, altering the distance. This is a well known effect in graphite intercalation compounds [188], where the distance between the graphite layers can increase from 3.35 Å to 5.35 Å when the intercalant is potassium [189]. In addition, these data suggest the existence of ion percolation channels within the melanin granules, as recently proposed by Liu et.al [100]. Therefore, the use of the electrodeposition on gold substrates provides high quality films with a significant amount of domains where molecules are oriented parallel to the surface plane, resulting in a structural ordering along the stacking direction of the oligomers.

8.3.3 Linear Dichroism of NEXAFS spectra

The polarization dependence of the NEXAFS spectra was used as an additional technique for supporting the informations on the film structural order gained from X-ray diffraction measurements. Before going into details, a closer look at the involved orbitals and their orientation within the molecule is necessary. The monomer of melanin are composed of a benzene ring combined with a nitrogen-containing pyrrole ring. In aromatic benzene rings, π*-orbitals are known to spread over annular clouds above and below the molecular plane, with a dipole moment oriented perpendicular to the molecular plane. On the contrary, σ*-orbitals are distributed within the molecular plane, as well as the corresponding dipole moment. The π*-orbitals of both carbon and nitrogen in the pyrrole ring can be assumed to have a similar configuration. Therefore one would expect that if the intensity of π*-peaks increases, that of σ*-peaks should simultaneously decreases.

Figure 8.5 shows the NEXAFS spectra at the N $1s$ threshold as a function of the angle θ between the linear light polarization and the surface normal of

the gold substrate. The spectra were normalized in the σ^* part extended from $\approx$ 407 eV (N_C feature) to the higher photon energy part. The N 1s NEXAFS spectrum of eumelanin electrodeposited on gold substrates is dominated by a sharp peak at 398.7 eV (N_A) and a shoulder extending from 400 eV to 404 eV (N_B). The N_A feature is ascribed to the lowest unoccupied electronic level, with a π^* character [110]. Both the N_A and N_B features are observed in the N 1s NEXAFS spectrum of eumelanin powders dissolved in a DMSO solution and deposited by drop-casting on ITO substrates (Figure 8.5-a, sample A); in this case, a polarization dependence of the absorption coefficient can hardly be perceived (not reported), indicating that the melanin molecules are either all oriented at the magic angle ($\alpha = 54°$) or are disordered. On the other hand, the dichroism displayed by the N 1s NEXAFS spectra of the sample electrodeposited on gold substrates indicates that, throughout the surface, the molecules tend to assume a preferred average tilting angle with respect to the substrate. Additionally, since the N_B feature shows the same dichroic behaviour as the N_A peak, it is recognized to have a prevalent π^* character. Similar results are obtained when the same series of angular dependent measurements were repeated on the C 1s and O 1s edges (not reported). Therefore, already at this stage it can be concluded that electrodeposition on gold substrates provides substantial improvements in the production of ordered melanin films.

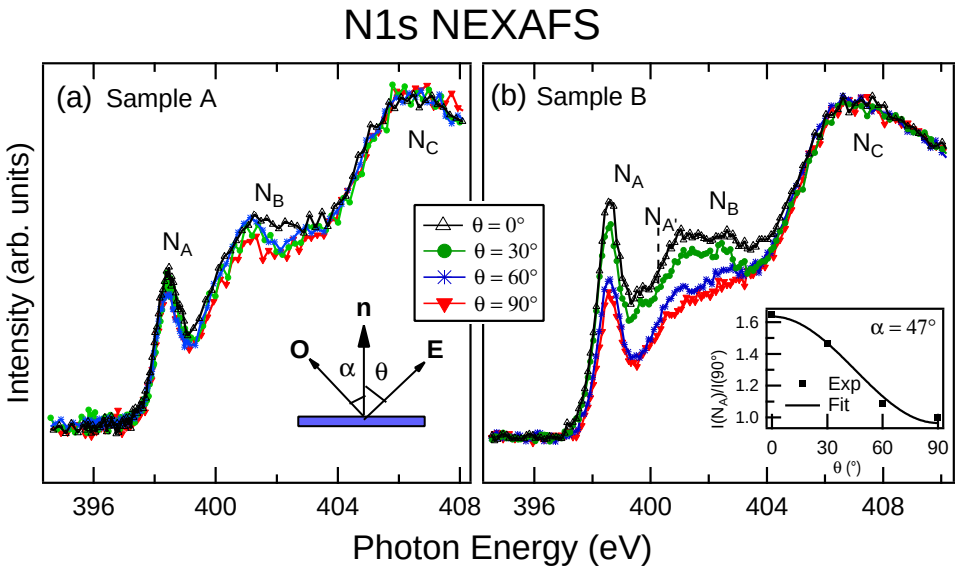

Figure 8.5: Angular dependence of X-ray absorption spectra measured on N K-edge of sample A (a) and sample B (b). Inset in panel (b): intensity of the N_A peak vs the angle of the polarization θ. Measurements are taken at a constant grazing angle of 6°.

In order to quantitatively analyze this geometrical configuration, all the N $1s$ NEXAFS spectra have been deconvoluted by performing nonlinear least-squares fitting on the experimental data through a suitable number of Gaussian and step functions. In particular, the peak N_A contains one Gaussian component and the behaviour of this component versus the angle of the polarization θ is shown in the inset of Figure 8.5-b. According to Stöhr [47] and to the present scattering geometry [49], in the case of a π^* orbital, the angular dependance of the resonance intensity can be described by the following formula:

$$I(\theta) = A \cdot \left[1 + \frac{1}{2}\left(3cos^2\alpha - 1\right)\left(3cos^2\theta - 1\right)\right] \tag{8.2}$$

where A and α are the free fitting parameters and a cylindrical symmetry for the policrystalline substrate has been assumed. Specifically, α is the angle between the melanin molecular planes with respect to gold surface. From the fit of the angular dependance of peak N_A, an average tilt angle of $\alpha = 47 \pm 5°$ is obtained as a result. Actually, since X-ray diffraction measurements showed that a relevant number of molecules lies flat on the surface, this angle should be intended as an average angle, to which also molecules with the plane tilted with respect to the surface contribute. Yet, the domains can be oriented only in a few direction otherwise no dichroism would be detected in the NEXAFS measurements. For example, the intensity plot for $\alpha = 47°$ can be well reproduced if 53 % of the domains has $\alpha = 90°$, alternatively if 72 % of the domains has $\alpha = 60°$. This clearly shows that the experimental angle $\alpha = 47°$ could originate from at least two differently oriented domains, in which one lies flat on the substrate.

However, the question of how these domains are distributed along the direction perpendicular to the substrate surface remains still open. In fact, it should be reminded that the measurement of X-ray diffraction is a bulk-sensitive technique, while the X-ray absorption spectroscopy in the partial yield detection mode is known to explore the sample properties in the surface layers. At the light of this consideration, the previous results can be interpreted in the following way: the contact with a gold substrate at which an electric field is applied could cause the melanin molecular plane to align parallel to the substrate itself. This is surprising since, despite the disorder and the supramolecular organization, melanin seems to act like porphyrins and phthalocyanines, for which the orientation on gold is simply driven by the maximization of the overlap between the π^*-orbitals with the electron cloud of the metal surface [49]. In this perspective, the strong resemblance of the eumelanin planar protomolecule with the aromatic ring of porphyrins and phthalocyanines is further supported. Then, growing away from the substrate, eumelanin molecules are likely to change orientation.

When eumelanin is dissolved in DMSO and drop-casted on ITO substrates, since neither angular dependance of NEXAFS spectra nor specular peaks in the X-ray diffraction data have been detected, the eumelanin fundamental units probably rearrange in a random way (i.e. without any long range order). Nevertheless, if the eumelanin is dissolved in DMSO and electrodeposited on gold substrates, a long range order is reconstituted as indicated by the X-ray diffraction measurements. These experimental results indicate that the electrodeposition process on gold drives the eumelanin particle to deposit with a preferential geometrical arrangement, i.e. the electrodeposition technique substantially improves the melanin films inner order.

8.3.4 Preliminary study of electronic properties

In the previous section, the intercalation of potassium in the electrodeposited films has been considered to justify the increase of the inter-layer distance. At this point, it is interesting to determine where potassium is located in the melanin oligomer, as well as how the presence of potassium in the electrodeposited film may alter the electronic structure of synthetic eumelanin compound. In the following, the soft X-ray spectroscopy data of the electrodeposited film (sample B) are compared to the corresponding set of spectra collected from eumelanin dissolved in DMSO and drop-casted on ITO substrates (sample A). Due to the high chemical disorder of eumelanin, which is known to contain four different monomers, nitrogen-related experimental data have been selected for a straightforward analysis, since each of the different melanin monomers contains one single N atom, providing an unambiguous information about possible interaction of nitrogen with potassium.

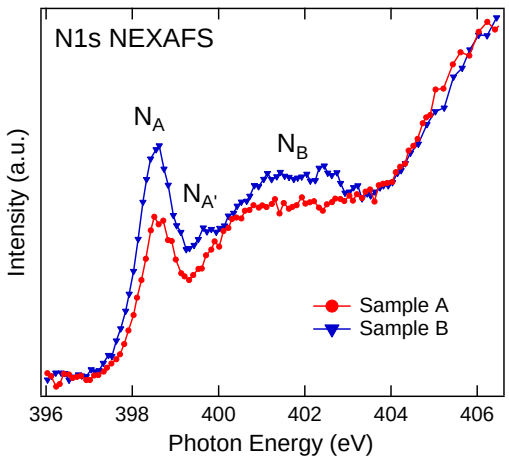

Figure 8.6: N 1*s* NEXAFS spectra of sample A and B collected at $\theta = 60°$.

The NEXAFS measurements (Figure 8.6) provides information on the unoccupied molecular orbitals. In particular, the N 1*s* NEXAFS spectra collected at $\theta = 60°$ have been compared in order to avoid possible dichroism effects for spectra collected far from the magic angle conditions ($\theta = 60°$ is very close to $\theta = 54°$, the magic angle). These spectra were normalized in the σ^* part located at ≈ 407 eV. As mentioned above, all the N 1*s* NEXAFS spectra are dominated by a sharp peak at 398.7 eV (N_A) and a shoulder extending from 400 to 404 eV (N_B). Nevertheless, in the N 1*s* NEXAFS spectrum of the electrodeposited sample a small feature appeared at $h\nu = 399.5$ eV ($N_{A'}$). In sample B, the N_A peak intensity is enhanced with respect to the drop-casted sample A, and the N_B shoulder is different too. Thus, the density of unoccupied states higher in energy results to be changed.

These experimental evidences point out that one of the possible binding sites for potassium in synthetic eumelanin is the imine group. Actually, it has been suggested that in natural melanin the alkali and alkaline earth cations bind to carboxyl group [100]. However, the inspection of the coordination of Zn(II) in both Sepia melanin and synthetic DHI melanin offers an interesting situation: whereas in the biological sample Zn(II) share the same site as Mg(II) and Ca(II) [106], in the synthetic material, being smaller the concentration of COOH, zinc is more prone to bind to imine sites [107]. This underlines that the experimental results for natural eumelanin cannot apply straightforwardly to synthetic eumelanin, as our experimental results seem to confirm.

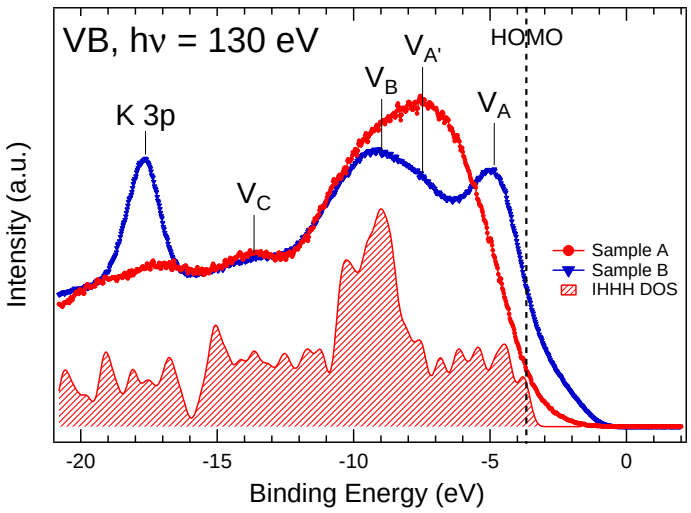

Figure 8.7: Valence band spectra of sample A and B collected by exciting the sample with hν = 130 eV photon energy. The main melanin bands are labelled from V_A to V_C. The filled spectrum represents the calculates density of states of the tetramer IHHH.

Finally, the valence band spectra collected at $h\nu = 130$ eV photon energy are presented for the undoped drop-casted sample on ITO (sample A) and for the electrodeposited eumelanin on gold substrates (sample B) (Figure 8.7). XPS probes the local chemical environment and is rather sensitive to changes on a scale length of the order of the molecule dimensions. Since we have detected differences in morphology on a much larger scale length, we do not expect to observe changes in the photoemission spectra due to the thin film morphology. Rather, the presence of K ions nearby the photoemitting molecule is expected to be tracked.

The spectral features of sample A data have been singled out in agreement with the analysis carried out in Chapter 7.3.2. The same structures are found in the sample B spectrum, except for the K $3p$ peak located at 17.6 eV in BE. However, remarkable differences are found in the region below 10 eV, where the intensity ratio of features V_A, $V_{A'}$ and V_B is deeply affected. In particular, the peak V_A grows in intensity when potassium is inserted in sample B. Moreover, at the low-BE side of this peak, an increase of the spectral weight is observed, suggesting that additional electronic states are contributing to the spectrum at low energies. The two valence band spectra are plotted together with the calculated density of states (DOS) for an undoped tetramer composed of three HQ and one IQ monomers (named IHHH), which can be regarded as one of the most probable eumelanin protomolecules, when eumelanin is obtained from the oxydation of tyrosine (Chapter 7). The comparison of the two valence band spectra shows that the insertion of potassium strongly affects the electronic occupied states below the HOMO (indicated by a bold broken line in Figure 8.7).

8.4 Conclusions

In conclusion, we have shown that K has relevant effects on the morphology of thin films of synthetic eumelanin on conducting substrates, being able to affect the growth and the size of eumelanin aggregates. Indeed, the use of different substrates and deposition techniques strongly affects the agglomeration characteristics of synthetic melanin and the quality of the film on a micrometric scale. When eumelanin dissolved in a KBr solution is deposited on ITO subtrates by drop-casting (sample D), the film is strongly inhomogeneous on a scale size larger than 5 μm and aggregates of dozen of microns in lateral size can easily form. The formation of these large agglomerates on ITO is restrained whenever the electrodeposition technique is employed for growing eumelanin films (sample C), yet these films are still affected by heterogeneous structures. More homogeneous films are obtained only when

the electrodeposition technique is applied on gold substrates (sample B). In this sample, the quality of the film strongly improves: the surface is quite continuous and only occasionally interrupted by particle with diameter exceeding 500 nm. Due to the low density of the large aggregates detected al low magnification (Figure 8.1), sample B has been selected to probe the structural and electronic properties. XRD and NEXAFS provide evidence of bulk long-range ordering and partial orientation in the topmost layers, respectively. Finally, the presence of potassium also affects the electronic states across the energy gap through a transfer of spectral weight involving the HOMO level, along with a clear interaction with nitrogen atoms in the molecule.

Chapter 9

Electronic states in K-doped eumelanin: theory and experiments

9.1 Introduction

In Chapter 8, the role of K ions on eumelanin aggregation behaviour has been assessed. Besides, the efficiency of the electrodeposition technique in controlling the size of agglomerates and improving the aligment of eumelanin protomolecules has been shown. A preliminary analysis on the influence of K ions on the electronic properties, based on a comparison of the experimental valence bands to the calculated DOS of IHHH tetramer, suggested that a transfer of the spectral weight involving the HOMO level occurs after K intercalation. According to the nitrogen-related experimental data, we found that the K ions interact with nitrogen atoms in the molecule, supporting the validity of a macrocyclic tetramer as a model protomolecule.

In this chapter, a further refinement of the eumelanin tetramer model is achieved by calculating the most favourable position for K atoms in the eumelanin macrocycle. For the K-doped protomolecule, the calculated DOS and N 1s NEXAFS spectra are presented and compared to the experimental results. Supplementary soft X-ray electron spectroscopies data are provided for both the undoped (sample A) and doped samples (sample B and C) introduced in Chapter 8. In particular, similar experimental results are obtained for electrodeposited films on Au (sample B) and on ITO (sample C), showing that the choice of the substrate poorly affects the electronic properties of the electrodeposited samples. While in Chapter 8, electrodeposited films on Au (sample B) were selected for an accurate structural analysis due to

the high homogeneity of the surface film, in the present chapter we resort to consider electrodeposited film on ITO (sample C) for further inspecting the effects of K intercalation on eumelanin electronic porperties with resonant photoemission (ResPES) experiments on C K-edge. This choice is motivated by the fact that, in view of possible applications to electronic organic devices such as dye-sensitized solar cells (DSSCs), conductivity and transparency to UV-VIS are simultaneously guaranteed only by ITO substrates.

9.2 Results and discussion

9.2.1 Calculated K-tetramer formation energies and DOS

According to the results of Chapter 8.3.4, in synthetic eumelanin one of the possible binding sites for K-ions is the imine group. Based on our calculations in the Chapter 7, we have studied two melanin tetramers, the QIQI and IHHH, both with two H atoms bound to two N atoms. While the former was recognized to be energetically more stable in the gas phase, we found that, in the sample containing eumelanin synthetized by oxidation of tyrosine with hydrogen peroxide, calculations on the IHHH tetramer better matches with the experiment. The K ion is placed in three different configurations with respect to the macrocycle:

- the K ion sits inside the cage of the macrocyle. The two H are removed;
- the K ion is about 1.5 Å above the macrocycle and the geometry of the system is allowed to relax. The two H are removed;
- the K ion is about 1.5 Å above the macrocycle and the geometry of the system is allowed to relax. The two H remain inside the macro-cycle;

In Table 9.1 the calculated binding energy of the K ion in each molecular structure is listed. The first important result is that, upon relaxation, in both IQIQ and IHHH tetramers the K ion does not incorporate into the cage but prefers to sit above it. The favoured configuration is when the tetramer has the H atoms are bound to the N inside the macrocyle and the K ion lies above the macrocycle. After relaxation, the K ion is about 2 Å above the plane formed by the 4 N atoms in the macrocyle. This value is compatible with the experimental observation that upon K intercalation there is an increase in the interlayer distance from $d = 3.45$ Å to $d = 3.81$ Å (see the XRD results on sample B in Chapter 8.3.2). Although the theoretical value is slightly in

	K position	# H	Energy of K ion
K-IHHH	IN	0	2.95 eV
K-IHHH	OUT	0	-1.02 eV
K-IHHH	OUT	2	-4.15 eV
H-QIQI	IN	0	2.35 eV
H-QIQI	OUT	0	-0.25 eV
H-QIQI	OUT	2	-2.72 eV

Table 9.1: Calculated binding energy of the K ion when it is interacting with the macrocycle of the IHHH and IQIQ tetramers. This energy is calculated when K ion is located in the molecular plane (IN) as well as when the K ion is relaxed at 2 Å far from the molecular plane (OUT). Besides, the possibility for the two hydrogen atoms either to be removed (0) or to remain in the macrocyle (2) has been considered.

excess with respect to the experimental one, we have to take into the account that these calculations neglect the effect of the stacking on the intercalation process by considering the presence of just one tetramer.

Both the favoured molecular structure for IHHH and IQIQ are represented in Figure 9.1. However, from Table 9.1, the preferred tetramer for K binding in gas phase is IHHH. Therefore we will proceed with a further analysis of the electronic properties by considering the density of states (DOS) and the projected DOS calculated for this configuration, named K-IHHH. In Figure 9.2-a the total DOS, along with the projected DOS on the O $2p$, O $2s$, N $2p$, N $2s$, K $3p$ and K $4s$ orbitals, is plotted. The HOMO level is set to 3.19 eV. Despite the major contribution to the whole DOS comes from C-derived states (not reported), a significant contribution to the spectral weight in the region between HOMO and 15 eV is given by O $2p$ and N $2p$ orbitals. On the other hand, the contribution of the N $2s$ states is located above 5 eV, while the O $2s$ states appears only above 7 eV.

As it can be observed, apart from the peak at 17.6 eV due to K 3p states, the contribution from the potassium states to the DOS of the tetramer is virtually close to zero. Actually, the K-derived states are found throughout the whole DOS of the protomolecule, as evidenced by Figure 9.2-c, but the intensity with respect to the N- and O-derived states is at least two orders of magnitude less. Of particular interest for further discussions is the DOS at HOMO energy (enlarged in Figure 9.2-b), which receives contribution principally from C $2p$ states (not reported), but also from O $2p$ and N $2p$ orbitals. Although a contribution to the HOMO level is also given by K $4s$ states, this is estimated to be at least two orders of magnitude less than the orbitals of other atoms. A charge transfer from the K atom to the protomeolecule to yield a K^+ ion and a $IHHH^-$ molecule is therefore expected.

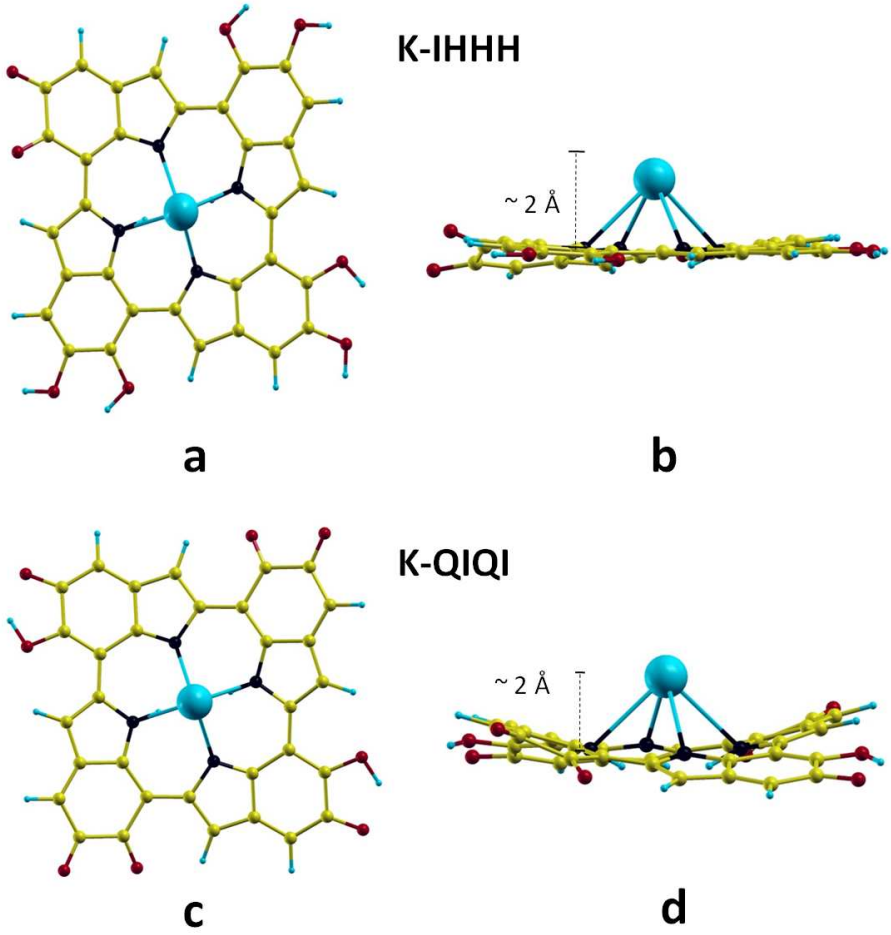

Figure 9.1: Molecular structure of the K binding to the IHHH tetramer, displayed in top view (a) and in side view (b), and to the IQIQ tetramer, displayed in top view (c) and in side view (d). According to calculations, the energetically more stable configuration in both tetramer is achieved when the K ion lies 2 Å above the plane formed by the 4 N atoms in the macrocyle and the two hydrogens atoms remain inside the ring.

The question is to understand where the extra electron goes.

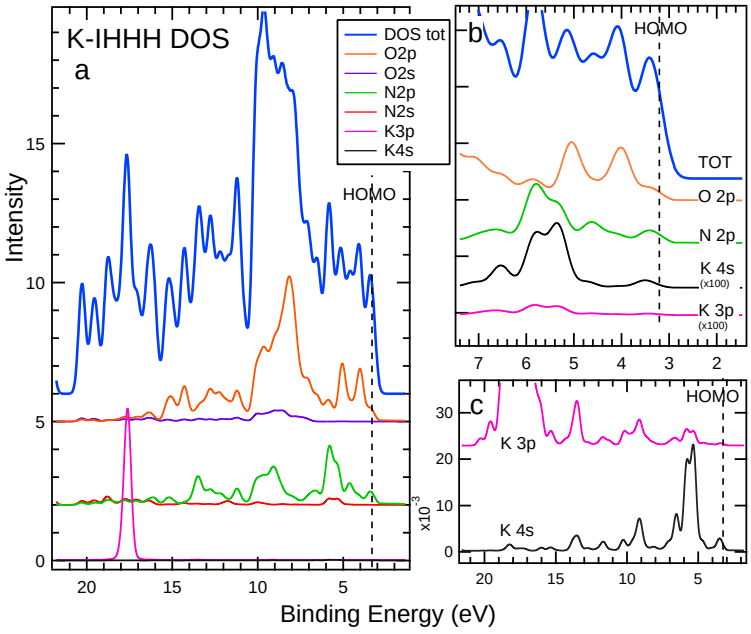

Figure 9.2: (a) Calculated density of states of the K-IHHH tetramer and projected DOS on the O $2p$, O $2s$, N $2p$, N $2s$, K $3p$ and K $4s$ orbitals. (b) Magnification of the HOMO region of panel (a). (c) Magnification of the K-derived states.

9.2.2 Valence Band study

In Figure 9.3, the calculated DOS for K-IHHH is compared to the valence band spectra of the electrodeposited sample grown on Au substrate (sample B) and on the ITO substrate (sample C). In the same figure, the calculated DOS for IHHH and the valence band spectrum of the undoped sample on ITO (sample A) are also shown in order to obtain further information on the K influence on the electronic properties of eumelanin. Experimental spectra are collected at photon energy $h\nu = 281$ eV and the main features are labelled according to the previous analysis in Chapter 7.3.2 and Chapter 8.3.4.

In the spectra of sample A and sample C, the shoulder at about 19 eV of binding energy (BE) is due In $4d$ electrons coming from ITO, because the photon beam impinged part of the uncovered substrate. The intense peak at BE = 17.6 eV in the spectra of sample B and C is ascribed to K $3p$ states, and has a clear counterpart in the calculated DOS of K-IHHH (see also the projected DOS of K $3p$ states in Figure 9.2). Considering that in the spectrum of sample C the K $3p$ peak is overlapped to the In $3d$ peak, the

quantity of potassium in both the electrodeposited sample can be estimated to be very similar. Actually, a more precise calculation of the potassium quantity in the doped samples has been achieved by evaluating the core-level peak areas in the survey spectrum and by scaling them with respective cross section for photoemission [190]. Although this method is not exact (e.g., corrections for electron transmission function of the analyser are neglected), satisfactory results have been obtained for stochiometric compounds: e.g., XPS spectra of KBr dissolved in DMSO and deposited on ITO substrates have been collected and from the survey spectrum a ratio K : Br = 1 : 1.04 is calculated (the theoretical ratio is 1 : 1). With this method, the N : K ratio results 1 : 0.65 in sample B and 1 : 0.69 in sample C, confirming that both the electrodeposited samples contain a similar quantity of K.

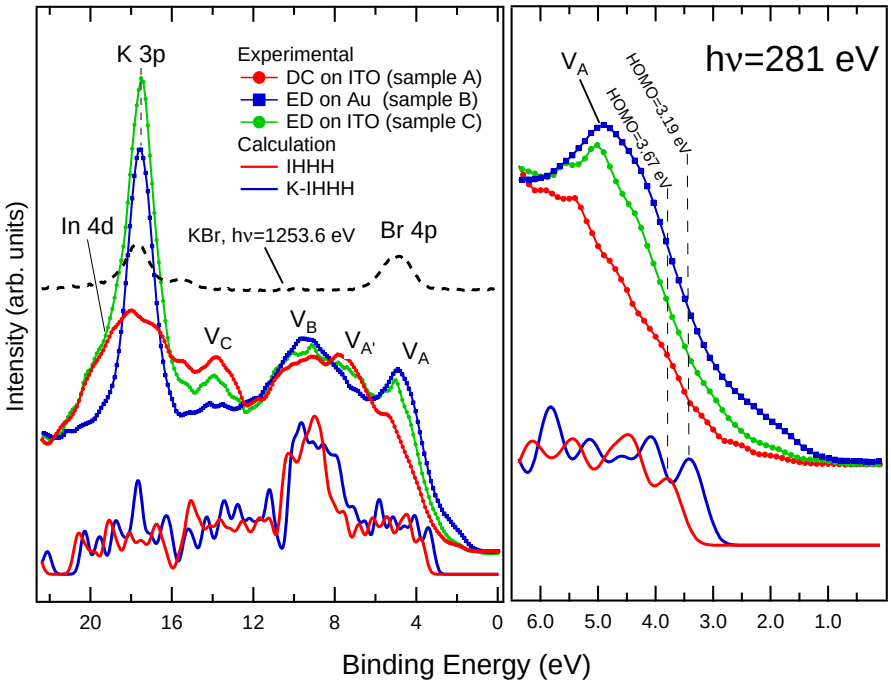

Figure 9.3: Experimental VB spectra of sample A (red circles), sample B (blue squares) and sample C (green triangles) collected at hν = 281 eV compared to the experimental VB spectrum of KBr dissolved in DMSO and deposited on ITO (black dashed line, hν = 1253.6 eV). In the bottom part of the figure the calculated DOS of the IHHH (red line) and of the most favoured K-IHHH molecular structure (blu line) are shown.

By comparing the experimental spectra of sample A, B, C, we notice that the principal modifications in VB after K-intercalation are the decrease of peak V_C intensity and the increase in intensity of peak V_A and its low-BE

side[1]. Indeed, the calculated DOS on the IHHH tetramer indicates that upon K-doping additional electronic states appear in the total DOS at low energies, shifting the HOMO of about 0.5 eV toward lower energies with respect to the undoped case. This trend is enhanced in sample B, despite the quantity of potassium is assumed to be close to that in sample C, which suggests that the K-intercalation has been, to some extent, more efficient in sample B.

The influence of K intercalation on low-BE region of valence band is also evident when the case of K-evaporation on eumelanin thin films is analysed. In Figure 9.4, Ultraviolet Photoemission spectra (UPS, obtained with He II radiation) of eumelanin thin films dissolved in DMSO and drop casted on Au substrates (a) are compared to UPS spectra of eumelanin thin films electrodeposited on Au substrates (b). Spectra are taken before K evaporation (indicated by circles) and after four cycles of K-evaporation and annealing in UHV enviroment (indicated by open triangles). Before evaporation, in the electrodeposited sample we recognize an increase of peak V_A intensity with respect to the DC sample spectrum (BE = 5 eV), as seen in sample B VB spectrum. When potassium is evaporated on both the DC sample and the ED sample, an increase in intensity in 1-4 eV region is clearly detected, and this cannot be obviously ascribed to Br $4p$ states. In summary, K-doping yields additional electronic states to the VB spectrum at low energies, with K atoms that probably donate their $4s$ electrons to the eumelanin macromolecule. This effect is observed in electrodeposited sample as well as in eumelanin thin films after K-evaporation. The shift of HOMO level towards

[1]From XPS measurements, a residue of Br is detected, indicating that part of potassium is still present as KBr on the film surfaces. Specifically, the ratio K : Br is 5.4 : 1 in sample B and 5.5 : 1 in sample C indicating that about 18 % of the total potassium quantity is not involved in the doping process of eumelanin. Therefore, the increase in intensity of peak V_A could be ascribed to Br $4p$ peak (BE = 5 eV), as revealed by looking at the VB of KBr KBr dissolved in DMSO and deposited on ITO substrates (black dashed line in Figure 9.3, left panel). In this spectrum, since the substrate was totally covered by KBr and DMSO completely evaporated, no electrons coming from either ITO or DMSO contribute to the spectrum. The intensity of the KBr spectrum is scaled so that the K $3p$ peak area is about the 18 % of the K $3p$ peak area in the VB spectra of sample B and C, i.e. the K $3p$ peak and the Br $4p$ peak in the spectrum of KBr are a rough estimate of the undissolved KBr in sample B and C. However, the VB spectrum of KBr is collected at photon energy $h\nu$ = 1253.6 eV, for which the cross section ratio $\sigma_{K3p}/\sigma_{Br4p}$ is 1.25 while at $h\nu$ = 281 eV this value is 3.84. Therefore, in order to account the contribution of Br $4p$ orbitals to peak V_A in spectra of sample B and C, the Br $4p$ peak area in the VB spectum of KBr should be decreased of two thirds. By all means, this is obviously a quite rough approximation, but it helps us to estimate that in VB spectra of sample B and C the increase of peak V_A is not completely due to the presence of Br. Besides, if we take a closer look at the HOMO region (Figure 9.3, right panel), we note that upon intercalation there is a net increase in intensity of the tail in the 1-4 eV region, which cannot be explained only by the presence of Br in the samples.

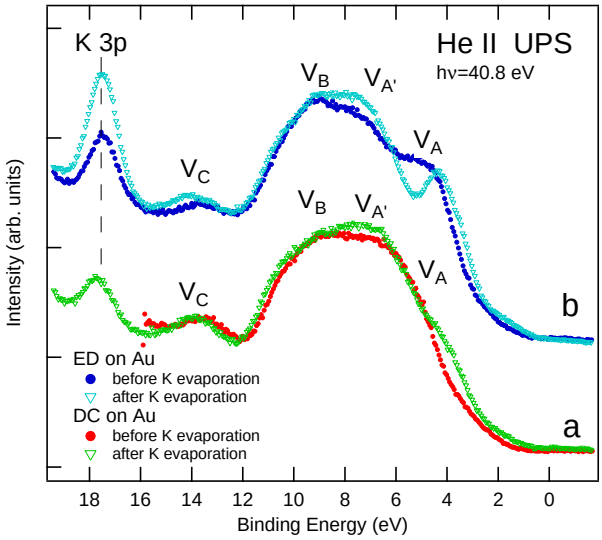

Figure 9.4: He (II) UPS spectra collected on eumelanin dissolved in DMSO and drop casted on Au substrate (a) and on eumelanin electrodeposited on ITO in a solution of DMSO and KBr (b). Spectra are measured before (circles) and after (open triangles) four cycles of K-evaporation and annealing.

lower binding energy is also predicted in the calculated DOS of the K-IHHH protomolecule, supporting the model proposed in Chapter 9.2.1.

9.2.3 Linear Dichroism of N *K*-edge NEXAFS spectra

In Chapter 8, electrodeposition was recognized as a practical deposition method for both controlling the aggregation effect of K ions on eumelanin structure and for limiting the presence of Br from the starting solution. However, only electrodeposited films on Au (sample B) were selected for an accurate structural analysis due to the higher homogeneity of the surface film with respect to the sample C (eumelanin electrodeposited on ITO) and beacause sample C was not a good candidate for XRD measurement, since the substrate (ITO on glass) yields a broad amorphous-halo in the XRD pattern that overwhelms the thin film contribution to the XRD pattern.

Indeed, the polarization dependence of the NEXAFS spectra has been measured on sample C to verify to which extent the two electrodeposited films share the same structural properties. First, in Figure 9.5-a N 1s NEXAFS spectra of sample A, B and C, normalized in the σ^* part located at $\approx$ 407

eV, are shown. These spectra have been collected at $\theta = 60°$ [2] in order to avoid possible dichroism effects for spectra collected far from the magic angle conditions ($\theta = 60°$ is very close to $\theta = 54°$, the magic angle). It is clear that both the electrodeposited samples are characterized by a sharp peak at 398.7 eV (N_A), a shoulder extending from 400 eV to 404 eV (N_B) and a weaker feature at $h\nu = 399.5$ eV ($N_{A'}$), which is absent in sample A spectrum, as already evidenced in Chapter 8.3.4. Besides, the shape and intensity ratio of all these features remain constant when passing from sample B to sample C, confirming that in both the doped samples the K ions have an analogous effect on the N binding.

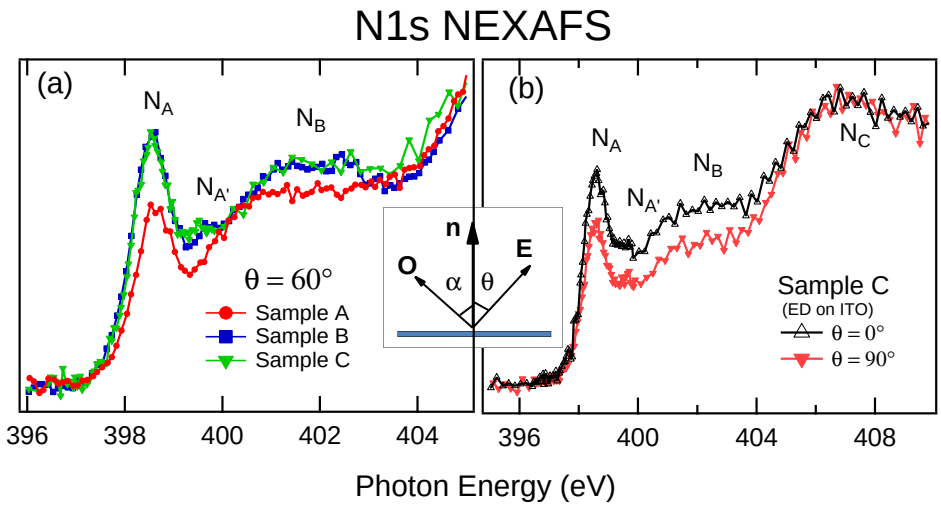

Figure 9.5: N 1s NEXAFS spectra of sample A, B and C collected at $\theta = 60°$ (a). Angular dependence of X-ray absorption spectra at N K-edge measured on sample C (b). All measurements are taken at a constant grazing angle of 6°.

In Figure 9.5-b, NEXAFS spectra at N K-edge of sample C are displayed for p-polarizazion ($\theta = 0°$) and s-polarization ($\theta = 90°$). The dichroism exhibited by these spectra indicates that, as for sample B, throughout the surface, the molecules tend to assume a preferred tilting angle with respect to the substrate. Following the same analysis for the angular dependance of peak N_A intensity as described in Chapter 8.3.3, an average tilt angle of $\alpha = 51 \pm 5°$ [3] is obtained as a result. This angle is very close to that found for sample B ($\alpha = 47°$), suggesting that whenever eumelanin is electrodeposited

[2] According to notation introduced in Chapter 2.1.5, θ is angle between the X-ray polarization vector and the normal to the surface

[3] α is the angle between the melanin molecular planes with respect to the normal at the surface.

in a solution containing K ions, a well defined self-assembly behaviour is manifested throughout the surface, independently from the substrate chosen. This is not surprising since all the eumelanin films analysed in this work are dozen of nm thick and therefore no influence on the surface structural properties of eumelanin is expected from the substrate[4].

In conclusion, the analysis of N 1s NEXAFS spectra and VB spectra (see section 9.2.2) has revealed that sample B and C are comparable with respect to structural and electronics properties. Therefore, we select sample C for next analysis, because in view of possible applications to electronic organic devices such as dye-sensitized solar cells (DSSCs), the ITO substrates is the only support for eumelanin that possess simultaneously conductivity and transparency to UV-VIS.

9.2.4 Resonant Photoemission at C *K*-edge

Figure 9.6 and Figure 9.7 show the valence band ResPES of sample A and sample C, respectively, obtained by scanning the photon energy across the C 1s absorption threshold, from 281.0 eV to 291 eV. In the right panels, the C 1s NEXAFS spectra measured during the ResPES scans are also shown for each sample, while, as an example, the off-resonance valence band spectra collected with hν = 281.0 eV photon energy are displayed in the bottom panels of the ResPES plots. C 1s NEXAFS features are labelled according to analysis accomplished in Chapter 7.3.3. All data are normalized to the substrate signal collected at the same photon energies.

In both samples, the first resonance in ResPES spectra is detected at about hν = 285.1 eV (C_A peak in Figure 9.6 and Figure 9.7), for which all valence band features show an intensity enhancement. In the XAS spectrum, the lowest lying C_A peak can be ascribed to excitation into π^* empty orbitals, as it is usually found in hydrocarbon rings (see, e.g., Ref. [47]), while in the region at higher photon energies an increasing contribution from σ^* states is expected [47]. Beyond this enhancement, an Auger emission with a clear dispersive behaviour on the BE scale (i.e. a normal Auger emission) appears. Besides, in Figure 9.7, a relevant contribution from the direct photoemission peak of K 3p can be observed at BE = 17.6 eV.

[4]Actually, it is not excluded that also eumelanin films depositited on ITO (sample A) display self-assembling properties on the surface. In fact, the absence of dichroism in sample A, as disclosed in Chapter 8.3.3, could derived from the protomolecules oriented at the magic (average) angle of $\alpha = 54°$, which is very close to the tilt angles calculated for samples B and C. In this case, eumelanin would be likely to possess a preferential angle for the orientation of protomolecules on the surface that is independent from the deposition technique and the metal doping employed.

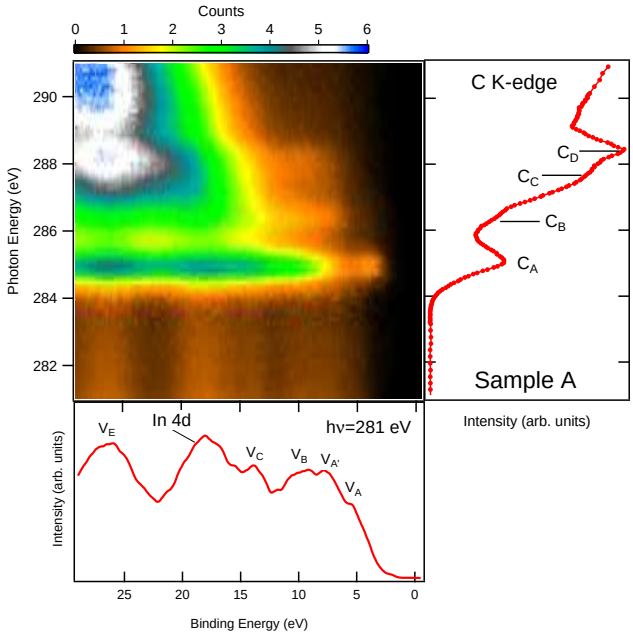

Figure 9.6: ResPES data of eumelanin dissolved in DMSO and drop casted on ITO (sample A) collected across the C 1s absorption threshold. Valence band collected with hν = 281 eV photon energy (bottom panel). C 1s NEXAFS spectrum (right panel).

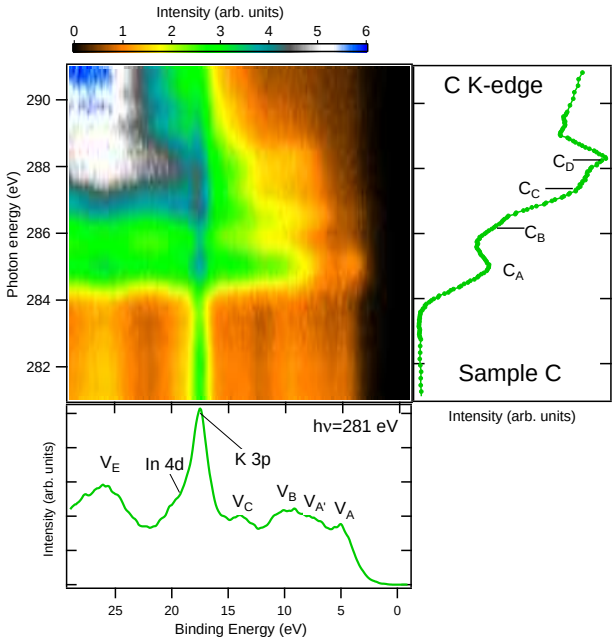

Figure 9.7: ResPES data of eumelanin electrodeposited on ITO in a solution of DMSO and KBr (sample C) collected across the C 1s absorption threshold. Valence band collected with hν = 281 eV photon energy (bottom panel). C 1s NEXAFS spectrum (right panel).

In order to evidence only the truly resonating features, the contour plots of the resonant spectral weight (RSW) for sample A (a) and sample C (b) are shown in Figure 9.8. The RSW has been obtained by subtracting from each of the measured spectra the normal Auger emission and the off-resonance spectrum collected at hν = 281 eV, i.e. below the absorption edge. In this way, one can identify the electronic states resonating at the the carbon K-edge and the photon energy where the resonant enhancement occurs.

The RSW contour plots of the undoped and doped samples share some characteristics. As the photon energy is varied across the the first C 1s $\rightarrow$ π^* transition (peak C_A), a sharp enhancement of the VB region around 3.8 eV binding energy is detected in both samples and, according to the characterization furnished to decay channels in Chapter 2.2, is assigned to participator decay. This VB region corresponds to the low-BE side of peak V_A, as can be deduced by combining the off-resonance spectra displayed at the bottom of each RSW contour plots. Simultaneously an intense hump appears at higher binding energies (corresponding to VB features V_B and V_C).

Whereas this large hump disappears in both samples only when the photon energy is increased beyond hν = 286.5 eV, i.e. beyond the C_B absorption peak, the resonant behaviour of the low-BE side of peak V_A is different in the two samples: in sample A, the resonant enhancement monotonically decreases as C 1s electrons are promoted to empty states assigned to peak C_B; on the other hand, in sample B, a small enhancement of the VB region around BE = 3 eV is observable for photon energies crossing peak C_B (indicated by a red arrow in Figure 9.8-b).

This is more evident when the individual RSW spectra at the absorption edge of peak hν = 285.1 eV (C_A) and hν = 286.6 eV (C_B) are plotted in the 0-6 eV range (Figure 9.9-b and -c, left panel). At hν = 285.1 eV (Figure 9.9-b, left panel) the 1-5 eV energy region is enhanced in both samples. A comparison with off-resonance VB spectra (Figure 9.9-a, left panel) shows that this resonance doesn't involve peak V_A but its low-BE tail. Since V_A peak doesn't seem to resonate across C K-edge at all in any sample, peak V_A can be ascribed mainly to O 2p and N 2p orbitals.

In Figure 9.9-c (left panel) the RSW spectra at hν = 286.7 eV are also shown. Here, a small enhancement in the 1-3.5 eV energy range is detected mainly for sample C, confirming that the K-intercalation provides new states in that VB region. Besides, since the resonant photoemission process requires the spatial overlap among the involved occupied and unoccupied orbitals (see Chapter 2.2), the states in the 1-3.5 eV energy range of sample C can be located on the same carbon atoms where the unoccupied states contributing to peak C_B are found (Figure 9.7, right panel).

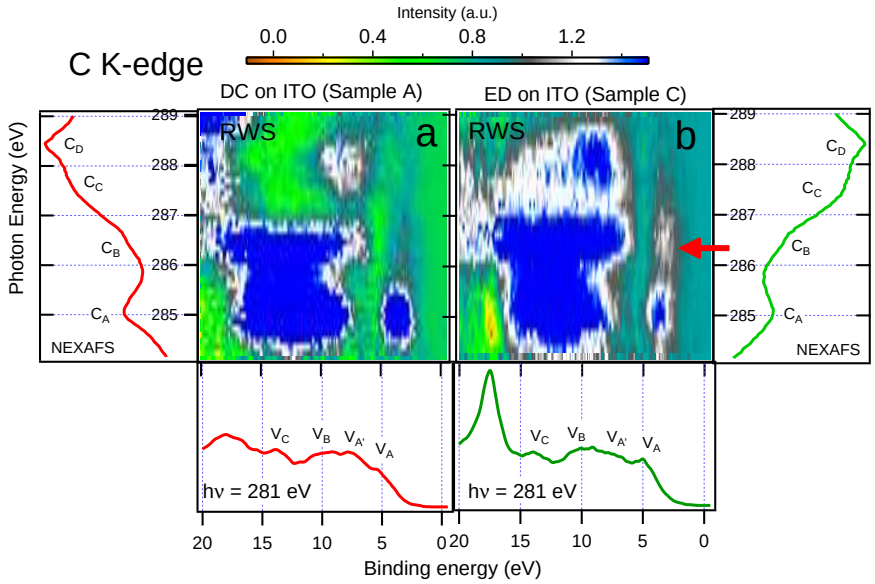

Figure 9.8: Contour plots of resonant spectral weight (RSW) spectra of sample A (a) and sample C (b). The RSW has been obtained by subtracting from each of the measure spectra the normal Auger emission and the off-resonance spectrum (bottom panels) collected below the absorption edge, at hν = 281 eV. In the lateral panels, NEXAFS spectra collected during the ResPES scan of each sample are shown.

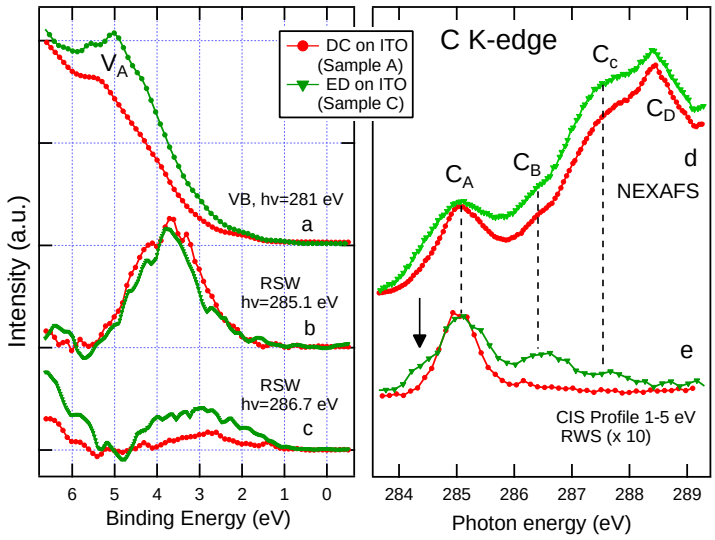

Figure 9.9: Left panel: RSW spectra of sample A (red cicles) and sample C (green triangle) at at hν = 285.1 eV (b) and at hν = 286.7 eV (c). The VB spectra at hν = 281.0 eV are also shown (a).
Right panel: C 1*s* NEXAFS (d) and the CIS profile of RSW spectra in the 1-5 eV energy range (e) of sample A (red circles) and sample C (green triangles).

This behaviour is confirmed when the intensity of selected regions of the valence band is plotted against the photon energy (Constant Initial State, CIS, curve), as shown in right panel of Figure 9.9. Both the structures in the 1-5 eV (Figure 9.9-e, right panel) are enhanced in sample C as the photon energy approaches hν = 286.0 eV. Furthermore, a smaller enhancement can be estimated for sample C also at hν = 287.0 eV, i.e. when peak C_C occurs, but in this case the low signal-to-noise ratio prevents a reliable identification.

Further remarks can be done when C 1s NEXAFS spectra of sample A and C, collected in partial yield mode and normalized in the σ^* part located at $\approx$ 295 eV, are considered (Figure 9.9-d, right panel). These spectra are very similar, yet the intensity of the features labelled as C_B and C_C are increased in sample C, just as observed in the CIS profiles at the same photon energies. This confirms that, at higher photon energies than the first allowed excitation, the K ion doping induces additional electronic states. The resonances found in CIS profiles suggest that when electrons are excited to these states, they delocalize in a time comparble or longer than the C 1s corehole decay time, likely due to a remarkable $\pi*$ character. Moreover, in the C 1s NEXAFS spectrum of sample C peak C_A results larger with respect to the corresponding structure of sample A. This can be due either to a change in nature of the first π^* state in the doped molecule, resulting in a lifetime broadening or in a modification of the involed molecular vibrations, or to additional empty states at lower energy than peak C_A. Specifically, in the CIS profile of sample C (Figure 9.9-e, right panel), a new feature, distinct from that at hν = 285.1 eV, is singled out at hν = 284.5 eV (indicated by a black arrow), which would support the hypothesis of new empty states due to K-intercalation. However, the low signal-to-noise ratio of the RSW spectra at this photon energy prevents a further analysis at this stage.

9.2.5 N-related electronic states

In section 9.2.3, an overall change in N 1s NEXAFS spectra of the doped samples with respect the undoped sample has been highlighted. Correspondently, upon intercalation some modifications appear in the N 1s XPS spectrum.

This is shown for N 1s XPS spectrum of sample C in Figure 9.10-b, for which an asymmetric profile at low binding energies is observed compared to N 1s XPS spectrum of sample A (Figure 9.10-a). This is confirmed when spectra are fitted with gaussian functions, after a Shirley background substraction. While the fit of spectrum (a) consists of only one gaussian, spectrum (b) requires to introduce a second component at lower binding energies. Looking at the fitting parameters (displayed in Figure 9.10), the position of the maximum and the FWMH of component 1 in spectrum (b) are very close

to the corresponding paramenters of the single component in spectrum (a). Thus, component 1 can be assigned to eumelanin macromolecules that are not interacting with potassium through N atoms. On the contrary, component 2 is ascribed to eumelanin molecules whose N atoms binds to K ions. It is worth noting that the ratio of the area of the 2 components ($Area_1/Area_2 = 6$) suggests that, for one part of eumelanin in which K ions bind to N atoms, six part are interacting with K ions through other atoms or are not interacting at all.

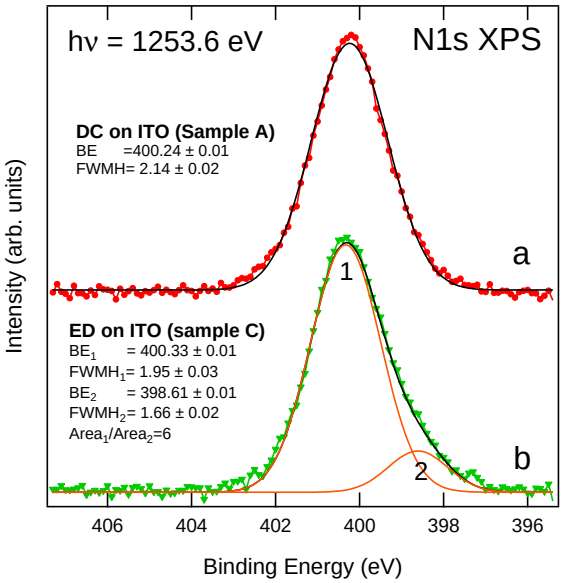

Figure 9.10: N 1s XPS spectra of sample A (a) and sample C (b) collected at hν = 1253.6 eV.

The possibility of alternative binding sites to N atoms has already been suggested by estimating the quantity of K ions in the macromolecule (N : K = 1 : 0.6) which exceeds that expected if K ions interacted only with macrocycle (1 : 0.25). Indeed, the analysis of N 1s XPS spectra further restricts the role of N atoms in the interaction with K ions. However, it should be reminded that modifications in spectra obtained with X-ray photoemission and absorption spectroscopy (which are local probes) such as those seen for N 1s XPS and N 1s NEXAFS spectra still support the hypothesis of imine group as one (but not the sole) of the possibile interaction sites for potassium.

A further confirmation to this assumption is given by comparing the calculated N 1s NEXAFS spectrum of K-IHHH protomolecules with experimental spectra colleted at polarization angle of $\theta = 60°$. In Figure 9.11, the calculated N 1s NEXAFS spectrum for K-IHHH is shown (a) along with that of

IHHH, which are aligned according to the analysis reported in Chapter 7.3.3 for the IHHH tetramer. It can be observed that the LUMO of K-IHHH is shifted by 2.43 eV to the lower energies with respect to the LUMO of IHHH, while the intense peak LUMO+3 of K-IHHH is about at the same energy as the LUMO of IHHH.

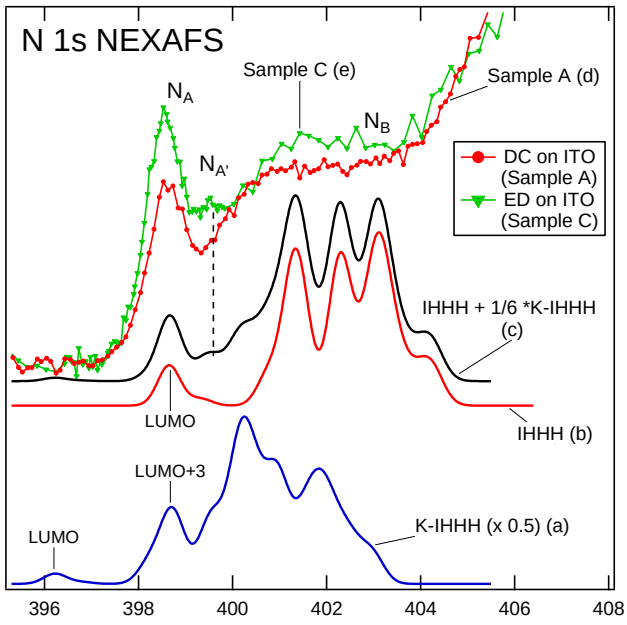

Figure 9.11: Calculated N 1*s* NEXAFS spectra of the K-IHHH (a) and IHHH (b) tetramer, along with a linear combination of the two (c), where K-IHHH weight one sixth. Experimental N 1*s* NEXAFS spectra, colleted at polarization angle of $\theta = 60°$, of sample A (d) and sample C (e) are also shown.

According to the fit of N 1*s* XPS spectra, for one part of eumelanin in which K ions bind to N atoms, six part are interacting with K ions through other atoms or are not interacting at all. Therefore, we compare the experimental data of sample C (Figure 9.11,e) with a $1:6$ linear combination of the calculated spectra of K-IHHH and IHHH (Figure 9.11-c and -d, respectively). It should be reminded that, as already assessed in Chapter 7.3.3, the calculated NEXAFS spectrum of IHHH presents an overall agreement with the experimental spectrum of sample A. Indeed, in the linear combination, while the LUMO coming form K-IHHH is quite unobservable, as expected from the experimental data, new features appear in correspondence of the photon energies of the experimental peak N'_A (as indicated by dashed line) which are not present in calculated IHHH spectrum (b). On the other hand, it is clear that peak N'_A is not detected in the experimenatal spectrum of sample

A (d). Besides, this linear combination would explain the increased intensity of peak N_A as well as of N_B shoulder, which is observed in the experimental spectrum of the doped sample (e). Therefore, K-IHHH tetramer can account for modifications observed upon K-intercalation in the N 1s NEXAFS spectra of sample C (and consequently of sample B). However, the 1 : 6 ratio, along with the stechiometric experimental N : K ratio (1 : 0.6), suggests the presence of other binding sites for K atoms in addition to the center of the ring.

9.3 Conclusions

In this Chapter, eumelanin films electrodeposited on ITO substrates are selected for studying the effects of potassium ions on the electronics properties of eumealnin. These films have been shown to exhibite a preferential orientation of the molecular plane throught the surface as well as changes in the valence band structure and nitrogen-related experimental data upon K-intercalation. Starting from the model protomolecules of IHHH and IQIQ introduced in Chapter 7, we have found that the favoured configuration for the K ion with respect to the nitrogen-containing macrocycle is when the K ion is 2 Å far from the molecular plane, leaving two hydrogen atoms in the ring. Moreover, a greater stability of the K ion is achieved in the IHHH tetramer compared to IQIQ tetramer. The calculated DOS of this configuration, named K-IHHH, revealed the presence of additional occupied electronic states at low binding energies compared to the undoped case, as also confirmed by experimental valence band spectra. New unoccupied orbitals located on carbon atoms are also observed in resonant photoemission experiment on C K-edge. By estimating the quantity of potassium in the samples, the possibility of additional binding sites to N atoms for K ions is proposed. Furthermore, N 1s XPS spectrum revealed that the imine groups are far from being saturated by the K binding, yet they still play a role in the K doping, as confirmed by comparing the experimental N 1s NEXAFS spectrum to the calculated spectrum of the proposed K-IHHH tetramer.

Chapter 10

Conclusions

In the present work, the structural and electronic properties of two self-assembling organic systems, namely the porphyrins and the eumelanin, have been studied.

Porphyrin monolayers have been produced in UHV by sublimating multilayers pre-deposited on single crystal substrates in the range of 520-570 K. The molecular orientation has been determined with angle resolved X-ray absorption near atomic edges (NEXAFS), while the strength of the interaction with the substrate has been traced with X-ray photoemission spectroscopy (XPS) and, in some case, Resonant photoemission spectroscopy (ResPES) on C K-edge.

The adsorption orientation and the electronic properties of ZnTPP molecules critically depends on the chosen substrate, highlighting the versatility of porphyrin in providing different self-assembled nanostructered organic/inorganic interfaces. On a metal substrate such as Ag(110), ZnTPP molecules is adsorbed with both the phenyl rings and the macrocycle flat on the surface. A partial filling of the LUMO of the pristine molecule is evidenced in VB spectra and primarly involved the electronic states in the macrocycle, as indicated by ResPES measurements. The possibile metallization of the molecular overlayer is also supported by the core level fit of both C 1s and N 1s, which requires the use of a DS lineshape with an asymmetry parameter (singularity index) of 0.10 ± 0.01. A different arrangement and interaction are found for Si(111). The macrocycle plane of the molecules is adsorbed with an average angle of $15 \pm 5^{\circ}$. The ResPES behaviour indicates that for the phenyl rings the charge transfer into the substrate is less favorable than in the Ag(110) case and comparable to the multilayer case. Core-level photoemission indicates that the molecule is interacting with the substrate using a macrocycle pyrrole ring, while the phenyl rings are rotated in such a way that it minimizes the interaction with the substrate.

Up to now, only indirect methods such as STM images and the relative density functional theory (DFT) simulation of the STM images have been employed to determine the adsorpion configuration of 2H-TPP molecules on Ag(111) [51, 66, 67, 68, 72, 149]. According to these techniques, 2H-TPP molecules on Ag(111) have the phenyl ring surfaces rotated with respect to the macrocycle.
In the present study, however, the adsorpion geometry of a 2H-TPP monolayer on Ag(111) has been analysed for the first time with a direct method, i.e. polarization dependance of NEXAFS spectra. In contrast with STM images results, the conformation with both the macrocycle and the phenyls flat on the surface is observed for 2H-TPP molecules on Ag(111). The flat rotation of the phenyls is demostrated to be crucially determined by the annealing at 550 K, which is the method that allows the thermal desorption of the pre-deposeted multilayer to obtained the monolayer. DFT and molecular dynamics calculations suggest a possible molecular reaction of porphyrins to explain this adsorption conformation: the de-hydrogenation of eight carbon atoms in the remaining monolayer after the multilayer desorption, with the formation of four new aryl-aryl carbon bonds. The chemical reaction produces a more stable molecule that forms a patterned square lattice on the Ag(111) and that can be eventually further modified by the introduction of the central metal atoms.

The Fe metalation of both monolayer and multilayer (about 4 ML) of 2H-TPP on Ag(111) has been successfully reproduced in UHV by following an already known recipe [68]. In the present thesis, however, new insights on the model of the molecular structural configuration onto the substrate surface have been provided as well as an extensive characterization of the electronic states before and after the metalation. The study of the monolayer case showed a metallic behaviour for the film, as confirmed by the analysis of the VB spectrum at the Fermi edge during the Fe deposition and by the XPS fitting functions that have required the introduction of an asymmetry. In particular, the metallic state of the monolayer evolves with Fe complexation due to Fe *d*-states hybridization with the *sp*-bands of the substrate. From polarization dependance of NEXAFS spectra at N 1s and C 1s thresholds, the influence of the Fe metallic centre in the porphyrin core is observed to have only minor effects in the monolayer adsorption configuration, probably due the conformation of phenyl legs which reduces the degrees of freedom of the macrocycle towards the already reached lowest energy situation. In contrast, in multilayers, which has the non-flat orientation of the phenyls, the Fe metalation of the 2H-TPP molecules favours a macrocycle saddle shape. Moreover, both core level and valence band photoemission results have given evidence that the charge injection from the substrate is more likely confined

to the first layer.

The Fe metalation of both monolayer and multilayer (about 4 ML) of octaethyl-porphyrin molecules (2H-OEP) on Ag(111) has been successfully reproduced for the first time in UHV. The present study evidences that, under equivalent experimental conditions, Fe metalation is accomplished in both 2H-TPP and 2H-OEP deposited on Ag(111) with comparable characteristics, with the charge injection from the substrate to the molecular film that is more likely confined to the first monolayer. In contrast, the 2H-OEP molecular plane in monolayer is observed to be tilted with respect the surface plane to optimize steric hindrance, which is likely to be mastered by lateral groups, as also suggested by 2H-OEP monolayer simulations [125]. In addition, the macrocycles occur to be further tilted with respect the surface plane in 2H-OEP multilayer packing, along with possible chemical modification of the iminic groups.

The informations obtained from the experiments on porphyrins presented here indicates that the selected substrate and the interfacial behaviour are important for the controlled self-assembly of ordered nanostructures such as porphyrins, and offers a number of powerful approaches to tailor the behaviour of porphyrin-based devices.

While the basic molecular unit of porphyrins is well known and can be easily controlled in the nanostructure self-assembling, the basic molecular building block of eumelanin has not been isolated yet, leading to a great uncertainty about its chemical composition. This is in part due to the fact that melanins are difficult molecules to study because they are chemically and photochemically stable, they are virtually insoluble in most common solvents and are unlikely to be evaporated in UHV without structural damage [92]. Therefore, the first goal of this study has been the production of continuous thin films suitable for a detailed spectroscopic characterization in UHV conditions. The films have been prepared by drop casting from a solution of synthetic eumelanin powders in dimethyl sulfoxide (DMSO) and can be regarded as reference samples for the study of eumelanin in condensed phase. The comparison of the calculated DOS of monomers and some model protomolecules with the valence band and X-ray absorption spectra of thin film of eumelanin revealed that a model tetramer composed of three HQ and one IQ is the minimum supramolecular level of organization that can provide a consistent spectroscopical picture of an altogether complex and highly disordered system.

The addition of potassium ions to the eumelanin compound has profound effects on eumelanin morphology at a microscopic scale as well as on the electronic structure. Atomic force microscopy (AFM) images show that eumelanin films produced from a starting solution containing KBr are con-

stituted of spherical particles of about 50 nm in diameter that exhibite the tendency of a progressive build-up toward larger structures. The hierarchical organization displayed by synthetic K-doped eumelanin is absent in the synthetic undoped sample but it is very similar to the self-assembly behaviour observed in the natural compound - which is naturally synthetized in a saline enviroment - suggesting the fundamental role of metal ions in eumelanin aggregation.

AFM, X-ray diffraction and polarization dependent NEXAFS measurements have disclosed that electrochemical deposition is a controlled way to introduce K ions in eumelanin sample while improving the inner film order. The K-doping strongly affects also the electronic properties of eumelanin oligomer. XPS and ResPES spectra revealed the presence of additional occupied electronic states at low binding energies compared to the undoped case, while new unoccupied orbitals have been induced by analysing NEXAFS spectra and CIS profile. These experimental evidences may be reproduced by calculations on K-doped IHHH tetramer, for which the favoured configuration is the K ion is 2 Åfar from the nitrogen-containing macrocycle. The possibility of additional binding sites to N atoms for K ions is proposed.

Appendix A

Modelling the peak shapes

Energy (E) distribution curves in photoelectron spectroscopy may be theoretically characterized by spectral functions, which take into account all the possible excitation processes in the sample of interest [191]. In the majority of cases these spectral functions may be represented by a set of peaks, e.g. main line and satellites, multiplets, doublets or even single lines. The peak shapes are typically determined by a Lorentzian contribution due to the limited lifetime of the core hole state and a Gaussian broadening, mostly due to incoming radiation and the measurement process in the spectrometer. Gaussian contributions may also be related to thermal (phonon) excitation processes [192]. Chemical, structural, and electronic (by dopants) inhomogeneities in the surroundings of the emitting atoms often also contribute to Gaussian broadening. Both the area-nomalized Lorentzian function $L(E)$

$$L(E) = \frac{2}{\beta\pi} \cdot \left\{ 1 + \left[\frac{E - E_0}{\beta} \right]^2 \right\}^{-1} \tag{A.1}$$

and the area-nomalized Gaussian function $G(E)$

$$G(E) = \frac{1}{2\sqrt{2\pi\beta}} \cdot \exp\left\{ -\ln 2 \cdot \left[\frac{E - E_0}{\beta} \right]^2 \right\} \tag{A.2}$$

are completely characterized by the peak parameters β, corresponding to 1/2 of the full width at half maximum (FWHM), and E_0, the peak position.

In photoemission process, a fast photoelectron with energy well above the conduction band is produced. In metals, because the sceening process, the positive photohole creates electron-hole pairs in the Fermi sea of conduction electrons. This is an intrinsic process, and the intrinsic lineshape is given by

the asymmetric Doniach-Sunjic (DS) lineshape [146]:

$$DS(E) = \beta \cdot \frac{\cos\left\{\pi\frac{\alpha}{2} + (1-\alpha)\arctan\left[\frac{E-E_0}{\beta}\right]\right\}}{[(E-E_0)^2+\beta^2]^{\frac{1-\alpha}{2}}} \tag{A.3}$$

This function may describe low-energy tails of the peaks, which are determined by the values of the so-called asymmetry parameter α. As α increases, the peak of the line moves from the energy of the unscreened transition toward greater BE, i.e., from the position that the peak would have if α were zero. Thus, for very accurate binding energy measurements (to within 0.05 eV), the singularity index must be accurately determined. Notice that the Doniach-Sunjic peak shape transforms into a Lorentzian in the limit of $\alpha \to 0$.

An adequate approach to describe XPS core level lines is the description of the peaks as the convolution of independent Gaussian and Lorentzian (or Doniach-Sunjic type) contributions, namely the Voigt profile [193]. This profile function and the corresponding derivatives with respect to the parameters have to be evaluated numerically, which makes the minimization process more time-consuming.

A faster convergence of the iterative process returning good results, however, can be frequently obtained by the simple product of independent Gaussian and Lorentzian (or Doniach-Sunjic type) contributions [193]. The latter is the approach chosen in the present thesis for the fitting of core-level photoemission spectra.

Appendix B

List of papers

The present thesis is based on the following papers:

Chapter 3

- C. Castellarin-Cudia, P. Borghetti, G. Di Santo, M. Fanetti, R. Larciprete, C. Cepek, P. Vilmercati, L. Sangaletti, A. Verdini, A. Cossaro, L. Floreano, A. Morgante and A. Goldoni: *Substrate influence for the Zn-tetraphenyl-porphyrin adsorption geometry and the interface-induced electron Transfer*, ChemPhysChem **11** (2009) 2248.

Chapter 4

- G. Di Santo, S. Blankenburg, C. Castellarin-Cudia, M. Fanetti, P. Borghetti, L. Sangaletti, L. Floreano, D. Passerone and A. Goldoni: *Chemical modification of 2H-tetraphenyl-porphyrin on Ag(111): carbon de-hydrogenation and flat conformation*, submitted to NanoLetters (2010).

Chapter 5

- G. Di Santo, P. Borghetti, C. Castellarin-Cudia, M. Fanetti, B. Taleatu, L. Sangaletti, L. Floreano, E. Magnano, F. Bondino and A. Goldoni: *Conformational adaptation and electronic structure of 2H-tetraphenyl-porphyrin on Ag(111) during Fe metalation*, submitted to J. Phys. Chem. (2010).

Chapter 6

- P. Borghetti, G. Di Santo, C. Castellarin-Cudia, M. Fanetti, L. Sangaletti, E. Magnano, F. Bondino and A. Goldoni *Direct Fe metalation of 2H-octaethyl-porphyrin on Ag(111): electronic states and conformational adaptation*, in manuscript.

- M. Fanetti, P. Vilmercati, C. Castellarin-Cudia, P. Borghetti, A. Goldoni, S. Modesti, A. Calzolari and S. Fabris: *Structure and molecule-substrate interaction in a Cobalt octaethyl-porphyrin monolayer on the Ag(110) surface*, in manuscript.

Chapter 7

- L. Sangaletti, P. Borghetti, P. Ghosh, S. Pagliara, P. Vilmercati, C. Castellarin-Cudia, L. Floreano, A. Cossaro, A. Verdini, R. Gebauer and A. Goldoni: *Polymerization effects and localized electronic states in condensed-phase eumelanin*, Phys. Rev. B **80** (2009) 174203.

Chapter 8

- P. Borghetti, A. Goldoni, C. Castellarin-Cudia, L. Casalis, F. Herberg, L. Floreano, A. Cossaro, A. Verdini, R. Gebauer, P. Ghosh and L. Sangaletti: *Effects of potassium on the supramolecular structure and electronic properties of eumelanin thin films*, Langmuir (in press).

Chapter 9

- P. Borghetti, P. Ghosh, A. Goldoni, C. Castellarin-Cudia, G. Drera, L. Floreano, A. Cossaro, A. Verdini, R. Gebauer and L. Sangaletti: *Electronic states in nanostructured K-doped euelanin films on ITO: theory and experiments*, in manuscript.

Acknowledgments

I want to express all my gratitude to the people that have contributed to the work presented in this thesis.

Above of all, I am profoundly grateful to my tutor prof. Luigi Sangaletti, from whom I have learnt most of what I know about this field of physics. During all these years, he has been not only my supervisor but also a good person that guided me through my doubts (and shared with me a lot of fine music!).

I owe special thanks to Dr. Andrea Goldoni for giving me the oppurtunity to work in its group at Elettra Synchrotron in Trieste and for numberless instructive discussions which improved my work. I also would like to thank Carla Castellarin-Cudia and Giovanni Di Santo for the invaluable cooperation at μ-nano-Carbon Laboratory at Elettra (and outside the lab). Special thanks go to Paolo Vilmercati, Alberto Verdini, Luca Floreano, Albano Cossaro for many useful (scientific and not only) reccomandations during my PhD studentship.

I wish to express my gratitude to Emilia, Maya, Marina, Silvia, the wide community of "Brescia people" and the other special persons I met in Trieste, which made the period I spent there such an enjoyable and unforgettable time.

A considerable part of my work time at Surface Science Laboratory in Università Cattolica (Brescia) was shared with Giovanni Drera. Thank you for being such a funny and good friend and for helping me in my "patacche" experimental issues.

Last years have been so important in my life. I have realized how lucky I am in being surrounded by so many extraordinary friends. You are too many to be cited all, but I hope that I'll be able to express my thankfulnees in our everyday friendship. Thanks to my long standing (and patient) friends, to the new friends I've recently found and to all who will stay by my side whatever road I will take.

Last, but not least, I would like to say thank you to my parents, my sister Michela and to the rest of my family for their invaluable support.

Bibliography

[1] J. V. Barth, G. Costantini, and K. Kern, Nature **437**, 671 (2005).

[2] G. M. Whitesides and B. Grzybowski, Science **295**, 2418 (2002).

[3] N. R. Armstrong, J. Porphyrins Phthalocyanines **4**, 414 (1999).

[4] J. M. Lehn, Science **295**, 2400 (2002).

[5] S. Oliver, N. Coombs, A. Kuperman, A. Lough, and G. A. Ozin, Nature **378**, 47 (1995).

[6] C. Fouquey, J. M. Lehn, and A. M. Levelut, Adv. Mater. **2**, 254 (1990).

[7] P. Jourdan, P. Fromme, H. T. Witt, O. Klukas, W. Saenger, and N. Krauss, Nature **411**, 909 (2001).

[8] M. Ruben, J. M. Lehn, and G. Vaughan, Chem. Commun. 1338 (2003).

[9] O. Waldmann, J. Hassmann, P. Müller, G. S. Hanan, D. Volkmer, U. S. Schubert, and J. Lehn, Phys. Rev. Lett. **78**, 3390 (1997).

[10] M. L. Wolbarsht, A. W. Wash, and G. George, Appl. Opt. **20**, 2184 (1981).

[11] M. M. Jastrzebska, H. Isotalo, J. Paloheimo, and H. Stub, J. Biomater. Sci. Polymer Edn. **7**, 557 (1995).

[12] T. Sarna, B. Pilas, E. J. Land, and T. G. Truscott, Biochim. Biophys. Acta **883**, 162 (1986).

[13] G. W. Zajac, J. Gallas, J. Cheng, M. Eisner, S. C. Moss, and A. E. Alvarado-Swaisgood, Biochim. Biophys. Acta **1199**, 271 (1994).

[14] J. M. Gallas, K. C. Littrell, S. Seifert, G. W. Zajac, and P. Thiyagarajan, Biophys. J. **77**, 1135 (1999).

[15] P. Diaz, Y. Gimeno, P. Carro, S. Gonzalez, P. L. Schilardi, G. Benitez, R. C. Salvarezza, and A. H. Creus, Langmuir **21**, 5924 (2005).

[16] C. M. R. Clancy and J. D. Simon, Biochemistry **40**, 13353 (2001).

[17] J. Cheng, S. C. Moss, M. Eisner, and P. Zcshack, Pigment Cell Res. **7**, 263 (1994).

[18] A. Napolitano, A. Pezzella, M. d'Ischia, G. Prota, R. Seraglia, and P. Traldi, Rapid Comm. Mass Spectrom. **10**, 468 (1996).

[19] A. Pezzella, M. d'Ischia, A. Napolitano, R. Seraglia, P. Traldi, and G. Prota, Rapid Comm. Mass Spectrom. **11**, 368 (1997).

[20] J. B. Nofsinger, S. E. Forest, L. M. Eibest, K. A. Gold, and J. D. Simon, Pigment Cell Res. **13**, 179 (2000).

[21] T. S. Balaban, Acc. Chem. Res. **38**, 612 (2005).

[22] J. Falk, *Porphyrins and Metalloporphyrins* (Elsevier, 1975).

[23] W. Kaim and B. Schwederski, Acc. Chem. Res. **38**, 612 (2005).

[24] R. S. Czernuszewicz, J. Porphyrins Phthalocyanines **4**, 426 (2000).

[25] I. Scalise and E. N. Durantini, J. Photochem. Photobiol. A **162**, 105 (2004).

[26] C. Castellarin-Cudia *et al.*, Surf. Sci. **600**, 4013 (2006).

[27] D. Monti, S. Nardis, M. Stefanelli, R. Paolesse, C. D. Natale, and A. D'Amico, J. Sensors **2009**, 1 (2009).

[28] R. J. D. Miller, *Surface Electron Transfer Processes* (VCH Publishers, 1995).

[29] J. Yang, J. Zhang, D. Wang, Y. Bai, H. Sun, D. Shen, and T. Li, J. Photochem. Photobiol. A **112**, 225 (1998).

[30] P. Vilmercati *et al.*, Surf. Sci. **600**, 4018 (2006).

[31] T. Okajimaa, Y. Yamamoto, Y. Ouchi, and K. Seki, J. Electron Spectr. Rel. Phenom. **114**, 849 (2001).

[32] A. Scheybal, T. Ramsvik, R. Bertschinger, M. Putero, F. Nolting, and T. A. Jung, Chem. Phys. Lett. **411**, 214 (2005).

[33] H. Wende *et al.*, Nature Materials **6**, 516 (2007).

[34] J. Manono, P. A. Marzilli, and L. G. Marzilli, Inorg. Chem. **48**, 5636 (2009).

[35] J. Li, A. Ambroise, S. I. Yang, J. R. Diers, J. Seth, C. R. Wack, D. F. Bocian, D. Holten, and J. S. Lindsey, J. Am. Chem. Soc. **121**, 8927 (1999).

[36] S. R. Forrest, Chem. Rev. **97**, 1793 (1997).

[37] H. E. Katz, J. Mater. Chem **7**, 1793 (1997).

[38] S. Sun and N. S. Sariciftci, *Organic Photovoltaics: Mechanism, Materials and Devices* (ed. Taylor and Francis, 2005).

[39] G. Witte and C. Wöll, Phys. Stat. Solidi A **205**, 497 (2008).

[40] C. Wöll, *Physical and Chemical Aspects of Organic Electronics* (WILEY-VCH Verlag Gmbh, 2009).

[41] K. M. Kadish, K. Smith, and R. Gillard, *The Porphyrin Handbook* (Academic, 2000).

[42] A. K. Burrel and M. R. Wasielewski, J. Porphyrins Phthalocyanines **4**, 401 (2000).

[43] H. Liu, X. S. Feng, Q. B. Xue, L. Wang, and K. Z. Yang, Thin Solid Films **340**, 265 (1999).

[44] R. Beswick and C. Pitt, J. Colloid Interf. Sci. **124**, 146 (1988).

[45] A. Ruaudel-Teixier and A. Barraud, Thin Solid Films **99**, 33 (1983).

[46] A. Desormeaux, M. Ringuet, and R. Leblanc, J. Colloid Interf. Sci. **147**, 57 (1991).

[47] J. Stöhr, *NEXAFS Spectroscopy* (Springer, 1992).

[48] J. Åhlund, K. Nilson, L. K. J. Schiessling, S. B. ans N. Mårtensson, C. Puglia, B. Brena, M. Nyberg, and Y. Luo, J. Chem. Phys. **125**, 34709 (2006).

[49] L. Floreano, A. Cossaro, R. Gotter, A. Verdini, G. Bavdek, F. Evangelista, A. Ruocco, A. Morgante, and D. Cvetko, J. Chem. Phys. **112**, 10794 (2008).

[50] K. K. Okudaira, H. Setoyama, H. Yagi, K. Mase, S. Kera, A. Kahn, and N. Ueno, J. Electron Spectr. Rel. Phenom. **137**, 137 (2004).

[51] F. Buchner, K. Flechtner, Y. Bai, E. Zillner, I. Kellner, H. Steinrück, H. Marbach, and J. M. Gottfried, J. Phys. Condensed Matter **112**, 15458 (2008).

[52] N. Nishimura, M. Ooi, K. Shimazu, H. Fujii, and K. Uosaki, J. Electroanalytical Chemistry **473**, 75 (1999).

[53] G. Bussetti, C. Corradini, C. Goletti, P. Chiaradia, M. Russo, R. Paolesse, C. D. Natale, A. D'Amico, and L. Valli, Phys. Stat. Solidi B **13**, 2714 (2005).

[54] A. Ishida and T. Majima, Nanotechnology **10**, 308 (1999).

[55] K. Sakakibara and F. Nakatsubo, Cellulose **15**, 825 (2008).

[56] P. A. Brühwiler, O. Karis, and N. Mårtensson, Rev. Mod. Phys. **74**, 703 (2002).

[57] N. C. Maiti, S. Mazumdar, and N. Periasamy, J. Phys. C **99**, 10708 (1995).

[58] A. V. Zamyatin, A. V. Gusev, and M. A. J. Rodgers, J. Am. Chem. Soc. **126**, 15934 (2004).

[59] M. P. de Jong, R. Friedlein, S. L. Sorensen, G. Öhrwall, W. Osikowicz, C. Tengsted, S. K. M. Jönsson, M. Fahlman, and W. R. Salaneck, Phys. Rev. B **72**, 035448 (2005).

[60] L. Scudiero, D. E. Barlow, U. Mazur, and K. Hipps, J. Am. Chem. Soc. **123**, 4073 (2001).

[61] Z. Sun, Y. She, and R. Zhong, Front Chem. Eng. China **3**, 457 (2009).

[62] E. Baciocchi, O. Lanzalunga, A. Lapi, and L. Manduchi, J. Am. Chem. Soc. **120**, 5783 (1998).

[63] D. Wœhrle, J. Porphyrins Phthalocyanines **4**, 418 (2000).

[64] P. Gambardella *et al.*, Nature Materials **8**, 189 (2009).

[65] F. J. Williams, O. P. H. Vaughan, K. J. Knox, N. Bampos, and R. M. Lambert, Chem. Commun. **44**, 1688 (2004).

[66] F. Buchner, V. Schwald, K. Cornanici, H.-P. Steinrüch, and H. Marbach, ChemPhysChem **8**, 241 (2007).

[67] A. M. M. Kretschmann, M. Walz, K. Flechtner, H. P. Steinrück, and J. M. Gottfried, Chem. Commun. 568 (2007).

[68] J. M. Gottfried, K. Flechtner, A. M. M. Kretschmann, T. Lukasczyk, and H. P. Steinrück, J. Am. Chem. Soc. **128**, 5644 (2006).

[69] Y. Bai, F. Buchner, M. Wendahl, I. Kellner, A. Bayer, H. P. Steinrück, H. Marbach, and J. M. Gottfried, J. Phys. Condensed Matter **112**, 6087 (2008).

[70] S. Fukuzumi, J. Porphyrins Phthalocyanines **4**, 398 (2000).

[71] T. E. Shubina, H. Marbach, K. Flechtner, A. M. M. Kretschmann, N. Jux, F. Buchner, H. P. Steinrück, T. Clark, and J. M. Gottfried, J. Am. Chem. Soc. **129**, 9476 (2007).

[72] T. Lukasczyk, K. Flechtner, L. Merte, N. Jux, F. Maier, J. M. Gottfried, and H. P. Steinrück, J. Phys. Condensed Matter **111**, 3090 (2007).

[73] W. Auwärter, A. Weber-Bargioni, S. Brink, A. Riemann, A. Schiffrin, M. Ruben, and J. V. Barth, ChemPhysChem **8**, 250 (2007).

[74] R. A. Nicolaus, *Melanin* (Hermann, 1968).

[75] M. H. Van-Woert and L. M. Ambani, Adv. Neurol. **5**, 215 (1974).

[76] N. Kollias, R. M. Sayer, L. Zeise, and M. R. Chedekel, J. Photochem. Photobiol. B: Biol **9**, 135 (1991).

[77] P. Meredith, J. Riesz, B. J. Powell, S. P. Nighswander-Rampel, M. R. Pederson, and E. G. Moore, Soft Matter **2**, 37 (2006).

[78] S. E. Forest and J. D. Simon, Photoch. Photobiol. **68**, 296 (1998).

[79] P. Meredith and J. Riesz, Photoch. Photobiol. **79**, 211 (2004).

[80] J. Riesz, J. Gilmore, and P. Meredith, Biophys. J. **90**, 1 (2006).

[81] T. Ye and J. D. Simon, J. Phys. Chem. B **107**, 11240 (2003).

[82] J. McGinness, P. Corry, and P. Proctor, J. Appl. Phys. **183**, 853 (1974).

[83] P. Meredith, J. Riesz, B. J. Powell, R. Vogel, D. Blake, S. Subianto, G. Will, and I. Katrini, *Broad band photon-harvesting biomolecules for photovoltaics. In Artificial Photosynthesis: From Basic Biology to Industrial Application* (Wiley, 2005).

[84] P. Meredith and T. Sarna, Pigment Cell Res. **16**, 572 (2006).

[85] M. A. Rosei, L. Mosca, and F. Galluzzi, Syn. Met. **76**, 331 (1996).

[86] M. M. Jastrzebska, A. Kocot, and L. Tajber, J. Photochem. Photobiol. B: Biol **66**, 201 (2002).

[87] G. Albanese, M. G. Bridelli, and A. Deriu, Biopolymers **23**, 1481 (1984).

[88] M. G. Bridelli, R. Capelletti, and P. R. Crippa, Physiol. Chem. Phys. **12**, 233 (1980).

[89] H. Z. Hill and G. J. Hill, Pigment Cell Res. **1**, 163 (1987).

[90] C. G. Burkhart and C. N. Burkhart, Intern. J. Derm. **44**, 340 (2005).

[91] F. A. Zucca *et al.*, Pigment Cell Res. **17**, 610 (2004).

[92] Y. Liu and J. D. Simon, Pigment Cell Res. **16**, 606 (2003).

[93] S. Ito, Biochim. Biophys. Acta **883**, 155 (1986).

[94] C. Lambert, J. N. Chacon, M. R. Chedekel, E. J. Land, P. A. Riley, A. Thompson, and T. G. Truscott, Biochim. Biophys. Acta **993**, 12 (1989).

[95] E. Kaxiras, A. Tsolakidis, G. Zonios, and S. Meng, Phys. Rev. Lett. **97**, 218102 (2006).

[96] K. B. Stark, J. M. Gallas, G. W. Zajac, M. Eisner, and J. T. Golab, J. Phys. Chem. B **107**, 11558 (2003).

[97] S. P. Nighswander-Rempel, I. B. Mahadevan, P. V. Bernhardt, J. Butcher, and P. Meredith, Photoch. Photobiol. **84**, 620 (2008).

[98] B. J. Powell, T. Baruah, N. Bernstein, K. Brake, R. H. Mckenzie, P. Meredith, and M. R. Pederson, J. Chem. Phys. **120**, 8608 (2004).

[99] B. J. Powell, Chem. Phys. Lett. **402**, 111 (2005).

[100] Y. Liu, L. Hong, V. R. Kempf, K. Wakamatsu, S. Ito, and J. D. Simon, Pigment Cell Res. **17**, 262 (2004).

[101] L. Sangaletti, S. Pagliara, P. Vilmercati, C. Castellarin-Cudia, P. Borghetti, P. Galinetto, R. Gebauer, and A. Goldoni, J. Phys. Chem. B **111**, 5372 (2007).

[102] R. C. Sealy, J. S. Hyde, C. C. Felix, L. A. Menon, and G. Prota, Science **217**, 545 (1982).

[103] L.Zeise, M. R. Chedekel, and T. B. Fitzpatrick, *Melanin: its role in human protection* (Valdenmar Publishing, 1995).

[104] G. Prota, *Melanins and Melanogenesis* (Academic Press, 1992).

[105] L. Hong and J. D. Simon, J. Phys. Chem. B **111**, 7938 (2007).

[106] L. Hong and J. D. Simon, Photoch. Photobiol. **82**, 1265 (2006).

[107] B. Szpoganicz, S. Gidanian, P. Kong, and P. Farmer, J. Inorg. Biochem. **89**, 45 (2002).

[108] Y. Liu and J. D. Simon, Pigment Cell Res. **18**, 42 (2005).

[109] A. G. Orive *et al.*, Chem. Eur. J. **13**, 473 (2007).

[110] L. Sangaletti *et al.*, Phys. Rev. B **80**, 174203 (2009).

[111] J. D. Jackson, *Classical Electrodynamics* (Wiley, 1962).

[112] U. Fano and J. W. Cooper, Rev. Mod. Phys. **40**, 441 (1968).

[113] A. Zajac and E. Hecht, *Optics* (Addison-Welsey, 1974).

[114] V. Coropceanu, J. Cornil, D. A. da Silva Filho, Y. Olivier, R. Silbey, and J. L. Bredas, Chem. Rev. **107**, 926 (2007).

[115] D. Menzel, Chem. Soc. Rev. **37**, 2212 (2008).

[116] P. Vilmercati, D. Cvetko, A. Cossaro, and A. Morgante, Surf. Sci. **603**, 1542 (2009).

[117] M. O. Krause, J. Phys. Chem. Ref. Data **8**, 307 (1979).

[118] M. Weinelt, A. Nilsson, M. Magnuson, T. Wiell, N. Wassdahl, O. Karis, A. Föhlisch, and N. Mårtensson, Phys. Rev. Lett. **78**, 967 (1997).

[119] Y. Luo, H. Ågren, J. Guo, P. Skytt, N. Wassdahl, and J. Nordgren, Phys. Rev. A **52**, 3730 (1995).

[120] J. Schnadt *et al.*, Nature **418**, 620 (2002).

[121] M. Coville and T. D. Thomas, Phys. Rev. A **43**, 6053 (1991).

[122] Z. W. Gortel and D. Menzel, Phys. Rev. B **64**, 115416 (2001).

[123] F. Gel'mukhanov and H. Ågren, Phys. Rev. **312**, 115416 (1999).

[124] V. S. Y. Lin, S. G. D. Magno, and M. J. Therien, Science **264**, 1105 (1994).

[125] M. Fanetti, P. Vilmercati, C. Castellarin-Cudia, P. Borghetti, A. Goldoni, S. Modesti, A. Calzolari, and S. Fabris, The structure and the molecule-substrate interaction in a Co-octaethyl Porphyrin monolayer on the Ag(110) surface *(in preparation)*.

[126] M. P. Byrn, C. J. Curtis, Y. Hsiou, S. I. Khan, P. A. Sawin, S. K. Tendick, A. Terzis, and C. E. Strouse, J. Am. Chem. Soc. **115**, 9480 (1993).

[127] D. K. Sarkar, X. J. Zhou, A. Tannous, M. Louie, and K. T. Leung, Solid State Commun. **125**, 365 (2003).

[128] H. L. Anderson, Chem. Commun. 2323 (1999).

[129] D. A. Fletcher, R. F. McMeeking, and D. Parkin, J.Chem. Inf. Comput. Sci **36**, 746 (1996).

[130] R. W. Wagner, T. E. Johnson, and J. S. Lindsey, J. Am. Chem. Soc. **118**, 11166 (1996).

[131] G. Polzonetti, private communication.

[132] S. Narioka, H. Ishii, Y. Ouchi, T. Yokoyama, T. Ohta, , and K. Seki, J. Phys. C **99**, 1332 (1995).

[133] F. Moresco, G. Meyer, K. H. Rieder, J. Ping, H. Tang, and C. Joachim, Surf. Sci. **499**, 94 (2002).

[134] M. Eichberger, M. Marschall, J. Reichert, and W. Auwa, Nano Lett. **8**, 4608 (2008).

[135] M. Bernien, X. Xu, J. Miguel, M. Piantek, P. Eckhold, J. Luo, J. Kurde, W. Kuch, and K. Baberschke, Phys. Rev. B **76**, 214406 (2007).

[136] T. Yokoyama, T. Kamikado, S. Yokoyama, and S. Mashiko, J. Chem. Phys. **121**, 11993 (2004).

[137] T. Jung, R. Schlittler, and J. Gimzewski, Nature **386**, 696 (1997).

[138] F. Moresco, G. Meyer, K. H. Rieder, H. Tang, A. Gourdon, and C. Joachim, Phys. Rev. Lett. **87**, 088302 (2001).

[139] S. Lukas, G. Witte, and C. Wöll, Phys. Rev. **88**, 28301 (2002).

[140] Q. Chen, A. J. McDowall, and N. V. Richardson, Langmuir **19**, 10164 (2003).

[141] L. Floreano, A. Cossaro, D. Cvetko, G. Bavdek, and A. Morgante, J. Phys. Chem. B **110**, 4908 (2006).

[142] G. Bavdek, A. Cossaro, D. Cvetko, C. Africh, C. Blasetti, F. Esch, A. Morgante, and L. Floreano, Langmuir **24**, 767 (2008).

[143] T. Shimooka, S. Yoshimoto, M. Wakisaka, J. Inukai, and K. Itaka, Langmuir **19**, 6380 (2003).

[144] M. S. Liao and S. Scheiner, J. Chem. Phys. **117**, 205 (2002).

[145] D. A. Shirley, Phys. Rev. B **55**, 4709 (1972).

[146] S. Doniach and M. Sunjic, J. Phys. C **3**, 285 (1970).

[147] A. Goldoni, R. Larciprete, C. Cepek, C. Masciovecchio, F. E. Melloui, R. Hudej, M. Sancrotti, and G. Paolucci, Surf. Rev. and Lett. **9**, 775 (2002).

[148] J. L. Solomon, R. J. Madix, and J. Stöhr, Surf. Sci. **255**, 12 (1991).

[149] Y. Bai, F. Buchner, I. Kellner, M. Schmid, F. Vollnhals, H. P. Steinrück, and H. M. J. M. Gottfried, New J. Physics **11**, 125004 (2009).

[150] W. Auwärter *et al.*, Phys. Rev. B **81**, 245403 (2010).

[151] http://gwyddion.net/.

[152] J. VandeVondele, M. Krack, F. Mohamed, M. Parrinello, T. Chassing, and J. Hutter, ChemPhysChem **167**, 103 (2005).

[153] J. P. Perdew, K. Burke, and M. Ernzerhof, Phys. Rev. Lett. **77**, 3865 (1996).

[154] S. Goedeker, M. Teter, and J. Hutter, Phys. Rev. B **54**, 1703 (1996).

[155] S. Grimme, Chem. Commun. **27**, 1787 (2006).

[156] C. A. Pignedoli, T. Laino, M. Treier, R. Fasel, and D. Passerone, Eur. Phys J. B **75**, 1434 (2010).

[157] G. Bussi and D. D. M. Parrinello, Eur. Phys J. B **126**, 014101 (2007).

[158] G. Polzonetti, Chem. Phys. **296**, 87 (2004).

[159] L. Floreano *et al.*, Rev. Sci. Instruments **70**, 3855 (1999).

[160] M. Zangrando, M. Zacchigna, M. Finazzi, D.Cocco, R. Rochow, and F. Parmigiani, Rev. Sci. Instruments **75**, 31 (2004).

[161] D. H. Aue, H. M. Webb, and M. T. Bowers, J. Am. Chem. Soc. **97**, 4136 (1975).

[162] B. Johansson and N. Mårtensson, Phys. Rev. B **21**, 4427 (1980).

[163] J. B. Hudson, *Surface Science* (Butterworth-Heinemann, 1992).

[164] S. A. Krasnikov, N. N. Sergeeva, M. M. Brzhezinskaya, A. B. Preobrajenski, Y. N. Sergeeva, N. A. Vinogradov, A. A. Cafolla, M. O. Senge, and A. S. Vinogradov, J. Phys. Condens. Matter **20**, 235207 (2008).

[165] P. Panchmatia, B. Sanyal, and P. Oppeneer, Chem. Phys. **343**, 47 (2008).

[166] D. J. Gardiner, *Practical Raman spectroscopy* (Springer-Verlag, 1989).

[167] R. L. McCreery, *Raman Spectroscopy for Chemical Analysis* (Wiley and Sons, 2000).

[168] Quantum-ESPRESSO is a community project for high-quality quantum-simulation software, based on density-functional theory, and coordinated by Paolo Giannozzi. See http://www.quantum-espresso.org and http://www.pwscf.org.

[169] D. Vanderbilt, Phys. Rev. B **41**, 7892 (1990).

[170] W. Kohn and L. J. Sham, Phys. Rev. **140**, 1133 (1965).

[171] P. E. Blöchl, Phys. Rev. B **50**, 17953 (1994).

[172] B. Hetényi, F. D. Angelis, P. Giannozzi, and R. Car, J. Chem. Phys. **115**, 5791 (2001).

[173] J. C. Slater, Adv. Quantum Chem. **6**, 1 (1972).

[174] J. C. Slater and K. H. Johnsson, Phys. Rev. B **5**, 844 (1972).

[175] J. F. Janak, Phys. Rev. **18**, 7165 (1978).

[176] P. Rez, J. R. Alvarez, and C. Pickard, Ultramicroscopy **78**, 175 (1999).

[177] L. Triguero, L. G. M. Pettersson, and H. Ågren, Phys. Rev. B **58**, 8097 (1998).

[178] R. Buczko, G. Duscher, S. J. Pennycook, and S. T. Pantelides, Phys. Rev. Lett. **85**, 2168 (2000).

[179] B. Hetényi, F. D. Angelis, P. Giannozzi, and R. Car, J. Chem. Phys. **120**, 8632 (2004).

[180] I. Tanaka, H. Araki, M. Yoshiya, T. Mizoguchi, K. Ogasawara, and H. Adachi, Phys. Rev. B **60**, 4944 (1999).

[181] K. Lie, R. Hoier, and R. Brydson, Phys. Rev. B **61**, 1786 (2000).

[182] C. Elsasser and S. Kostlmeier, Ultramicroscopy **86**, 325 (2001).

[183] M. Cavalleri, M. Odelius, A. Nilsson, and L. G. M. Pettersson, J. Chem. Phys. **121**, 10065 (2004).

[184] N. F. Mott and E. A. Davies, *Electronic Process in Non-Crystalline Materials* (Oxford-Clarendon, 1979).

[185] U. Höpfner, H. Hehl, and L. Brehmer, Applied Surf. Sci. **152**, 259 (1999).

[186] C. Nogues and M. Wanunu, Surf. Sci. Lett. **573**, L383 (2004).

[187] M. P. Seah, G. C. Smith, and M. T. Anthony, Surf. and Interf. Anal. **15**, 293 (1990).

[188] M. S. Dresselhaus and G. Dresselhaus, Advances in Physics **30**, 139 (1981).

[189] G. S. Parry and D. E. Nixon, Nature **216**, 909 (1967).

[190] J. J. Yeh and I. Lindau, At. Data Nucl. Data Tables **32**, 1 (1985).

[191] S. Hüfner, *Surface Science* (Springer, 1995).

[192] C. O. Almbladh and P. Minnhagen, Phys. Stat. Solidi B **85**, 135 (1978).

[193] D. Briggs and M. P. Seah, *Practical Surface Analysis 1* (Wiley and Sons, 1990).